AN EXPERIMENTAL STUDY OF TRANSIENT TORQUE AND POWER NUMBER FOR HEAT GENERATOR DESIGN IN WIND THERMAL ENERGY CONVERSION

by Navid Nazari

A thesis submitted to the School of Graduate Studies

in partial fulfillment of the requirements for the degree of

Master of Engineering

Faculty of Engineering and Applied Science

Memorial University of Newfoundland

September 2023

St. John's, Newfoundland, Canada

Abstract

This research focuses on assessing the heat generator design for wind thermal energy conversion technology, in which wind power is directly converted into heat. Although several technologies have been proposed and investigated for heat generation, water heating through liquid agitation is selected for wind-to-heat conversion due to its simplicity and high potential for commercialization.

In this research, the technical challenges of the technology were understood by analyzing the system's performance during different operating conditions. It was seen that the system's performance under transient operating condition is of question since there is no literature available regarding the characteristics of the agitator's torque in baffled tanks during unsteady operation. Therefore, an experimental setup was designed and constructed for parametric study. The flow field inside the agitator was investigated by calculating the power number (N_P) of two impellers. This study considered several transient operation modes: acceleration, deceleration, and variable shaft velocity (sinusoidal). The analysis suggests that N_P in transient condition differs from the steady-state operation, which is an important outcome when matching an agitator to a wind turbine. The results show that the transient N_P is directly correlated to the angular acceleration/deceleration rate with higher sensitivity to the acceleration rather than deceleration. Furthermore, when the angular velocity of the impeller follows a sinusoidal profile, the change in transient N_P is affected by both frequency and amplitude. Finally, the temperature rise of the working fluid (distilled water) is measured during a 60-minute test by applying two different velocity profiles: constant angular velocity and sinusoidal velocity profiles. The results reveal that the sinusoidal velocity profile requires more input power, leading to a higher temperature rise than the constant angular speed operation.

Acknowledgments

I express my deep gratitude to several individuals who have been crucial to completing my master's thesis. Their unwavering support and guidance have been instrumental in my journey. I am profoundly thankful to my supervisor, Dr. Xili Duan, for his expertise, patience, and commitment to excellence. His guidance has shaped the direction of my research, and his mentorship has been inspiring.

The Graduate Studies Office in the Faculty of Engineering and Applied Sciences at MUN provided invaluable resources for which I am grateful.

I sincerely thank Steve from the Technical Service team, whose technical expertise was invaluable, and Dan Mclean for his continuous support and collaboration.

I also appreciate my family's emotional and moral support, especially my wife, Atena Goudarzi, and friends throughout this academic journey. Without them, this journey would have been a difficult one.

Navid Nazari

September 2023

Table of Content

Abstract ..... **ii**
Acknowledgments ..... **iii**
List of Figures ..... **vii**
List of Tables ..... **xi**
Nomenclature ..... **xii**
Greek Symbols xiii
Abbreviations xiv
Chapter 1 Introduction **1**
1.1 Wind power in net-zero carbon energy systems 1
1.2 Direct wind-to-heat energy systems 2
1.3 Wind thermal energy conversion technology based on fluid agitation 4
1.4 Objectives 5
1.5 The structure of this thesis 6
Chapter 2 Literature Review **8**
2.1 Types of wind turbines 8
2.2 History of WTES development 9
2.3 Wind-driven heating technologies 15
2.3.1 Compression-based WTEC 15
2.3.2 Friction-based WTEC 16
2.3.3 Induction-based WTEC 17
2.4 Thermal, environmental, and economic performance 18
2.5 Potential application 19
2.6 Fluid agitation heating 20
2.6.1 Methods to study fluid agitators 21
2.7 Heat generator design parameters 22
2.7.1 Start-up process and torque characteristic 23
2.7.2 Rotational speed 24
2.7.3 Working fluid thermo-physical properties 27
2.7.4 Impeller geometry 28
2.8 Summary 30
Chapter 3 Theoretical analysis of wind-powered heat generator **31**

3.1 Introduction.....31
3.2 Wind thermal energy system engineering and analysis.....31
3.2.1 Wind turbine.....32
3.2.2 Transmission system.....34
3.2.3 Load.....35
3.3 Wind turbine-agitator performance analysis.....37
3.3.1 General governing equations.....38
3.3.1.1 System mechanics.....38
3.3.1.2 Thermodynamic analysis.....38
3.3.2 Rotor-shaft operation mode.....40
3.3.3 System performance.....41
3.3.3.1 Steady-state operation.....41
3.3.3.2 Transient operation.....44
3.4 Analysis of agitator power absorption.....45
3.4.1 Dimensionless analysis.....46
3.4.2 Agitator transient power consumption.....50
3.5 Summary.....53
Chapter 4 Experimental setup and methods.....54
4.1 Introduction.....54
4.2 Experimental setup.....54
4.3 Signal processing.....57
4.3.1 Ensemble averaging.....58
4.4 Uncertainty analysis.....59
4.4 Experimental procedure.....61
4.5 Data analysis.....62
4.6 Summary.....63
Chapter 5 Results and discussion.....64
5.1 Introduction.....64
5.2 Effect of friction and inertia torque on measurements.....64
5.3 Steady-state analysis.....66
5.4 Transient analysis.....67
5.4.1 Acceleration.....68

5.4.1.1 Effect of different acceleration rates on torque (τ) and power number (N_P) 68
5.4.1.2 Effect of different ω_1 on torque (τ) and power number (N_P) under constant acceleration rate 72
5.4.1.3 Effect of different ω_2 on torque (τ) and power number (N_P) under constant acceleration rate 76
5.4.2 Deceleration 80
5.4.2.1 Effect of different deceleration rate on transient torque (τ) and N_P 80
5.4.2.2 Effect of different ω_1 on torque (τ) and power number (N_P) with constant deceleration rate 85
5.4.2.3 Effect of different final speed ω_2 on torque (τ) and power number (N_P) with constant deceleration rate 89
5.4.3 Sinusoidal velocity profile 93
5.4.3.1 Effect of different shaft angular frequency (*f*) on torque (τ) and power number (N_P) 93
5.4.3.2 Effect of different shaft angular amplitude on torque (τ) and power number (N_P) 96
5.5 Effect of different velocity profiles on temperature rise of the working fluid 99
5.6 Summary 100
Conclusion and recommendation 102
6.1 Conclusion 102
6.2 Recommendations 103
References 104
Appendix A: Equipment datasheet and drawings 117
A.1 Stepper motor 117
A.2 Torque sensor 118
A.3 Heat generator 119
A.4 Impeller 121
Appendix B: Codes 122
B.1 Sample Arduino code 122
B.2 MATLAB code 123

List of Figures

Figure 1-1: different wind energy systems. 3

Figure 1-2: a simplified schematic of wind thermal energy system based on fluid agitation. 5

Figure 2-1: different wind-to-heat concepts proposed for space heating [13]. 11

Figure 2-2: basic schematic of compression-based wind energy converter [16]. 16

Figure 2-3: basic schematic of friction-based wind energy converter (hydrodynamic retarder) [16]. 17

Figure 2-4: basic schematic of induction-based wind energy converter (eddy current heater) [16]. 18

Figure 3-1: power coefficient and blade tip speed curve of different rotor designs [78]. 33

Figure 3-2: different type of wind turbine based on their torque-speed characteristic [34]. 34

Figure 3-3: different transmission systems. 35

Figure 3-4: different type of loads that can be matched to wind turbine based on their torque-speed characteristic [34]. 36

Figure 3-5: different type of loads that matched to a type 1 wind turbine [34]. 42

Figure 3-6: N_P vs. Re for different impellers [87]. 49

Figure 4-1: schematic of the experimental setup developed for this study. 55

Figure 4-2: the experimental setup developed for this study. 56

Figure 4-3: 3D printed Four-bladed Flat Blade Turbine impellers for the purpose of experimental study ($FBT-07$: Blade Dia. = $70\,mm$, Blade Height = $30\,mm$, Blade Width = $2\,mm$, $FBT-10$: Blade Dia. = $100\,mm$, Blade Height = $30\,mm$, Blade Width = $2\,mm$) 57

Figure 4-4: raw and filtered torque signal using ensemble averaging method. 59

Figure 4-5: the procedure for data acquisition and data analysis. 63

Figure 5-1: results of the total torque and the sum of inertia and friction torque for the experimental test condition presented in Table 4-2 65

Figure 5-2: results of N_P across the Reynolds range for $FBT-10$ and $FBT-07$. 66

Figure 5-3: results of changing acceleration rate on torque for $FBT-07$ ($\boldsymbol{\omega_1} = 25.13\,rad/s, \omega_2 = 37.7\,rad/s$). 69

Figure 5-4: results of changing acceleration rate on torque for $FBT-10$ ($\boldsymbol{\omega_1} = 12.57\,rad/s, \omega_2 = 25.13\,rad/s$). 69

Figure 5-5: results of changing acceleration rate on N_P for $FBT-07$ ($\boldsymbol{\omega_1} = 25.13\,rad/s, \omega_2 = 37.7\,rad/s$) 71

Figure 5-6: results of changing acceleration rate on N_P for $FBT-10$ ($\boldsymbol{\omega_1} = 12.57\,rad/s, \omega_2 = 25.13\,rad/s$). 72

Figure 5-7: results of changing $\boldsymbol{\omega_1}$ on torque for $FBT-07$ in constant acceleration ($\omega_2 = 50.27\,rad/s, d\omega/dt = 12.57\,rad/s^2$) 74

Figure 5-8: results of changing $\boldsymbol{\omega_1}$ on torque for $FBT-10$ in constant acceleration ($\omega_2 = 43.98\,rad/s, d\omega/dt = 12.57\,rad/s^2$) 74

Figure 5-9: results of changing $\boldsymbol{\omega_1}$ on N_P for $FBT-07$ in constant acceleration ($\omega_2 = 50.27\,rad/s, d\omega/dt = 12.57\,rad/s^2$) 75

Figure 5-10: results of changing $\boldsymbol{\omega_1}$ on N_P for $FBT-10$ in constant acceleration ($\omega_2 = 43.98\,rad/s, d\omega/dt = 12.57\,rad/s^2$) 76

Figure 5-11: results of changing ω_2 on torque for $FBT-07$ in constant acceleration ($\boldsymbol{\omega_1} = 18.85\,rad/s, d\omega/dt = 12.57\,rad/s^2$) 77

Figure 5-12: results of changing ω_2 on torque for $FBT-10$ in constant acceleration ($\boldsymbol{\omega_1} = 12.57\,rad/s, d\omega/dt = 12.57\,rad/s^2$) 78

Figure 5-13: results of changing ω_2 on N_P for $FBT-07$ in constant acceleration ($\boldsymbol{\omega_1} = 18.85\,rad/s, d\omega/dt = 12.57\,rad/s^2$)..... 79

Figure 5-14: results of changing ω_2 on N_P for $FBT-10$ in constant acceleration ($\boldsymbol{\omega_1} = 12.57\,rad/s, d\omega/dt = 12.57\,rad/s^2$)..... 80

Figure 5-15: results of changing deceleration rate on torque for $FBT-07$ ($\boldsymbol{\omega_1} = 37.7\,rad/s$, $\omega_2 = 25.13\,rad/s$)..... 81

Figure 5-16: results of changing deceleration rate on torque for $FBT-10$ ($\boldsymbol{\omega_1} = 37.7\,rad/s$, $\omega_2 = 25.13\,rad/s$)..... 82

Figure 5-17: results of changing deceleration rate on N_P for $FBT-07$ ($\boldsymbol{\omega_1} = 37.7\,rad/s$, $\omega_2 = 25.13\,rad/s$). 83

Figure 5-18: results of changing deceleration rate on N_P for $FBT-10$ ($\boldsymbol{\omega_1} = 37.7\,rad/s$, $\omega_2 = 25.13\,rad/s$). 85

Figure 5-19: results of changing $\boldsymbol{\omega_1}$ on torque for $FBT-07$ in constant deceleration ($\omega_2 = 18.85\,rad/s, d\omega/dt = -12.57\,rad/s^2$)..... 86

Figure 5-20: results of changing $\boldsymbol{\omega_1}$ on torque for $FBT-10$ in constant deceleration ($\omega_2 = 12.57\,rad/s, d\omega/dt = -12.57\,rad/s^2$)..... 87

Figure 5-21: results of changing $\boldsymbol{\omega_1}$ on N_P for $FBT-07$ in constant deceleration ($\omega_2 = 18.85\,rad/s, d\omega/dt = -12.57\,rad/s^2$)..... 88

Figure 5-22: results of changing $\boldsymbol{\omega_1}$ on N_P for $FBT-10$ in constant deceleration ($\omega_2 = 12.57\,rad/s, d\omega/dt = -12.57\,rad/s^2$)..... 88

Figure 5-23: results of changing ω_2 on torque for $FBT-07$ in constant deceleration ($\boldsymbol{\omega_1} = 50.27\,rad/s, d\omega/dt = -12.57\,rad/s^2$)..... 90

Figure 5-24: results of changing ω_2 on torque for $FBT-10$ in constant deceleration ($\boldsymbol{\omega_1} = 43.98\,rad/s, d\omega/dt = -12.57\,rad/s^2$)..... 90

Figure 5-25: results of changing ω_2 on N_P for $FBT-07$ in constant deceleration ($\boldsymbol{\omega_1} = 50.27\,rad/s, d\omega/dt = -12.57\,rad/s^2$)..... 92

Figure 5-26: results of changing ω_2 on N_P for $FBT-10$ in constant deceleration ($\boldsymbol{\omega_1} = 43.98\,rad/s, d\omega/dt = -12.57\,rad/s^2$)..... 92

Figure 5-27: results of changing shaft angular frequency on torque for $FBT-10$ ($\omega_0 = 31.42\,rad/s, \omega_A = 12.57\,rad/s$)..... 94

Figure 5-28: results of changing shaft angular frequency on N_P for $FBT-10$ ($\omega_0 = 31.42\,rad/s, \omega_A = 12.57\,rad/s$)..... 96

Figure 5-29: results of changing velocity amplitude on torque for $FBT-10$ ($\omega_0 = 31.42\,rad/s, f = 1\,Hz$)..... 98

Figure 5-30: results of changing velocity amplitude on N_P for $FBT-10$ ($\omega_0 = 31.42\,rad/s, f = 1\,Hz$)..... 98

Figure 5-31: effect of different angular velocity profile on the working fluid temperature rise for $FBT-10$..... 99

List of Tables

Table 2-1: summary of studies related to wind-to-heat technology. 12

Table 2-2: a summary of studies on the detailed design of the wind thermal energy converter based on fluid agitation. 25

Table 4-1: measurement uncertainties. 60

Table 4-2: range of studied parameters. 62

Table 5-1: test conditions for the assessment of friction and inertia torque on the total torque. ... 64

Table 5-2: the results of steady-state N_P in this study and Ref. [87]. 67

Table 5-3: test conditions for transient operation with different acceleration rates. 68

Table 5-4: test conditions for transient operation with different ω_1. 73

Table 5-5: test conditions for transient operation with different ω_2. 77

Table 5-6: test conditions for transient operation with different deceleration rates. 81

Table 5-7: test conditions for transient operation with different ω_1. 86

Table 5-8: test conditions for deceleration with different ω_2. 89

Table 5-9: range of parameters for sine velocity profile experiments with different frequencies. 93

Table 5-10: range of parameters for sine velocity profile experiments with different amplitudes. 96

Nomenclature

A	Area (m^2)
c	Specific Heat Capacity of Material (J/kg. K)
C_P	Power coefficient of wind turbines
D	Impeller Blade Diameter (m)
D_T	Tank Diameter (m)
E	Total Energy (kJ/kg)
F	Force (N)
Fr	Fraud Number
J	Inertia ($kg.m^2$)
K	Turbulent Factor
m	Mass (kg)
n	Gearing ratio
n_b	Number of Baffles
N_P	Impeller Power Number
P	Power (W)
Q	Heat Transfer (kW)
R	Radius (m)
Re	Reynolds number
t	Time (s)

T	Temperature (℃)
U	Internal Energy (kJ)
v	Velocity (m/s)
V	Volume (kg/m^3)
W	Impeller Blade Width (m)
W	Work (kJ)
w_b	Baffle Width (m)

Greek Symbols

α	Acceleration (rad/s^2)
Δ	Difference
λ	Tip Speed Ratio
μ	Viscosity (Pa·s)
ρ	Density (kg/m^3)
τ	Torque (N·m)
ω	Angular Velocity (rad/s)
φ	Frequency (Hz)

Abbreviations

CEIH	Comprehensive Evaluation Index of Heat
CFD	Computational Fluid Dynamics
ECU	Energy Conversion Unit
FBT	Flat Blade Turbine
HAWT	Horizontal Axis Wind Turbine
RPM	Revolutions Per Minute
SB-VAWT	Straight-bladed Vertical Axis Wind Turbine
TTL	Transistor-Transistor Logic
VAWT	Vertical Axis Wind Turbine
WECS	Wind Energy Conversion Systems
WTES	Wind-powered Thermal Energy System

Chapter 1 Introduction

1.1 **Wind power in net-zero carbon energy systems**

The imperative to address global warming and limit temperature increases drives the need for impactful actions to transition toward low-carbon energy systems. While the primary cause of climate change is human activities, substantial progress has been made in understanding and mitigating its effects. A range of strategies, including the commitment of numerous countries to achieve net-zero carbon emissions, underscores the global determination to combat climate change [1-2]. In this regard, utilizing new methods to decrease societies' dependency on fossil fuels is very important.

In cold regions, the demand for heat holds a more immediate significance. In 2018, the combined usage of space heating and water heating accounted for a significant 81.4% of the total energy consumed by Canadian households. Specifically, 64.0% and 17.4% were dedicated to space heating and water heating, respectively, while the remaining 18.6% were allocated to lighting, appliances, and space cooling. [3]. Notably, a significant proportion of the 682 million liters of diesel fuel consumed in 2020 within remote communities in Canada was explicitly designated for heating [4]. Similarly, in the European Union (excluding Mediterranean countries), residential energy consumption is primarily dominated by space heating, accounting for approximately 60-80% of the total residential energy usage. In comparison, an additional 13% is allocated for heating water tanks. [5]. In the Russian region, the demand for residential energy is dominated by space and water heating, comprising 58% and 25%, respectively. These two categories together contribute to a substantial 83% of the total energy demand. Consequently, the primary objective is to provide adequate heating and hot water solutions with optimal efficiency [6].

Considering the scarcities of fossil fuels, environmental degradation, logistical challenges, and price instability associated with them, the integration of renewable energy resources has resulted in widespread attention to cater to energy needs around the globe. This approach offers several key advantages, including the abundance of resources, reduction of pollution, elimination of long-haul transportation demands, and the sustainability of resources [7].

Wind power is a highly abundant resource globally among different renewable energy sources. Its cost is consistently declining, making it a potential contender for being the most cost-effective electricity generation method by 2030 [8]. As of the close of 2018, the worldwide installed capacity for wind power had reached an impressive 597 GW, contributing to nearly 5% of the global electricity demand [9]. Nevertheless, this current capacity remains significantly lower than the immense potential of global wind power, estimated to exceed 200,000 GW [10]. This rapid expansion of wind energy utilization is paralleled by substantial research and development in both academic and industrial sectors, focusing on Wind Energy Conversion Systems (WECS). Several studies and publications have explored various grid-connected and stand-alone WECS configurations, analyzing generator types and power electronic converters in depth [11, 12].

1.2 Direct wind-to-heat energy systems

Traditionally, renewable energy sources, specifically wind, have been utilized to produce heat indirectly. The process involves converting the rotational energy generated by a wind turbine into electricity via an electrical generator. The electricity produced can be transformed into heat through an electric heater, boiler, or heat pump [13]. The outcome of this method is the production of heat through wind energy.

The traditional windmill has existed for over 2,000 years and is a viable substitute for indirect wind power utilization [14]. The wind rotor directly transmits rotational energy to a machine's axis,

enabling activities such as woodcutting or grain grinding [14]. This antiquated methodology is still pertinent, mainly when used with modern technologies, as it is more energy-efficient than converting energy to electricity and subsequently back to rotational energy.

A direct wind-to-heat system converts wind energy to heat at the generation source. The heat generated is then stored in thermal energy storage for future use. This system is called a Wind-powered Thermal Energy System (WTES) [13]. Figure 1-1 shows different wind energy systems.

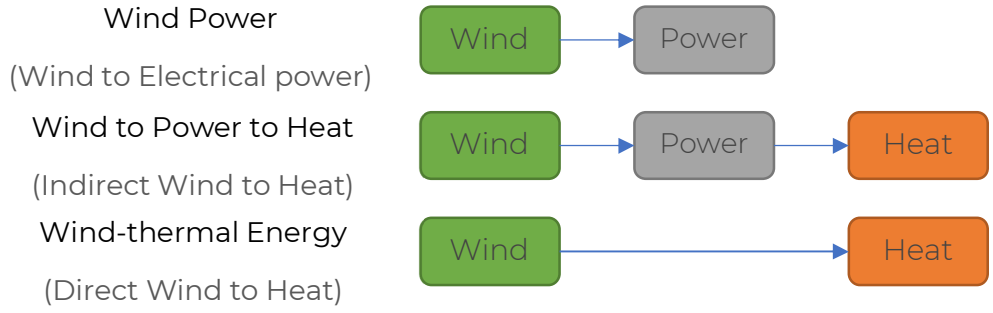

Figure 1-1: different wind energy systems.

Directly producing heat is significantly more cost-effective and sustainable than converting wind-generated electricity into heat using electric heating devices. There are two reasons for this phenomenon.

Mechanical windmills have a lower level of complexity, resulting in a more cost-effective and less resource-intensive construction process, ultimately leading to an extended lifespan. By eliminating the inclusion of an electrical generator, power converters, transformer, and gearbox in a water brake windmill, it becomes possible to construct the windmill with reduced robustness because of the weight savings [13].

Secondly, direct wind energy conversion into heat (or mechanical energy) can yield higher energy efficiency than electric conversion. Consequently, fewer wind energy converters are required to deliver a specific amount of heat, resulting in less space and resource utilization [14].

In addition to the above, direct heat generation significantly enhances small wind turbines' economic and environmental viability. Empirical evidence indicates that these smaller wind turbines, designed for electricity generation, exhibit substantial inefficiencies and often fail to meet the required energy output [15]. Nonetheless, employing comparable models for heat production has the potential to reduce embodied energy and expenses, expand the lifespan, and optimize efficiency.

The existing body of literature indicates that three distinct methodologies have been identified to design a heat generator capable of efficiently converting wind energy into heat. These methodologies include compression, friction, and induction, individually or in combination [16]. In all proposed devices, wind energy is converted into rotational energy by utilizing the wind turbine's rotor power. Subsequently, this rotational energy is transferred to a working fluid, a gas, or a liquid (such as water, oil, or sodium chloride), circulating within a closed-loop system. The rise in temperature of the working fluid enables the transfer of heat, which can be directly delivered to the end consumer or routed through a heat exchanger to a secondary circuit responsible for providing heat to its respective consumer.

1.3 Wind thermal energy conversion technology based on fluid agitation

Wind thermal conversion based on friction uses the rotational energy of the shaft to mechanically rotate an impeller submerged in a fluid [16]. As a result, heat is generated by friction losses among the molecules of the working fluid as the impeller rotates.

The simplest friction-based wind thermal energy conversion type is an impeller coupled to a wind turbine that stirs a fluid in a baffled tank. In this application, the system comprises the following components: 1) wind turbine, 2) transmission system, and 3) liquid stirrer, which includes container, baffles, and impeller. Considering the comprehensive knowledge required to design each of these components, a wind-heat generator should have all these parts designed in an integrated manner. Mathematical and numerical simulations and experimental testing can also improve the design. Figure 1-2 shows a simple schematic of a wind-heat device based on the liquid-stirring method.

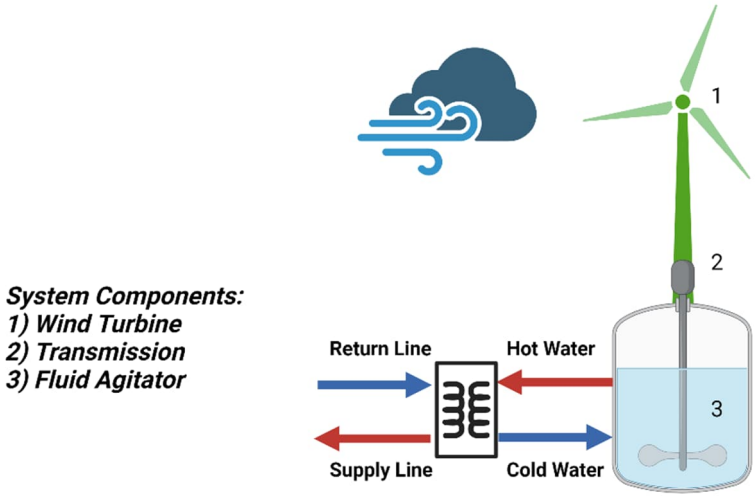

Figure 1-2: a simplified wind thermal energy system schematic based on fluid agitation.

1.4 Objectives

This study examines the design of a heat generator utilizing fluid agitation technology for direct wind-to-heat energy systems. This study can be separated into two sections: the technical analysis of a heat generator for direct wind energy conversion into heat and the experimental evaluation of

the heat generator's performance across various operating conditions, specifically transient conditions.

The objectives of technical analysis can be summarized as follows:

- Developing governing equations that describe the physics of the system.
- Analyzing system performance during steady-state and transient conditions.

In addition, the aims of the experimental study are as follows:

- Developing an apparatus by utilizing an electric motor instead of a wind turbine to study the torque characteristic of the fluid agitator under different possible operating modes.
- Analyzing torque and power number changing patterns through experimental study for different operating scenarios in steady-state and transient modes.

1.5 The structure of this thesis

In Chapter 2, a review of current literature on the topic of direct wind-to-heat systems, including wind-to-heat technologies and agitation heaters, is performed to provide a background to the whole thesis.

Chapter 3 aims to assess the performance of the wind-driven agitator heater for different operating scenarios. The governing equations and design parameters are presented and analyzed.

Chapter 4 details the experimental setup designed for the parametric study. In addition, the testing procedure followed for the data acquisition, along with the signal processing and data analysis method, are presented in this chapter.

Chapter 5 presents the experimental results of the torque measurement study. The data is examined per the research goals, and significant factors impacting the device's performance are evaluated.

Chapter 6 summarizes the primary outcomes, and recommendations regarding future research directions are given at the end.

Chapter 2 Literature Review

2.1 Types of wind turbines

Wind turbines harness the power of wind and transform it into mechanical energy through the rotor. The mechanical energy then can be utilized for several purposes, including water pumping and electricity generation [17]. Wind turbines can typically be categorized based on their application, capacity, number of blades, the relative placement of the rotor shaft in relation to the ground, the type of aerodynamic forces produced by the blades, and other factors [18]. The categorization of wind turbines can be primarily achieved through two methods, namely, the positioning of the rotor shaft in relation to the ground and the aerodynamic forces exerted on the blades [18]. Wind turbines can be categorized into two types, namely Horizontal Axis Wind Turbines (HAWT) and Vertical Axis Wind Turbines (VAWT), based on their relative position to the ground. Wind turbines can also be classified into lift-type and drag-type wind turbines, depending on the force type exerted by the blades [18].

Today, most large-scale wind turbines are airfoil three-bladed HAWTs. These turbines are characterized by their ease of control and relatively high efficiency [19]. Today's HAWT exhibits an efficiency ranging from approximately 30% to 45%, with a maximum efficiency of 50% [20-21]. In recent years, with the advancements in large-scale wind turbines and wind farms, there has been an increasing focus on small-scale VAWT wind turbines. These turbines are capable of distributed generation and catering to the off-grid wind power market, leading to a rise in attention towards them [18]. On the other hand, small-scale VAWT wind turbines have certain drawbacks compared to their large-scale counterparts. These include a limited swept area of the rotor, the challenge of start-up under low wind speeds, etc. [18].

The most significant difference between the HAWT and VAWT is that the rotor of a HAWT must always face the direction of the wind and thus requires a yaw system [22]. The drivetrain gearbox is the most critical component of HAWT, with over 20% of breakdowns attributed to gearbox failure due to excessive wear. However, the VAWT can receive wind from any direction and does not need a yaw system. Utilizing a direct-drive generator eliminates the need for a complex speed-increasing multistage gearbox and the potential failures that come with it [23-24]. The direct connection between the driveshaft and generator also results in minimal energy loss during the conversion from mechanical to electrical energy [25]. An additional benefit is that the mechanical load can be linked directly to the rotor shaft of the VAWT and placed at ground level, eliminating the necessity for a large tower to support the equipment's weight and avoiding the need for slip rings or flexible cables to connect the generator to the load, which is significant for smaller turbines. Therefore, the VAWT can be considered a suitable option for the small- and middle-scale wind power market due to the benefits mentioned above.

Finally, the Straight-Bladed Vertical Axis Wind Turbine (SB-VAWT), which is a type of lift-type VAWT, is extensively researched and is considered a good option among different types for off-grid small-scale energy systems in urban and rural areas due to its simple design, low cost, and high efficiency [18].

2.2 History of WTES development

During the 70s, many investigations were performed to develop an alternative energy conversion technology due to the oil crisis. James et al. [27] devised a methodology for wind-powered heating systems with storage for household heating. The study involved connecting wind turbines to a heating system, where all wind-generated electricity was transformed into heat through resistance

heating. The produced heat was directly supplied to the heating load, storing excess heat in storage tanks. The system solely utilized wind power for heating and did not directly convert it into heat.

Several patents have been published since the 1970s regarding wind-driven heating devices for low-temperature heating, including a system that utilizes wind-driven heat pumps [28]. One of the earliest patents in this field was issued in 1971, in which a wind-powered pump circulates fluid in a pipe circuit, generating heat through friction between the fluid and the pipes, which is then transferred and stored in a thermally insulated tank [29]. In 1978, Neyeloff analyzed a direct wind energy converter based on agitation to heat water in a closed tank [30].

In 1980, a patent was issued for a wind power device that generates heat using eddy current heating, where a heating component is placed in a liquid within a vessel and connected to a wind turbine rotor, allowing the heated liquid to be stored and circulated to heat loads using a heat transfer fluid [31]. Later, a wind-driven direct water heating system for heating dairy applications was developed and tested by the Agricultural Engineering Department at Cornell University with support from the U.S.D.A. Science and Education Administration/Agricultural Research in 1981 [32]. The Cornell wind-driven direct water heating system used a commercial wind turbine mechanically coupled to an Energy Conversion Unit (ECU) where water was agitated, thus converting mechanical energy to heat [32]. In 1982, Nattuvetty and Gunkel [33] analyzed the theoretical performance of the turbine-load system under various operating modes. In this work, the authors studied the overall performance efficiency of wind turbine-load systems under different operating conditions. In addition, several attempts have been made in Denmark to commercially utilize wind energy for space heating applications during the last three decades [14]. Overall, there has been an interest in developing direct wind thermal energy conversion methods, as shown by different researchers in the previous decades. Figure 2-1 summarizes the concepts proposed for generating heat from wind

energy. In addition, Table 2-1 presents some relevant selected research that studied wind thermal energy conversion technology from different aspects, such as thermal, economic, and environmental perspectives, along with the proposed applications and the studied configuration.

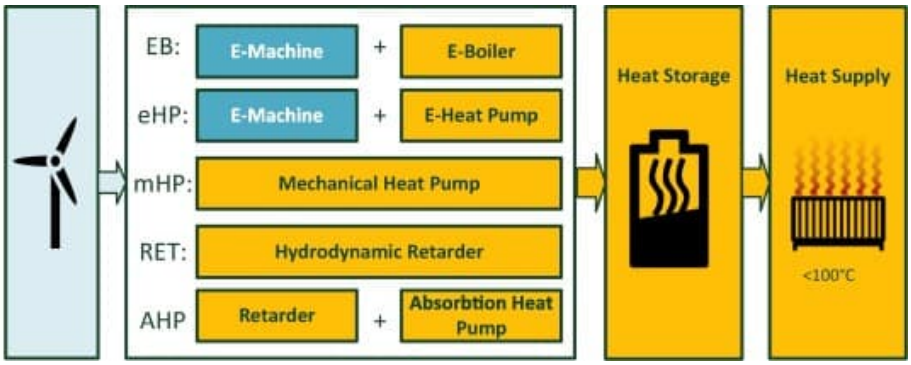

Figure 2-1: different wind-to-heat concepts proposed for space heating [13].

Table 2-1: summary of studies related to wind-to-heat technology.

Author	Publication Year	Performance Analysis	Economic Evaluation	Detail Design and/or Testing	Studied Configuration	Proposed Application
Nattuvetty [30]	1979	•		•	Electric Motor + Heat Generator	Space Heating
Gunkel et. Al [32]	1981	•	•	•	Electric Motor + Heat Generator	Space Heating
Nattuvetty and Gunkel [33]	1982	•			Vertical Axis Wind Turbine + Heat Generator	Space Heating
Kirke [34]	1998	•			Vertical Axis Wind Turbine + Heat Generator	Space Heating
Kim et al. [35]	2001			•	Electric Motor + Heat Generator + Heat Exchanger	Space Heating
Nakatake and Tanaka [36]	2005			•	Windmill + Heat generator	Desalination
Kim et al. [37]	2005			•	Electric Motor + Heat Generator + Heat Exchanger	Space Heating
Kim et al. [38]	2005			•	Vertical Axis Wind Turbine + Heat Generator + Heat Exchanger	Greenhouse Heating

Katawaluwa et al. [39]	2006			•	Vertical Axis Wind Turbine + Heat Generator + Radiator	Space Heating
Sateikis et al. [40]	2006	•			Detailed configuration was not provided	Space Heating
Chakirov and Vagapov [41]	2011			•	Vertical Axis Wind Turbine + Heat Generator	Space Heating
Al-Nimr et al. [42]	2012			•	Windmill + Desalination	Space Heating
Zhao et al. [43]	2014			•	Electric Motor + Heat Generator	Space Heating
Cerneckiene and Zdankus [44]	2014	•	•		Detailed configuration was not provided	Space Heating
Okazaki et al. [45]	2015	•	•		Wind Turbine + Thermal Storage + Rankine Cycle	Power Generation
Hu et al. [46]	2017			•	Vertical Axis Wind Turbine + Heat Generator	Space Heating
Hu et al. [47]	2017			•	Vertical Axis Wind Turbine + Heat Generator + Desalination	Desalination
Su [48]	2017	•	•		Detailed configuration was not provided	Space Heating
Zheng et al. [49]	2017		•		Detailed configuration was not provided	Industrial Heating
Mei et al. [50]	2017				Detailed configuration was not provided	Space Heating
Cheng et al. [51]	2017	•	•		Wind Turbine + Heat Generator + Long Distance Transmission	Space Heating
Yang et al. [52]	2018			•	Electric Motor + Heat Generator	Space Heating

Cao et al. [53]	2018	•	•		Wind Turbine + Heat Generator + Thermal Storage	Power Generation
Ma [54]	2019			•	Fan + Eccentric Stirring Device	Greenhouse Heating
Chen et al. [55]	2019	•	•		Wind Turbine + Heat Generator + Thermal Storage	Space Heating
Zhang et al. [56]	2020			•	Wind Turbine + Stirrer Device + Electric Rod	Space Heating
Liu et al. [57]	2021			•	Electric Motor + Heat Generator	Space Heating
Chen et al. [58]	2021			•	Electric Motor + Heat Generator	Space Heating
McLean et al. [59]	2022			•	Vertical Axis Wind Turbine + Heat Generator	Space Heating
Liu et al. [60]	2022			•	Electric Motor + Heat Generator	Space Heating

2.3 Wind-driven heating technologies

A wide range of research activities are conducted to investigate the conversion of mechanical energy into heat by a device. Overall, three primary methods are introduced to convert wind energy directly into heat: compression, friction, and induction [16]. In these devices, wind energy is converted into rotational energy by the wind turbine rotor and then transferred to a working fluid (e.g., water, oil), which circulates in a closed circuit and delivers heat to the consumer directly or through a secondary circuit.

2.3.1 Compression-based WTEC

The wind's rotational energy in compression-based wind thermal conversion is harnessed to power a pump or compressor, increasing the working fluid's pressure and temperature (Figure 2-2). This concept is commonly employed in compressed air systems [61-62] and heat pumps [63-66]. In the case of a liquid, the acceleration of the working fluid within the pipe system by the pump leads to an increase in friction losses due to the fluid's velocity, resulting in the conversion of kinetic energy into heat; additionally, the installation of an orifice or throttle valve further contributes to heat generation [67-69].

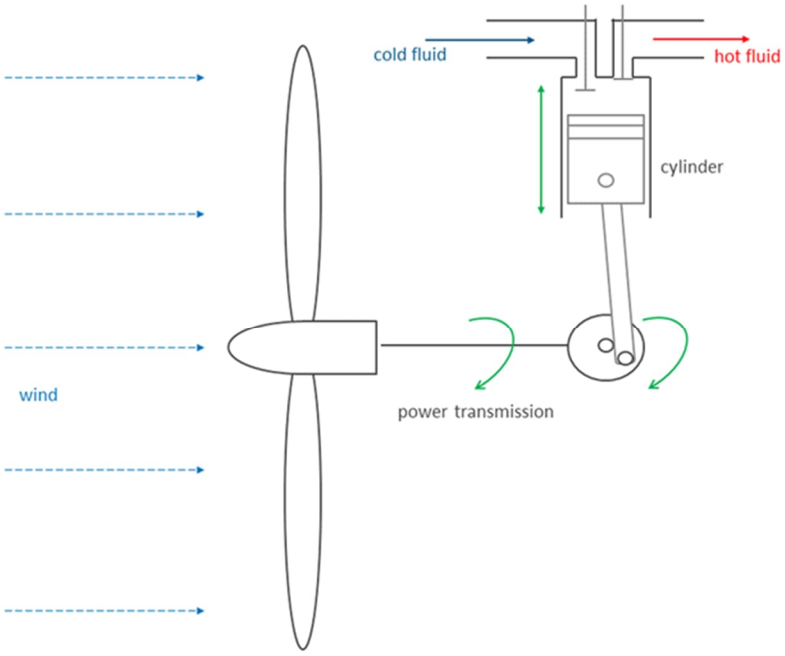

Figure 2-2: basic schematic of compression-based wind energy converter [16].

2.3.2 Friction-based WTEC

Friction-based wind thermal conversion employs the rotational energy of a shaft to mechanically rotate an impeller in a working fluid, which generates heat through friction losses (Figure 1-2). An example is the "Joule machine" concept, where an impeller is connected to a wind turbine and stirs a working fluid in a tank equipped with baffles [39, 41, 45, 47, 48, 52, 54]. A more advanced application is a hydrodynamic retarder, where a working fluid circulates in a toroidal chamber created by a rotor and a stator with vanes (Figure 2-3), in which adjusting the clearance between the rotating and fixed parts of the chamber produces a braking torque resulted from the viscous drag of the fluid [66]. Solid-solid friction, like what is used to slow down or stop vehicles or objects, is another example of friction-based heat generation that can produce heat over 400°C [70], and although widely used due to its simple structure and low costs, it requires frequent maintenance due to material wear during braking.

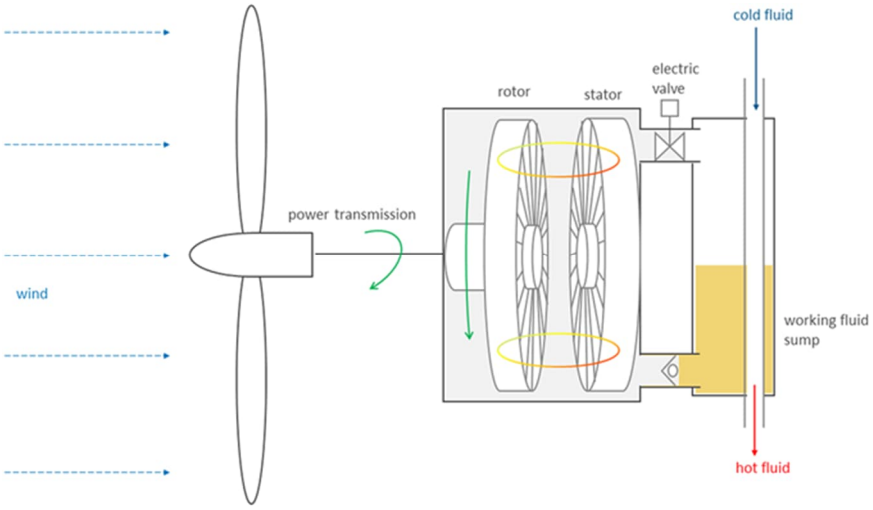

Figure 2-3: basic schematic of friction-based wind energy converter (hydrodynamic retarder) [16].

2.3.3 Induction-based WTEC

Induction-based wind thermal conversion, also known as eddy current heating, utilizes the rotational energy of wind turbine blades to generate heat through the flow of eddy currents induced by an alternating magnetic field (Figure 2-4). This technology achieves high temperatures up to 560 or 600 °C with an efficiency ranging from 70% to 99% [71-76].

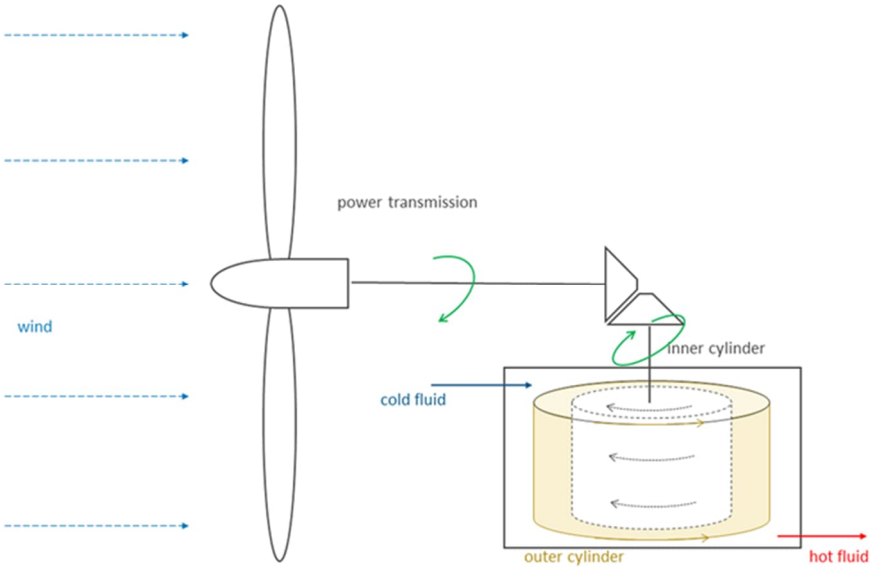

Figure 2-4: basic schematic of induction-based wind energy converter (eddy current heater) [16].

2.4 Thermal, environmental, and economic performance

Efficiency is an essential factor to consider when selecting an energy conversion process. This makes analyzing the performance of direct wind-thermal technologies critical. It is argued that direct wind-thermal conversion (or kinetic-thermal conversion) is more efficient than wind-electricity-thermal conversion because there are much smaller conversion losses, and almost all the wind energy can be converted into thermal energy [42]. Based on the Joule Machine concept, Chakirov and Vagapov mathematically demonstrated that wind energy can be converted into heat using wind heat generators [41]. The authors of Ref. [47] stated that a wind energy direct heating system reduces the energy conversion step and saves power generation equipment compared to the wind-electrical-thermal conversion system. In addition to reducing the initial investment cost, the system will significantly improve energy utilization efficiency [47]. Considering environmental concerns, it was shown that direct wind-thermal conversion could result in a reduction of carbon dioxide emissions by 21.22 tons compared to the burning of 8.10 tons of coal during the heating season [54].

Another critical parameter that should be considered in developing any energy conversion concept is the size of the system since it directly affects its economic performance. To determine the size of the wind-heat generation system, it is proposed to consider the following: 1) thermal load demand. 2) wind speed. 3) mechanical efficiency (including gearbox, rotor, and pump). The system's overall efficiency will be improved by designing the system according to these parameters and by the adequate insulation of the circulation system and heat generator [42].

Although there are advantages to wind thermal energy conversion systems, the deployment and commercialization of heat-generation wind turbines are limited, and their installed capacity is insignificant compared to electricity-generating wind turbines [48]. This could be because of the value of electricity, which is significantly higher than that of low-temperature heat (at least twice as high as heat prices for heating purposes) [49-50].

2.5 Potential application

Table 2-1 shows that heating applications are the most favorable direct wind heat generation technology market. As previously explained, water and space heating are the most significant part of residential energy consumption, specifically in cold regions [47]; therefore, most direct wind thermal energy conversion research focuses on the residential sector's heat generation potential. However, a few studies also investigated the possibility of large-scale direct wind heat generation for greenhouse heating and industrial processes [54]. Ref. [47] concluded that wind energy conversion for greenhouse heating has many advantages over the prior technologies, such as high heat supply and energy conservation efficiency, minimal restriction factors, stable heat supply, low economic costs, and rapid benefit recovery. In addition, the possibility of heat generation through WTEC for industrial-scale electricity generation was also studied in Ref. [51]. Researchers also proposed the generation of wind thermal heat as a method for desalinating water [18, 28]. Friction

heating converts wind energy into thermal energy, which is then used to produce fresh water. It has been demonstrated that wind heating technology can be applied to small-scale maritime and larger residential applications for water desalination [24, 35].

2.6 Fluid agitation heating

In this thesis, agitation technology is selected to be investigated for integration into a wind turbine for converting the mechanical energy of the wind turbine rotor into heat. Compared to other technologies to convert kinetic energy into heat, agitation heating is considered the most straightforward technology to produce heat since it is easy to integrate into the wind turbine.

Equipping a vessel with an agitator is considered a standard method to increase the homogeneity of the fluids or improve heat and mass transfer rates inside tanks. In this regard, mechanical mixing or agitation has become essential to various process-based industries such as chemical, pharmaceutical, oil and gas, metallurgical, mineral, wastewater treatment, etc. [77]. Since the agitation method is a mature technology widely used in different industrial processes, integrating it into a wind turbine could reduce the cost of construction, scale-up, operation, and maintenance of its parts compared to other methods of direct heat generation.

The fluid heating process by agitation is as predictable as friction itself and inherently achieves unit efficiency; yet, to many observers, the agitation heater may appear awkward and inefficient. This misconception is, in context, understandable since common modern mechanisms and appliances do not exploit this simple conversion process from mechanical to thermal energy [44].

Even in the 18th Century, mechanical pioneers acknowledged the value of frictional power conversion to heat. Paddle-type fluid agitators were constructed and tested by scientists such as

Joule as early as 1830. They were instrumental in equating mechanical power and heat and quantifying the conversion process [44].

Research on wind energy systems and applications has inspired a renewed interest in water heating through agitation in recent years. However, an exhaustive assessment of several aspects is necessary when designing a wind-heater device. Investors and decision-makers must know the methods and techniques that improve energy conversion efficiency to choose the most appropriate configuration. In this regard, the concept study of wind-heater technology is critical. Additionally, the design of agitation heaters involves different factors and parameters, such as the geometry of components (e.g., tank diameter, impeller shape, impeller parameters, number of baffles, etc.) and time-dependent parameters (e.g., rotational speed). The relationship between these factors and device performance can be investigated through different methodologies, including numerical techniques and experimental investigations. The following sections review the literature regarding the methods utilized to study wind-heater devices and the effects of various design factors on the agitator performance (selected papers are tabulated in Table 2-2).

2.6.1 Methods to study fluid agitators

Mathematical and numerical methods were applied to predict the heat generator flow's behavior and improve its performance. Most past studies benefited from simplified theoretical analysis to provide proof of concept through thermal and economic viability [41]. In addition, basic analytical modeling approaches were used to find a match between heat generator dimensions and wind turbine size [41]. The other research focus was predicting the amount of heat generation considering the actual wind profile. However, in most recent studies, an increasing trend can be seen for utilizing numerical simulation through Computational Fluid Dynamics (CFD) to predict the turbulent behavior of the flow under different working conditions [29, 48]. CFD tools helped

researchers investigate various novel geometries and working fluids with different thermo-physical properties to improve the heat generator performance. In addition, researchers recently used statistical tools to prioritize the effect of other parameters and working fluid properties on heat generator performance [45, 48]. It should be noted that although various numerical and statistical simulation tools can significantly help designers enhance heat generator device performance, the limitation of these tools to predict the systems' behavior should not be missed.

Another helpful tool that designers extensively used to understand the relationship among different parameters of the heat generator device was experimental testing. Since performing experimental analysis of the integrated system was hard to apply due to economic and lab limitations, in most of the available literature, an electric motor simulated wind turbine mechanical energy. Different design parameters such as torque characteristics, the geometry of the impeller (width, diameter, number of blades, etc.), container volume (height and width), and thermo-physical properties of working mediums (density, viscosity, specific heat, thermal conductivity, etc.) were analyzed by different authors through prototype testing. The integrated experimentation of wind turbine-heat generator devices was also studied in some research [26, 34].

2.7 Heat generator design parameters

This section is dedicated to reviewing the available literature regarding various design parameters of the heat generator device to provide a clear insight into how different parameters can affect heat generator efficiency. It is worth mentioning that many aspects of designing a heat generator are the same as a mixing system, but the provided literature in the following sections is just focused on research that used an agitator for direct wind thermal energy conversion.

2.7.1 Start-up process and torque characteristic

As shown in sections 3.3.1 and 3.3.3, the system operation, including start-up, depends on the magnitude of drag forces, including the impeller resistive force and the amount of input torque the wind turbine generates. Although the higher resistive force of the impeller results in more agitation and heat generation, turbine operation will only be possible if the sum of the resistive forces in the drivetrain is lower than the wind turbine rotor torque. Therefore, balancing the turbine's torque output to the sum of the resistive forces is critical in designing the wind agitator system.

Gunkel et. Al analytically researched the compatibility of a wind turbine and a fluid agitator by field testing. They stated that since both the wind turbine and liquid agitator are fan-in-fluid processes, the two devices can be united so that the agitator unit can fully utilize the wind turbine's mechanical output at all rotational speeds [44]. Chakirov and Vagapov mathematically showed that a match can be made between the torque-speed characteristics of a wind turbine and a heat generator to allow the wind turbine to operate at maximum power [41]. Other researchers also concluded the same result [20, 21], proving the fluid agitator's high potential for matching a wind turbine.

Regarding the start-up process, Mclean et al. revealed that the H-rotor Darrius turbine produces very little positive torque during the dead-band region during start-up by analyzing the experimental data [59]. They suggested that such a turbine may require a clutch mechanism to reach its steady-state rotation rate. Chen et al. claimed that analysis of the torque characteristics is very important for studying the stirring wind-heating start-up process, as it characterizes the system's starting capability [58]. In this regard and to improve the start-up process, a torque-limited hydraulic coupling was used to reduce the torque required during the starting process. The experimental results indicate that the starting torque decreased when a torque-limited hydraulic

coupling was used instead of a mechanical shaft connection in the stirring wind-heating system [58].

2.7.2 Rotational speed

Several research studies focused on the effect of rotational speed on the rise in temperature of working fluid. In Ref. [46], the authors showed that water and thermia oil temperatures reached 78 and 87 °C after 40 minutes of rotation with 660 rpm, respectively. It was concluded that the higher the fluid viscosity, the higher the fluid temperature. Yang et al. claimed that stirred liquid heating is feasible, and the heat effect is remarkable [52]. The increased rotation speed will increase the temperature rise and heat efficiency of the same working substance. Research by Hu et al. revealed that wind thermal efficiency is greatly affected by the speed at which stirring vanes rotate [46]. In the same experimental conditions, they concluded that the higher the speed of mixing vanes, the greater the temperature rise of the liquid and the greater the efficiency of the wind heater [46]. Overall, the available literature proves the significant effect of rotational velocity on rising working fluid temperature and wind-heater efficiency.

Table 2-2: an overview of studies on the detailed design of the wind thermal energy converter based on fluid agitation.

Author	Publication Year	Simulation Method		Experimental Setup			Design Parameters			
		Analytical	Numerical/Statistical	Heat Generator	Wind Turbine + Heat Generator	Heat Generator	Torque	Rotational Speed	Fluid Properties	Impeller Geometry
Nattuvetty [30]	1979	•				•				
Gunkel et. Al [32]	1981	•		•		•	•			•
Nattuvetty and Gunkel [33]	1982		•	•			•			
Kim et al. [35]	2001					•		•	•	•
Nakatake and Tanaka [36]	2005	•						•		•
Kim et al. [37]	2005					•		•		•
Kim et al. [38]	2005			•		•		•		•
Katawaluwa et al. [39]	2006	•					•	•		

Chakirov and Vagapov [41]	2011	•					•	•			
Al-Nimr et al. [42]	2012	•						•	•		
Zhao et al. [43]	2014		•			•		•			•
Hu et al. [46]	2017			•		•				•	•
Hu et al. [47]	2017	•					•				•
Yang et al. [52]	2018					•		•	•		
Ma [54]	2019					•					•
Zhang et al. [56]	2020	•				•				•	•
Liu et al. [57]	2021		•			•				•	•
Chen et al. [58]	2021			•		•	•	•			
McLean et al. [59]	2022	•					•	•			•
Liu et al. [60]	2022		•			•		•	•		

2.7.3 Working fluid thermo-physical properties

Among different thermo-physical properties, the focus was on studying the specific heat effect. A comparative analysis of the three working fluids showed that the 46# hydraulic oil with the smallest specific heat capacity can achieve higher heating temperatures [52]. Reference [46] compared the rise in temperature of water and thermal oil. It was reported that with the constant energy input, the increase in temperature of water and oil was 5°C and 8 °C, respectively. Considering the difference between the specific heat capacity of hydraulic oil and water, which are 1.9 kJ/kg °C and 4.18 kJ/kg °C, it was concluded that although the temperature rise of water was lower, its capacity to absorb heat is higher. Therefore, water is more thermally efficient than hydraulic oil. The statistical analysis results by Xingran et al. revealed that a heater's specific heat capacity mainly affects the preheating time (start-up). Therefore, its effect is more significant under short and variable wind conditions [57]. The results suggest that in windy areas, where the duration of rated wind during a windy season is long, the effect of specific heat on heating performance will be minimal. In reference [60], an experimental approach was employed to investigate the heating process of 30 types of working fluids by using multiple linear regression techniques and CFD tool, resulting in the establishment of a numerical evaluation model for the impact of thermophysical properties on the Comprehensive Evaluation Index of Heat (CEIH). The experimental findings and regression model analysis indicated that the heating effect was primarily influenced by the specific heat capacity, with density also playing a beneficial role in stirring heating. Based on these results, it was suggested that water-based salt solutions, such as KCL, exhibited superior heating effects compared to oil-based working fluids [60].

Regarding density, the simulation results and experiments revealed that a high-density fluid could absorb more of the rotor's kinetic energy when the viscosity is kept unchanged [57]. However, the required heating power will increase.

When it comes to viscosity, it was explained that viscous stress plays a crucial role in converting kinetic energy into thermal energy, but high viscosities can make turbulence more challenging to achieve [57]. In a heater, the working liquid enters the turbulent zone when Re > 4000, and there is complete turbulence when Re exceeds 10,000. This may be why most papers considered water the working medium to ensure turbulent flow (high Re) at low rotational speed [41].

2.7.4 Impeller geometry

According to the literature, the radial flow type impellers apply more significant shear stress to the fluid, generating more turbulence than their axial flow type counterparts. Therefore, they are considered the most appropriate geometry for the heat generator device. It was mathematically proved that the diameter of the impeller significantly impacts the heat generator's design [41]. It was shown that the power number can be changed by installing baffles to prevent mobility of the main volume of the liquid [41].

Experimental testing of three different groups of impellers for the heat generator device, including a Rushton turbine and two other double Rushton turbine impellers at a constant rotation speed and container volume, revealed a linear relationship between the temperature rise and the stirring time [57]. Based on the results, both double Rushton turbine impellers have similar temperature rise lines. Moreover, it was seen that temperature rise slopes in dual Rushton turbine impellers were higher than those in single impeller configuration [57]. It was concluded that by increasing the layer number and arranging the stirring rotors reasonably, the heating effect of the heat generator could be significantly improved because as the contact area between the rotors and working fluid

increases, more fluid is driven, intensifying the turbulent motion. However, the impeller should be arranged carefully since a close rotor arrangement will result in difficulty in returning the working liquid to the stirring center [57]. Finally, it is suggested that the rotor arrangement should be determined by four factors: heater size, rotor size, rotation speed, and type of liquid [57]. The CFD study of three different novel rotor geometries (a nonlayered-stirring impeller, a layered-stirring impeller, and a layered extruded stirring impeller) for the heating device was performed in Ref. [43]. The results revealed that the layered extruded stirring setup had the highest viscous dissipation rate at the same rotation speed, which means that the highest amount of mechanical energy turned into thermal energy per time unit [43]. The authors also noted that their numerical results were consistent with the experimental results [43]. Based on another experimental analysis of a heat generator with rotating and fixed vanes (separating vane), it was found that the average rotation speed of stirring vanes with separating blades was slower. However, the temperature of the liquid was higher due to the damping effect of the liquid [46]. As a result, more heat was generated by the damping effect than it was reduced by slowing down the stirring vanes' rotation speed. On the other hand, the experimental results revealed that the length of stirring vanes also significantly influences the wind heater's thermal efficiency [46]. With the increase in the size of the stirring vanes, the rotating speed of the moving vanes gradually becomes slower, but the heat generated by stirred liquid increases first and then decreases. However, when the width of the stirring vanes increases, the liquid temperature will not change significantly. It is concluded that there should be a best match point between the size of the moving vanes and the wind turbine, which could be calculated theoretically or decided by experiment [46].

2.8 Summary

Wind energy has a rapidly growing market, and studies are needed to enable its efficient utilization for other purposes, such as heat generation. Therefore, improving conversion technologies such as liquid stirring is essential in direct wind heat generation. This section provided an in-depth review of the published research with the information necessary to assist researchers regarding the effects of various design parameters on the heat generator device performance.

Many previous studies investigated the effect of different design parameters such as rotational speed, fluid properties, and impeller geometries. However, a missing point in these studies is that the researchers should have considered these parameters' effect on the agitator impeller's exerted torque. For example, although higher rotational speed will increase the heat generated in the tank, it also results in higher resistive force exerted on the impeller, leading to more input power consumption. Similarly, various fluids will have different densities and viscosity, affecting the impeller's torque. In this regard, studying any parameters should be accompanied by assessing the torque characteristic. Overall, the most critical aspect in designing a wind-heat generator is its torque characteristics, which should be clearly understood to optimize its design. In the following chapters, we will first assess the toque matching of the system and then perform experimental analysis to uncover an unknown torque behavior of the agitator heater in different operation modes.

Chapter 3 Theoretical analysis of wind-powered heat generator

3.1 Introduction

Fluid agitation heating was chosen for investigation in this research due to its simple system configuration and wide use in other studies for heat generation; the comparison of this technology with other wind-to-heat technologies is discussed in section 2.1.3, along with the investigation of main design factors.

This chapter analyzes the fundamental design aspects of the fluid agitator. In addition, the concept of turbine-heat generator torque matching for the wind thermal energy conversion device and system behavior under different operating conditions are discussed.

The aims of this part of the thesis are:

- Understating different parts of the system
- Presenting the governing equations that describe the physics of the system
- Analyzing system performance under different operating scenarios

3.2 Wind thermal energy system engineering and analysis

There are a wide variety of design factors for each WTES part, including wind turbine, transmission, and heat generator, which affect the system performance. In this regard, an evaluation of a heat generator, in our case, a fluid agitator, would only be complete considering the turbine that is most suited to drive the system, the transmissions that can be used, and the system efficiencies that may be achieved. In addition, improving the system's performance is only possible when the most compatible components are selected for the system's design. Therefore, the following sections briefly discuss wind turbines and transmission systems. Then, a detailed discussion about the design of the fluid agitator is given.

3.2.1 Wind turbine

When designing a wind power system, it is necessary to consider the properties of mechanical power from the rotor, such as torque and rotational speeds, as they are converted into another form of energy by an energy conversion component like mechanical pumps or electric generators. The characteristics of a wind turbine can be described using three equations, the first of which calculates the power of the turbine [20]:

$$P_{WT} = \mathrm{C}_P \frac{\rho_{air} A v^3}{2} \tag{3.1}$$

Where P_{WT} is the extracted power by wind turbines (W), C_P is the power coefficient of wind turbines, ρ_{air} is the air density (kg/m^3), v is the wind velocity (m/s), and A is swept area (m^2). Secondly, the power coefficient of a wind turbine is the function of the tip speed ratio (λ) of wind turbine blades, which the following equation can express:

$$\lambda = \frac{R\omega}{v} \tag{3.2}$$

Where ω is the rotor angular speed (rad/s) and R is the rotor radius (m). The optimal tip speed ratio determines the maximum power coefficient of a wind turbine ($\mathrm{C}_{P,max}$), and it is influenced by the rotor and blade designs [84] (see Figure 3-1). Thirdly, the wind turbine power (P_{WT}) can be determined through the combination of torque (τ) and angular speed (ω) which is given by:

$$P_{WT} = \tau . \omega \tag{3.3}$$

As a result, by substituting the tip speed ratio into the above equation, the torque output of the wind turbine (τ) will be:

$$\tau_{WT} = \frac{\mathrm{C}_P}{\lambda^3} \left(\frac{\rho_{air} A R^3}{2}\right) \omega^2 \tag{3.4}$$

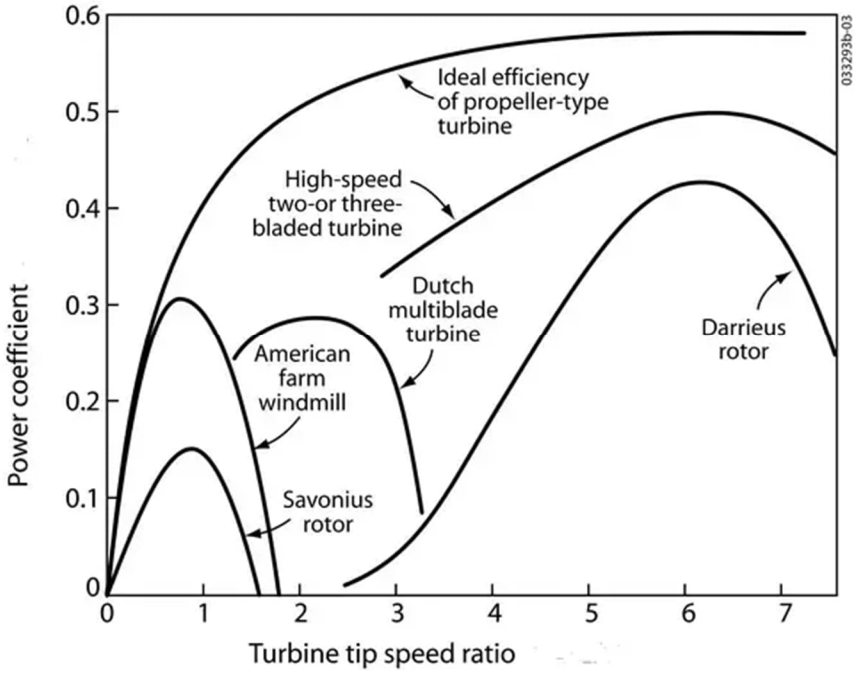

Figure 3-1: power coefficient and blade tip speed curve of different rotor designs [78].

Kirkle et al. classified wind turbines into three types based on their torque-speed curves [34]. Type 1 has low but significant torque when starting and at low speed, which is seen in low to medium solidity HAWTs and self-starting VAWTs. Type 2, high solidity rotors have high starting torque that decreases steeply with speed, such as in the fan windmill and Savonius rotor. Type 3 includes traditional Darrieus rotors with insignificant or negative torque at low speeds. Fig. 3-2 shows a schematic torque-speed curve of each wind turbine type. In the following sections, it will be shown that type 1 wind turbines can be considered the best choice for matching to a fluid agitator based on the torque-speed requirements.

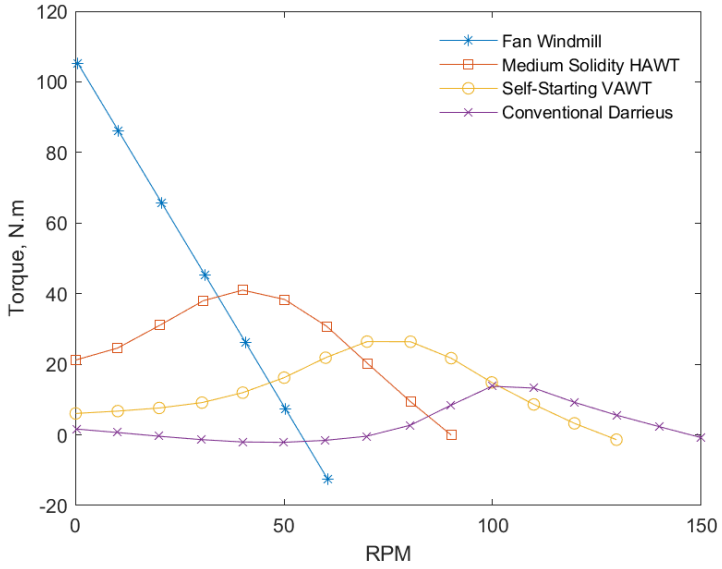

Figure 3-2: different type of wind turbine based on their torque-speed characteristic [34].

3.2.2 Transmission system

Transmissions can be divided into three types to match wind turbines to loads:

- Type 1: fixed ratio drive, which may or may not include gearing
- Type 2: clutch or other load-disengaging device for easy starting
- Type 3: variable ratio drive without or with control system

The fixed ratio drive (type 1) is the simplest and the cheapest option. Transmission type 2 utilizes a load-disengaging device, allowing a wind turbine to start with minimal load and engage the load at a specific speed. This increases system efficiency at the expense of added cost and complexity. Transmission type 3 has the potential to attain near-optimal system efficiency for all loads, but their complexity and need for individual design for each load increase system cost. Figure 3-3 shows a schematic of different wind thermal energy conversion transmission systems.

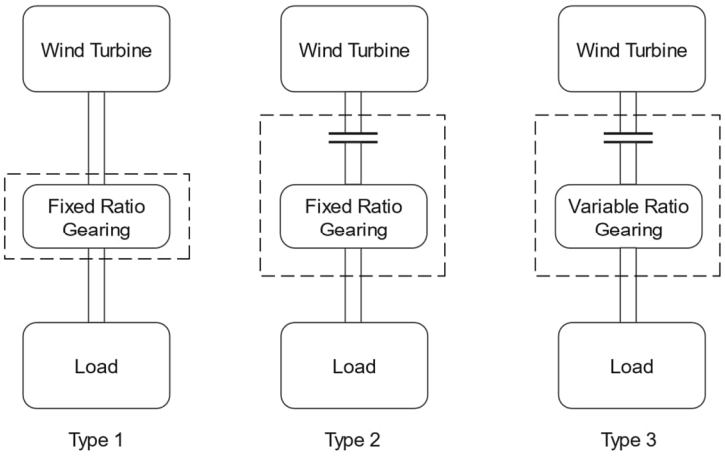

Figure 3-3: different transmission systems.

Due to the significance of simplicity in the development of WTES devices, type 1 transmission may be the optimal choice; nevertheless, the selection of the transmission system should be based on a thorough analysis of the load-matching requirements and desired system efficiency. Furthermore, it will be demonstrated that the use of type 1 transmission can still yield satisfactory system efficiency if the appropriate wind turbine is chosen, owing to the torque characteristics of the fluid agitator.

3.2.3 Load

Loads connected to wind turbines can generally be classified into three groups [34]. Load Type 1, such as multi-pole generators and non-geared hydraulic machines, has low starting torque and increases with speed [34]. Load type 2 has high starting torque with little increase in speed, such as positive displacement pumps with high static heads [34]. Load type 3 has moderate to high starting torque with a significant increase in speed, such as positive displacement pumps with substantial static and dynamic heads or generators/pumps with considerable drive train friction [34]. Figure 3-4 shows the torque-speed curve associated with these three types of loads.

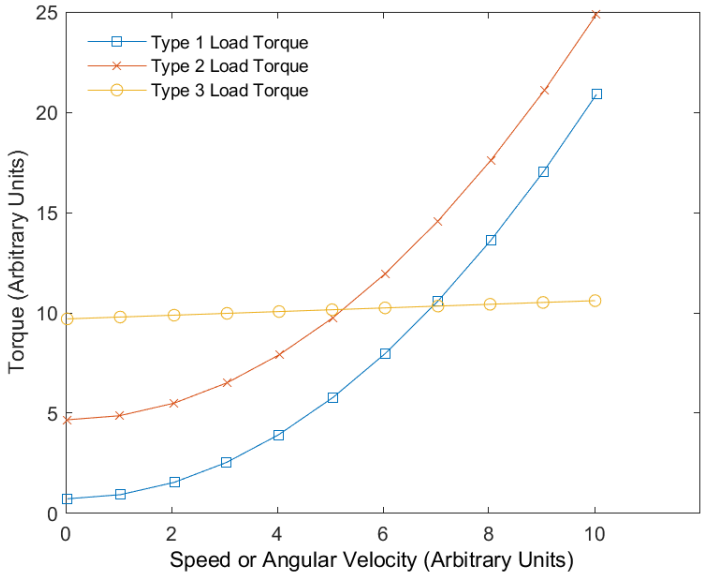

Figure 3-4: different type of loads that can be matched to wind turbine based on their torque-speed characteristic [34].

Very little information can be found in modern-day literature regarding using fluid agitators as heat generators. However, the chemical mixing industry has used agitator-type devices for fluid mixing processes, and from literature within that field, preliminary knowledge can be found regarding liquid agitators' power absorption and torque characteristics. For instance, Uhl and Gray found that the power absorption of impeller-type agitators was indeed proportional to the cube of rotational velocity at a high Reynolds number but, in laminar regions, proportional to the square of rotational velocity [79]. These relationships were detailed by Rushton, who found the following to be valid for a variety of impeller designs in baffled tanks in the turbulent region [80]:

$$P_{HG} = K\rho_{wf}D^5\omega^3 \tag{3.5}$$

Where K is the turbulent factor for a specific agitator configuration, D is agitator diameter (m), ρ_{wf} is the density of working fluid (kg/m^3), and ω is rotational speed (rad/s). The power

absorption equation for a high Reynolds number has several exciting and encouraging findings. For example, it was discovered that power absorption is directly related to the third power of rotational velocity, and that it depends on fluid density rather than viscosity, which is advantageous for applications such as water heating (density of water only varies by less than 1% from freezing to boiling while its viscosity decreases by 82% over the same temperature range) [80]. Additionally, industry literature reveals that the turbulent power absorption factor (K) remains constant for a specific agitator design once the transitional flow regime is exceeded. This factor was termed Power Number (N_P) and from equation 3.5 is defined as:

$$N_P = \frac{P_{HG}}{\rho_{wf} D^5 \omega^3} \tag{3.6}$$

And the agitator torque is:

$$\tau_{HG} = N_P D^5 \rho_{wf} \omega^2 \tag{3.7}$$

Equation 3.7 shows that the agitator's torque varies with the rotational velocity's second power. Therefore, by comparing equation 3.7 against 3.4, it can be concluded that the torque characteristic of the agitator is similar to that of the wind turbine, both proportional to the second order of rotational velocity. This significant outcome proves that fluid agitators can be matched to wind turbines.

3.3 Wind turbine-agitator performance analysis

To analyze the performance of the integrated system, it is necessary to understand the system mechanics, fluid mixing relationships, and thermodynamics. Therefore, the governing equations describing different system operation aspects are presented in the following sections. Then, the performance of the system under different operating conditions is assessed.

3.3.1 General governing equations

3.3.1.1 System mechanics

The wind-to-thermal system's governing relationship can be represented by Newton's second law applied to rotating systems or the conservation of angular momentum [59]:

$$\sum \tau_{System} = J_{System} \frac{d\omega}{dt} \tag{3.8}$$

Where τ_{System} denotes the summation of torques exerted on the system, J_{System} is the second moment of inertia for the system (turbine, transmission, and heat generator), and $\frac{d\omega}{dt}$ is the time rate of change of the system's angular speed. In equation 3.8, the torque and inertia components relate to the entire system rather than the turbine.

Expanding the torque relationship stated in equation 3.8 into individual components yields the subsequent expression [59]:

$$\tau_{WT} - \tau_{drag,Structure} - \tau_{bearing} - \tau_{HG} = J_{System} \frac{d\omega}{dt} \tag{3.9}$$

Where τ_{WT} is the torque that contributes to the rotational motion of the rotor, $\tau_{drag,Structure}$ is the resistive torque generated by drag acting on the rotating structure of the turbine (e.g., resistance due to struts and other structural members), and $\tau_{bearing}$ and τ_{HG} are the torques that resist the system rotation produced in the generator and bearings, respectively.

3.3.1.2 Thermodynamic analysis

The problem of a well-insulated vessel containing a fluid stirred by an external mechanism is a well-known scenario in thermodynamics (Joule experiment) [81], and it can be compared to the current investigation of the wind-to-thermal system, where a wind turbine replaces the traditional

electric motor as the source of external work input. In this regard, the physics can be mathematically described by applying the first law of thermodynamics to the heat generator tank [81]:

$$\frac{dE}{dt} = Q - W \tag{3.10}$$

Where Q and W represent the rates at which heat is transferred to the system and work is performed by the system, respectively. The total energy change of a system, E, can be analyzed by considering the change in kinetic energy, potential energy, and internal energy of the system. Given that there is no alteration in the system's height or contents, it is possible to exclude the gravitational potential term. In addition, if the time interval dt represents the system initially at rest and then at rest again after a period of revolution, the kinetic energy term can also be omitted. Under this scenario, equation 3.10 becomes:

$$\frac{dU}{dt} = Q - W \tag{3.11}$$

Where U is internal energy. The change in the system's energy is directly linked to its internal energy, resulting from the exchange of heat and work between the system and its surroundings. The specific internal energy between two states of the system can be determined by assuming that the heat transfer fluid inside the generator vessel is incompressible [81]:

$$u2 - u1 = \int_{T_1}^{T_2} c(T)dT \tag{3.12}$$

Where c is the specific heat capacity of the fluid in the system (for incompressible substances, $c_P = c_V = c$). By replacing equation 3.12 into equation 3.11 and changing the intensive specific internal energy property to extensive:

$$\frac{d}{dt}\int_{T_1}^{T_2} mc(T)dT = W \tag{3.13}$$

Where the mass of working fluid is assumed to be a constant. If the container is well-insulated, the energy lost to the surroundings due to temperature difference will be much less than the energy transferred from the generator impeller to the fluid. Thus, the heat transfer term, Q, can be ignored. The W refers to the power consumed by the generator as it transfers rotational shaft work to the internal energy of the working fluid. A common assumption is to omit the integral in equation 3.13 since the specific heat remains constant within the temperature range observed by the fluid in the vessel. By subtracting the integral and estimating the derivative as differences, the result can be simplified:

$$\Delta T = \frac{W}{(\rho_{water} V) c_p} \Delta t \tag{3.14}$$

Where the fluid volume, V, is represented as a design variable by expanding the mass parameter. Finally, by combining equation 3.14 and equation 3.5 and since $\dot{W} = \eta P_{WT}$ (assuming $\eta = 1$), vessel fluid temperature, ΔT, can be expressed as:

$$\Delta T = \frac{P_{WT}}{(\rho_{water} V) c_p} \Delta t \tag{3.15}$$

Where P_{WT} is the wind turbine (or electric motor) power output.

3.3.2 Rotor-shaft operation mode

Since wind velocity is rarely constant, it is feasible to adjust the angular velocity of the turbine rotor and impeller shaft to function in various manners, resulting in three distinct operating modes: constant angular speed, variable angular speed, and constant tip speed ratio. Among different methods, variable angular speed mode is a better option since other methods are either inefficient (constant angular speed) or complicated and costly (constant tip speed ratio) for the wind turbine-agitator system [33]. In the case of variable angular speed, the rotor-shaft angular velocity changes

as the wind velocity varies. By selecting this mode, it is also possible to use the type 1 transmission system, which is the simplest. Thus, it will result in reducing the system's complexity and cost.

3.3.3 System performance

3.3.3.1 Steady-state operation

Studying the steady-state operation of a wind-heater system, although challenging to achieve naturally, can provide valuable insights into its performance since this condition assumes a constant wind velocity and, therefore, constant rotor-shaft angular speed, which results in a constant tip speed ratio (λ) even if the system is designed with variable angular speed [34].

Nattuvetty demonstrated that in a constant wind velocity, the only torque fluctuations that occur within the cycle are due to discrete blade rotation [33]. These fluctuations, however, have minimal impact on the turbine's angular speed due to their high frequency and the system's high inertia. As a result, the system can be regarded as being in a steady state in practice.

Referring to equation 3.9, at steady-state, whereby definition there is no change in angular velocity, the relation described by equation 3.9 reduces to [59]:

$$\tau_{WT} = \tau_{drag,Structure} + \tau_{bearing} + \tau_{HG} \tag{3.16}$$

Equation 3.16 illustrates essential relationships for the functioning of the turbine-agitator system, particularly the consideration of the aerodynamic torque in the power produced by the turbine for its rotation, as well as the balance between the desired aerodynamic force generated by the rotor's blades and the resistive torque in the system at steady-state.

Kirke analyzed a specific type 1 wind turbine and generated a family of curves showing the relationship between τ and ω for different wind speeds, as depicted in Figure 3-5 [34]. By superimposing the $\tau - \omega$ of the turbine and $\tau - \omega$ curves of three type 1 agitator loads (labeled A,

B, and C in Figure 3-5, and considering an example steady wind speed of $7.5\,m/s$, it was found that a system with load A will operate at equilibrium at point 2, a system with load B at point 1 (which corresponds to $C_{P,max}$), and a system with load C at point 3 because the available torque matches the required torque [34].

Kirke also concluded that for slowly changing wind, the system can adapt by expanding or contracting the τ-ω curve [34]. If the wind speed increases to $10\,m/s$ (red curve), the operating point for the system with load B will move from point 1 to point 4 in Figure 3-5 or to point 6 if the wind speed decreases to $5\,m/s$ (yellow curve).

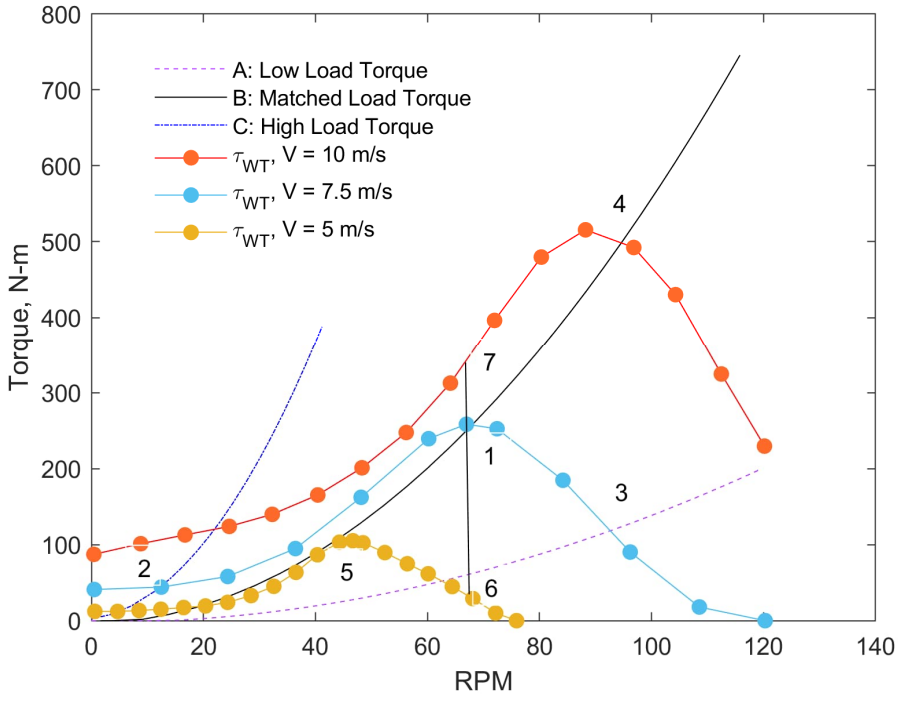

Figure 3-5: different type of loads that matched to a type 1 wind turbine [34].

3.3.3.1.1 Theoretical matching of agitator to wind turbine for steady-state operation

Designing the system based on a hypothetical steady-state operation case introduces the concept of theoretical matching between the wind turbine and heat generator, which can lead to the highest

possible performance (load type B). It is worth mentioning that this scenario was the only scenario considered in all previous publications regarding the design and sizing of the heat generator to be compatible with wind turbines. [30, 32, 41, 59].

Equations 3.4 and 3.7 showed that torque for both the wind turbine and fluid agitator varies with the square of rotational velocity, indicating that the wind turbine and agitator are intrinsically speed-matched. To achieve optimal operation, it's necessary to check the magnitudes of their torques by equating the torque generated by the turbine to that absorbed by the agitator. Thus, if the wind turbine runs at or near its $C_{P,max}$, maximum power point for any given wind turbine, as much as possible for the prevailing wind speed, the maximum system efficiency in terms of fluid temperature rise will be obtained. Assuming that friction forces are negligible ($\tau_{drag,Structure}$ and $\tau_{bearing}$), we will have:

$$\tau_{WT} = n\tau_{HG} \tag{3.17}$$

Where n is the gear ratio. For any given turbine, an optimally matched agitator can then be designed by rearranging equation 3.17 as shown below and using $N_P D^5$ as the design objective for the agitator. It is worth mentioning that water is considered a working medium in the analysis.

$$N_P D^5 = \frac{C_P}{\lambda^3 \rho_{water}} \left(\frac{\rho_{air} A R^3}{2n^3} \right) \tag{3.18}$$

All terms on the right-hand side of equation 3.18 are constant, where λ and Cp represent the optimal tip speed ratio and power coefficient for a given turbine. $N_P D^5$ can be used to select geometric variables for the agitator, irrespective of the turbine or wind conditions under the steady-state condition. This relationship demonstrates that there are no limitations on the physical design

of an agitator, as any element that resists fluid can generate heat. Therefore, the design should be guided by practical factors such as durability and versatility [33].

3.3.3.2 Transient operation

An intrinsic characteristic of wind energy is its intermittency, which includes gradual or sudden changes in wind velocity. As discussed in the previous section, the gradual change of wind velocity may not affect the system performance if the agitator is well-matched to the wind turbine. This is because the coupled system can adapt its speed to the wind speed, which can be considered a steady-state operation.

As evident, the system's steady-state equilibrium cannot be achieved, specifically during the start-up process or when the wind speed is suddenly changing, until a balance of torques is achieved. However, the system's ability to overcome resistive loading during its transient phase is significantly complex due to variable angular speed ($\frac{d\omega}{dt}$) caused by unbalanced torques, as stated in equation 3.9.

To simplify the problem, we will not consider the start-up process in our analysis. Heat generator design for the start-up process must consider the resistive forces under laminar conditions, which differs from the agitator power absorption in turbulent conditions.

Assuming the system is successfully started up, Kirke showed that under varying wind conditions, if either the wind turbine or the load has high inertia (J_{System}), it will take a significant time for the system to adjust to a new steady state operating point [34]. When the wind velocity decreases suddenly from 7.5 to $5\ m/s$, the wind turbine operates inefficiently and produces less torque and power (point 6) than it could at that wind velocity (point 5), as shown in Figure 3-5. On the other hand, if the wind speed increases abruptly, the torque and power available (point 7) for accelerating

the system will be significantly less than the torque and power available at the new equilibrium point (point 4), resulting in reduced system efficiency.

Kirke concluded that type 1 wind turbines perform well in consistent winds and are more adaptable to changes in wind speed, but they experience decreased efficiency during gusty conditions [34].

He suggested two design parameters to be considered to minimize this loss:

(i) system inertia should be minimized;

(ii) the $C_P - \lambda$ curve should be as flat as practicable.

Although the above solutions are essential to improve the system performance under transient operation, the characteristics of the load under transient operation (heat generator resistive torque) have been assumed to be the same as under steady-state operation. As shown in the following sections, there is little available literature about the agitator's torque characteristics and power absorption behavior under variable shaft speed, even in the process industry. Since this thesis focuses on understanding the criteria for designing an optimized heat generator based on fluid agitation that can be matched to a wind turbine in any operating conditions, assessment of the transient operation of the agitator is critical.

3.4 Analysis of agitator power absorption

Equation 3.18 shows that the agitator's design, mainly the impeller, for heat generation is entirely unrestricted, meaning that any element moving in a tank will convert mechanical energy to thermal energy. Therefore, the design should be followed by considering $N_P D^5$ as the design criteria. At this point, the main objective will be understanding the behavior of τ_{HG} in equation 3.16. τ_{HG} is also known as the hydrodynamic torque, which is the resistive force generated on the impeller's blade and shaft due to rotation inside the tank filled with a working fluid. The resultant torque for

the agitator was presented in equation 3.7. However, the impeller Power Number (N_P) needs to be known to calculate the torque and absorbed power of the agitator by this equation.

The research on the power characteristics of impellers dates back over 150 years, starting with the first publication on the topic in 1855 [82]. Although a direct mathematical relation to obtain a theoretical power equation is lacking, ample literature on empirical data can be examined for qualitative analysis and to determine the optimal choice for this experimental study.

The physical form or operation category determines the classification of an impeller, and there are various types, such as propellers, turbines, paddles, and high-shear impellers [83]. It has been shown that studying the flow field characteristics of tanks stirred by these impellers is essential for understanding their performance parameters and their impact on mixing time and mass transfer in tanks [84]. Understanding the generated flow fields has thus made it easier to select the appropriate impeller for specific usage and assist in improving the design. The available literature suggests that radial turbines produce turbulent flows, making them suitable for various applications, including homogenizers, colloidal mills, and emulsifiers [85]. In our study, like all past studies that designed agitators for heat generation, a radial-type impeller is considered for the experimental analysis.

3.4.1 Dimensionless analysis

The power consumption of the impeller in a vessel is influenced by various factors such as rotational speed, external forces, fluid properties, and the geometry of the impeller and vessel, which can be determined using Buckingham pi and dimensional analysis to obtain twelve dimensionless groups. Equation 3.19 presents the twelve dimensionless groups obtained by Buckingham's Pi theorem for a cylindrical vessel with a central impeller:

$$f\left(\frac{\rho NL}{\mu}, \frac{N^2}{g}, \frac{P}{\rho N^3 D^5}, \frac{D}{D_T}, \frac{D}{Z}, \frac{D}{C}, \frac{D}{p}, \frac{D}{w}, \frac{D}{l}, \frac{n_2}{n_1}, \frac{D}{B}, \frac{D}{l_b}\right) = 0 \quad (3.19)$$

The equality of the first three dimensionless terms guarantees dynamic and kinematic similarity between two geometrically similar vessels. In addition, the geometric similarity is determined by the last nine groups of the equation, showing that various factors can affect vessel power consumption, with certain factors being more significant than others. In further, the definition of the dimensionless groups is provided.

The first term in the above equation is Reynolds number, Re, which is the ratio of inertial forces to viscous forces [86]. It is defined as:

$$Re = \frac{\rho NL}{\mu} \quad (3.20)$$

L represents a characteristic length, N represents velocity, and μ represents the fluid viscosity. For agitation, impeller diameter, D, is employed as characteristic length, and the velocity is proportional to the impeller tip speed. It can be replaced by the product of impeller rotational speed and the impeller diameter:

$$Re = \frac{\rho D(\omega D)}{\mu} = \frac{\rho \omega D^2}{\mu} \quad (3.21)$$

The second dimensionless group in equation 3.19 is the Froude number (Fr) which is the ratio of inertial force to gravity force. It is defined as:

$$Fr = \frac{N^2}{g} = \frac{\omega^2 D^2}{g} \quad (3.22)$$

Where D is impeller diameter and ω is the rotational velocity of the impeller.

The third dimensionless term is Power Number (N_P), introduced in equation 3.6. The N_P and the drag coefficient for an immersed body are analogous, allowing us to understand their physical significance better and identify similarities between them. The N_P can be obtained from the drag coefficient equation. The drag coefficient can be expressed as:

$$C_d = \frac{2F}{\rho v^2 A} \tag{3.23}$$

Using the relations $v \propto ND$, $A \propto D^2$, and $P \propto NDF$, the following proportional relations are derived.

$$C_d \propto \frac{P}{\rho N^3 D^5} \tag{3.24}$$

$$C_d \propto N_P \tag{3.25}$$

A concise relationship can be summarized for the relationship between the Re, Fr, and N_P in a geometrically similar vessel.

$$N_P \propto (Re)^a (Fr)^b \tag{3.26}$$

The impact of the Fr on kinematic and dynamic similarity is minimal in fully baffled systems, as opposed to unbaffled systems, due to the absence of vortex formation, thus allowing for the simplification of the correlation between the N_P and Re in the investigation [83].

Plotting the different dimensionless groups on a graph is the most effective way to represent their correlation visually. However, focusing only on the groups responsible for kinematic and dynamic similarity is essential to avoid a cluttered graph. Figure 3-6 shows that the N_P of impellers with different geometrical configurations for a baffled system reaches a constant value at high Re [86]. However, it is a misconception that only the Re is sufficient to determine the power input required

by an agitator, as the dynamic similarity is only valid for a particular geometric configuration, and any changes in geometric parameters would yield different results.

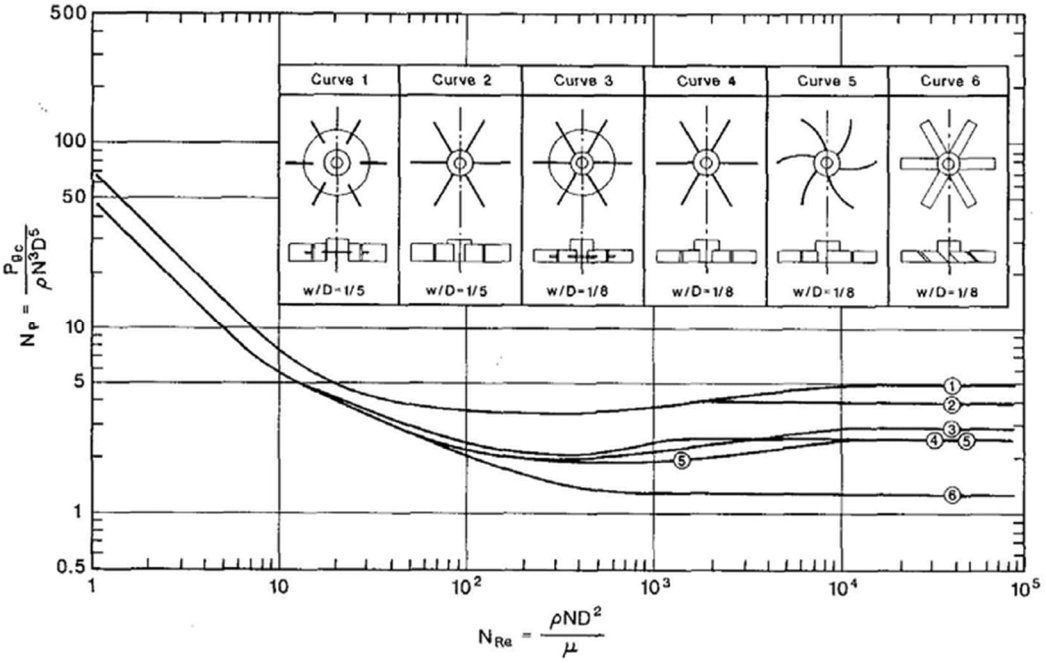

Figure 3-6: N_P vs. Re for different impellers [87].

Bates et al. [87] conducted a comprehensive study on multiple radial-type impellers, finding that an increase in Re leads to a decrease in N_P, eventually becoming constant in a fully turbulent flow. In addition, it was found that the N_P was influenced by factors like the number and width of the blades and the impeller clearance from the bottom of the tanks [87]. These results were expanded by other researchers, including Nienow and Miles [88], King et al. [89], Nagata [90], Bujalski et al. [91], and Xanthopoulos and Stamatoudis [92], who incorporated additional variables like tank size, shape, system scale, and blade/disk thickness. For example, it was demonstrated that the N_P decreases linearly as the blade thickness increases, which can be attributed to the impact of the blade/disk on flow separation [93-94].

In addition, Aiba [95] demonstrated that the liquid rotates as a solid body in a vessel without baffles, creating a free vortex independent of the impeller type and speed. However, baffles disrupt the flow and prevent the vortex formation in a baffled tank [96]. A fully baffled configuration for a given vessel is characterized by the highest relative N_P of the impeller compared to an unbaffled vessel [87].

Bates et al. [87] determined that a baffle ratio of 0.4 is the most efficient for any Flat Blade Turbine (FBT) diameter, as a further increase in baffle length will reduce the N_P. Nagata et al. [82] observed the same trend. Still, they specified 0.5 as the optimum baffle ratio. The baffle ratio is expressed as:

$$Baffle\ Ratio = \frac{n_b w_b}{D_T} \tag{3.27}$$

Where n_b represents the number of baffles and w_b / D_T denotes the ratio of baffle length to tank diameter. Using four baffles, where each baffle width is 10% of the tank's diameter, is regarded as a fully baffled setup.

3.4.2 Agitator transient power consumption

In many process industries where high mixing efficiency is concerned, tanks are equipped with baffles. Under these conditions, the flow field is chaotic, and a high level of turbulence is generated even if the impeller of agitator mixers rotates at a constant rotational speed [84]. However, the transient operation of the impeller with variable shaft speed, known as unsteady mixing, has also been suggested as an active control method to increase the turbulence inside the unbaffled tanks to improve the mixing efficiency [97-103]. Unbaffled tanks are commonly utilized in industries like food and pharmaceuticals where installing baffles is impractical or ineffective due to concerns

about cleaning the vessel interior, particle growth disturbance in crystallization, and catalyst agglomeration in catalytic processes [97].

In a study by Gao et al. [98], velocity measurements were conducted in a tank stirred by a Rushton turbine at a mean Re of 1145, using both steady and square wave shaft speed protocols, and the findings indicated a notable increase in turbulence intensity and radial jet width in the square wave scenario. Roy and Acharya [99] simulated the flow field of a Rushton impeller with the same configuration and Reynolds number as Gao et al. [98], resulting in a 20% increase in power consumption. It was determined that employing a protocol with varying shaft speeds would enhance the efficiency of mixing applications. Nevertheless, some drawbacks are linked to this method. If a variable speed protocol includes sudden changes in shaft speed, spikes in the shaft torque can cause mechanical wear in the mixer [100]. Furthermore, the rise in mean power consumption must be considered when assessing process efficiency, particularly in the case of an industrial-scale system. It was concluded that it is critical to have a more comprehensive understanding of the transient torque and power consumption before designing such systems.

Li and Xu [103] selected an unbaffled tank to investigate the enhancement of mixing efficiency by applying a forward-reverse rotating impeller. Numerical analysis revealed that the tank's flow field and power characteristics varied over time due to the forward-reverse agitation, as opposed to the relatively stable flow field observed in tanks with constant agitation. In addition, they calculated impeller power numbers in unbaffled and baffled tanks with unsteady and steady agitations. Comparing the results, it was found that the impeller power number is the smallest in the unbaffled tank at a constant speed, followed by the baffled tank with continuous agitation, and the largest in the unbaffled tank with transient agitation [103].

The importance of understanding the power demand in baffled tanks with transient operation for WTES application can be concluded from the findings and other studies on the power characteristics of mixing agitators in unbaffled tanks with unsteady mixing in the process industry.

The governing equation that describes the system in the transient stage is presented in equation 3.8. Applying this equation to an agitator tank will give:

$$\tau_{in} - \tau_{fr} - \tau_{hydro} = J_{System} \frac{d\omega}{dt} \tag{3.28}$$

In this equation, τ_{in} is the provided torque by either a wind turbine or an electric motor, τ_{fr} is the torque associated with friction in the drivetrain, and τ_{hydro} is the resistive torque generated because of fluid motion inside the tank. The right-hand side of equation 3.28 ($J_{System} \frac{d\omega}{dt}$) is also known as inertia torque since it is the required torque to overcome the system's inertia. To have a transient agitation, the driver should be able to overcome the sum of all the resistive torques. However, when analyzing the impeller's N_P, τ_{hydro} is the only concern.

τ_{hydro} is characteristic of the pressure and viscous forces exerted on the impeller by the fluid. The hydrodynamic drag is primarily caused by the pressure forces generated by the separated flow on the impeller faces, and torque is a reliable measure of various physical conditions during the transient process. The torque measurement offers valuable insights into the overall behavior of the flow field, even though it does not give a detailed description of velocity and vorticity fields. As a result, the objective of the experimental analysis in this study is to quantify the τ_{hydro} produced due to varying rotational velocity in the baffled tank.

3.5 Summary

This chapter comprehensively analyzed the various components constituting the entire system. The examination primarily focused on evaluating the governing equations, which serve as the foundation for comprehending the physics of the system. Furthermore, a critical assessment was conducted to determine the compatibility of the wind turbine with the agitator load, both in terms of steady-state and transient operation. These evaluations were undertaken carefully, ensuring that all aspects of the system's behavior were thoroughly assessed. In addition, a detailed analysis was carried out to examine the behavior of the agitator load under both steady-state and transient operations. It has been demonstrated that the effective operation of wind-powered heat generators in real-world scenarios necessitates a comprehensive understanding of impeller rotation within baffled tanks under transient conditions. Therefore, in focusing solely on the fluid agitator, the primary concern of this thesis, and omitting wind turbine operational characteristics at this stage, we conclude that designing the fluid agitator for a steady-state scenario is feasible. This is due to understanding the agitator's behavior under such operating conditions. Conversely, it has been revealed that the challenge in agitator design lies in transient operation, where the behavior of the agitator is unknown.

Chapter 4 Experimental setup and methods

4.1 Introduction

In this chapter, first, the experimental setup developed in this research is presented. Next, the importance of signal processing is discussed, and then the method applied to filter the torque signals is explained. Next, the uncertainty analysis method is provided to measure the uncertainties associated with the results. Then, the experimental procedure followed for performing the experiments is presented. Finally, the data analysis procedure is explained in detail.

4.2 Experimental setup

The schematic of the developed experimental setup is presented in Figure 4-1. Experiments were conducted in a cylindrical, baffled stainless steel tank (Figure 4-2). The SS Grade 316 was selected for the construction of the tank due to its corrosion-resistant nature and good mechanical properties [104]. The tank has an inner diameter of $D_T = 200\,mm$ and a height of H equal to its diameter. Four baffles were added to the tank, each $1/10th$ of diameter, to ensure a fully turbulent flow. The liquid used for the investigation was distilled water at room temperature.

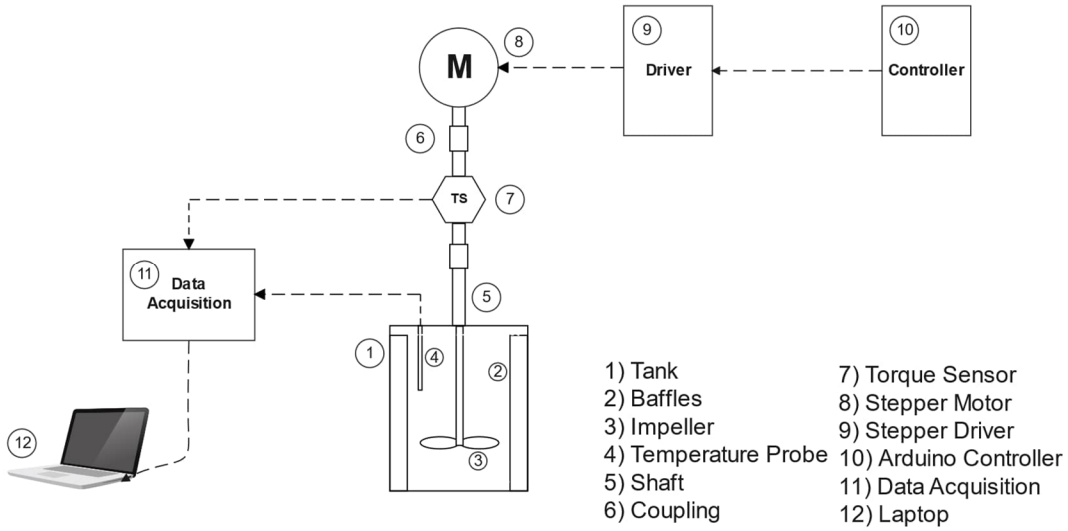

Figure 4-1: schematic of the experimental setup developed for this study.

Two radial four-bladed FBTs with different geometrical characteristics were selected to investigate the effect of impeller geometry on the measurements for experiments (Figure 4-3). Both impellers were 3D printed using plastic material to minimize the impact of inertia ($J_{Impeller}$) on the resulting torque during the variable angular speed motion. The impellers were designed in a manner that enabled them to be mechanically connected to the shaft using a screw. Each impeller was mounted on a small diameter ($10\ mm$) steel shaft at the tank's $2D_T/3$ height. It was also tried to select the smallest shaft size possible to minimize the effect of inertia (J_{Shaft}) on the measurements. In addition, a housing structure was created to attach the motor and support the shaft, with the housing being welded to the top cover of the tank. It also incorporates four holes in the cover to secure it to the tank to prevent vibration and fluid leakage.

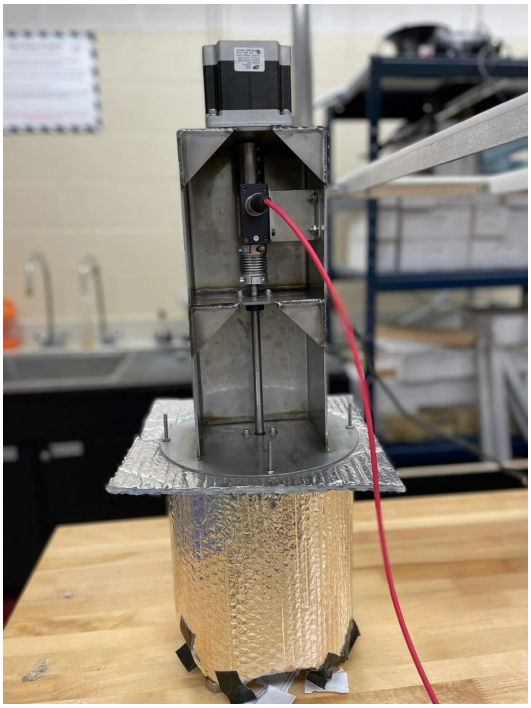

Figure 4-2: the experimental setup developed for this study.

The impellers were powered by a stepper motor (Applied Motion Products, HT34-695) and stepper drive (Applied Motion Products, STAC5) in micro-stepping mode (2000 steps per rotation) to ensure smooth motion. In addition, an Arduino controller (Arduino Mega 2560), which supplied the motor with a TTL signal, was utilized to control the motor. A rigid coupling was mounted between the motor and torque sensor, and a flexible coupling (R+W BKL) was considered to attach the torque sensor to the steel shaft. Two bearings were mounted on the shaft to limit the lateral movement and align the shaft with the motor centerline. Shaft torque was measured using an in-line torque transducer (TRS605, FUTEK), while shaft rotational speed was monitored using an optical encoder (2×360 PPR) embedded in the torque transducer. The default acquisition system (USB520, FUTEK) was primarily utilized for obtaining the torque signal, enabling a maximum acquisition rate of 4,800 Samples Per Second. The torque sensor's output signal is transmitted to the USB520 data acquisition system through a shielded wire, with the output being measured in

mV instead of $N{\cdot}m$ or $lb{\cdot}in$ units, but the data was subsequently converted to $N{\cdot}m$ using the vendor's default data acquisition software (SENSIT, FUTEK). To measure fluid temperature, a thermocouple probe (J-type) was used with a CompactDAQ Chassis (NI-9178, National Instrument) and a Temperature Input Module (NI 9211, National Instrument). Finally, the data were collected and analyzed using a Microsoft Windows Operating System PC.

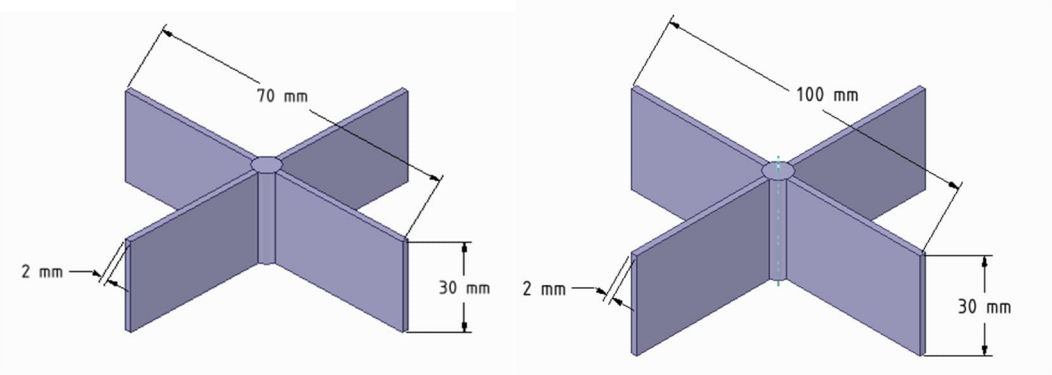

Figure 4-3: 3D printed Four-bladed Flat Blade Turbine impellers for experimental study ($FBT-07$: Blade Dia. = 70 mm, Blade Height = 30 mm, Blade Width = 2 mm, $FBT-10$: Blade Dia. = 100 mm, Blade Height = 30 mm, Blade Width = 2 mm)

4.3 Signal processing

Mixers rotating in fluids produce noisy torque signals, with the dominant excitation frequencies being the rotational speed of the impeller and the blade passing frequency. Moreover, despite using shielded wires, the torque sensor is susceptible to electromagnetic interference from the stepper motor and laboratory electronics. In addition, mass imbalance in the shaft results in cyclic load, which is picked up by the torque sensor. The presence of these factors results in unwanted signals in the final output, necessitating a filtering process to eliminate these noises before utilizing the torque value in subsequent analyses.

Among different methods, ensemble averaging is a recommended method in the literature for filtering noisy torque signals in agitation mixers, and it is utilized in this study for signal processing. The noise filtering technique used in this method is explained below.

4.3.1 Ensemble averaging

Ensemble averaging is a signal processing technique that reduces noise by simply computing averages of repeatable signals, which can come from multiple sensors or repeated measurements of the same experiment, assuming the systems can produce highly repetitive responses to many repeating experiments [105]. A time reference must be established to align all signals and create a standard time frame to generate an ensemble average. This allows for constructing an average signal by averaging corresponding points from each signal within the time frame. The process is repeated for each sample in the time frame to obtain the complete averaged response [105].

The results of employing the ensemble averaging technique to filter out noise from 1200 raw signals of ten repeated experiments are graphically represented in Figure 4-4. It is worth mentioning that the raw signals in Figure 4-4 depict only measurements for one experiment to avoid confusion. As can be seen, applying ensemble averaging resulted in significant noise reduction and, therefore, having smoother signals in contrast to the unprocessed signals.

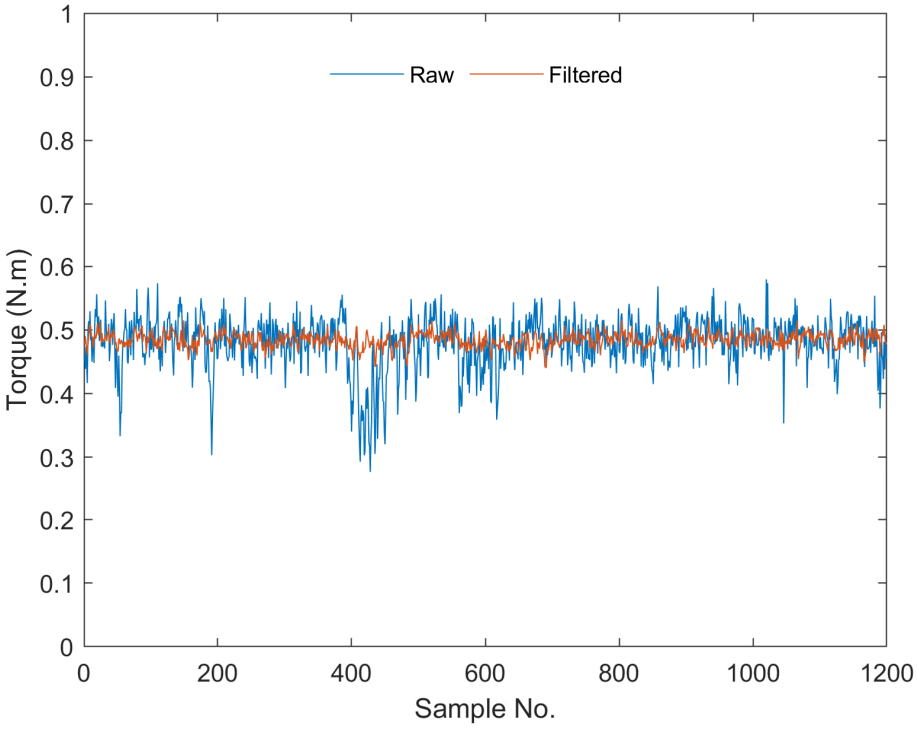

Figure 4-4: raw and filtered torque signal using ensemble averaging method.

4.4 Uncertainty analysis

Systematic uncertainties are reproducible inaccuracies that are consistently in the same direction and could be caused by an artifact in the measuring instrument. Although systematic uncertainty is inherent in all measuring instruments and cannot be eliminated from experimental studies, a thorough understanding of them is necessary as it assures that the actual value falls within the reported range.

Table 4-1: measurement uncertainties.

Parameter	*Uncertainty*
Temperature	±0.5 ℃
Torque	±0.01 $N.m$
Angular Velocity	±0.5 RPM
Volume	±0.05 Liters
N_P	0.31%
P_{in}	12.67%

Calculating the systematic uncertainty of a dependent variable can be determined by assessing the systematic uncertainties associated with the independent variables. Equation 4.2 demonstrates the uncertainty, symbolized as δR, of a value R that is a product of the independent variables represented by X [105].

$$R = X_1^a X_2^b X_3^c \dots X_M^m \tag{4.1}$$

Then

$$\frac{\delta R}{R} = \left\{ \left(a \frac{\delta X_1}{X_1} \right)^2 + \left(b \frac{\delta X_2}{X_2} \right)^2 + \left(c \frac{\delta X_3}{X_3} \right)^2 + \cdots + \left(m \frac{\delta X_M}{M} \right)^2 \right\}^{1/2} \tag{4.2}$$

The systematic uncertainties associated with the equipment used in this study are listed in Table 4-1. The dependent variables computed in this investigation are the impeller's N_P and the P_{in}. The

level of uncertainty associated with the impeller N_P is determined to be 0.31% for tests conducted at lower rotational velocities, resulting in small torques. Furthermore, the uncertainty of the P_{in} resulting from inaccuracies of the instrument measurements is 12.67%.

4.4 Experimental procedure

Experiments were performed across a range of nondimensional parameters as specified in Table 4-2. All experiments were conducted with the tank filled with distilled water to ensure no free surface above the water level. The positioning of the impellers was such that the highest points of the impellers were located 134 mm below the tank's cover (with a clearance of 66 mm from the tank's bottom). All the experiments with transient operation were carried out according to the following procedure.

1. After starting the motor, the impeller was speeded to the initial velocity (ω_1).
2. The impeller was allowed to undergo continuous rotational motion at a consistent rate ($\alpha_1 = 0$) for 30 seconds. This ensured that the steady-state condition was achieved before the initiation of transient operation.
3. Subsequently, a phase of transient motion featuring varying angular velocity ($\alpha_1 \neq 0$) was initiated and undergone which, as a result, the velocity of the impeller reached the desired final velocity (ω_2).
4. The impeller rotation at ω_2 continued until the condition of mean flow steady-state was again maintained for a sufficient time (30 seconds).

For every dataset, as previously explained, the resultant torque is a combination of the hydrodynamic torque, the torque needed to overcome the inertia during the transition stage, and the torque needed to overcome the friction in the shaft bearings. In all cases, the torque necessary to overcome inertia is negligible since it was tried to construct the system with the least possible amount of inertia. Furthermore, the magnitude of

the friction torque exerted by the bearing was also negligible in comparison to the hydrodynamic torque in all cases. A transient experiment was conducted to measure and compare the torque when the tank was empty and filled with the working medium to quantify the effect of inertia and friction torque. It was seen that the torque necessary to overcome inertia and friction was less than 5% of the minimum torque in the studied range. The result of the test will be presented in section 5.2.

Table 4-2: range of studied parameters.

Impeller	*Re*	*w/D*	D/D_T	*Angular Velocity (rad/s)*	*Acceleration (rad/s^2)*
FBT-10	19,950 – 69,900	0.3	0.5	12.57 – 37.7	1 – 62.83
FBT-07	14,500 – 39,900	0.43	0.35	18.85 – 43.99	1 – 62.83

4.5 Data analysis

In this study, a sample frequency of 100 HZ was selected for the data acquisition process, resulting in a substantial amount of data sets for each run. Therefore, data analysis was critical before interpreting the measured torque signals. As previously mentioned in section 4.4, the time domain of the experiment for the transient analysis of impeller motion was divided into three sections. The initial section involved the impeller operating at a constant rotational speed, followed by a transient phase where the impeller's rotational speed varied based on the acceleration requirement, and ultimately, another steady-state section where the impeller rotated at a constant speed. According to equation 3.7, if the rotational velocity remains constant, it can be concluded that the torque should also remain constant in theory, as the other variables are also held constant. Consequently, to present the data, the measured torque values obtained during the steady-state operation are averaged from 100 samples per second to 1 sample per second. However, regarding the transient

operating segment, the collected data from the data acquisition process was subjected to averaging to yield a frequency of 10 samples per second. This was undertaken to enhance comprehension of the flow properties exhibited during this stage. Figure 4.5 presents the procedure for this study's data acquisition and analysis. In addition, a curve-fitting approach (polynomial or cubic) was implemented to find a trend in the experimental measurements. It is worth mentioning that MATLAB software [107] was used for all the signal processing and data analysis purposes.

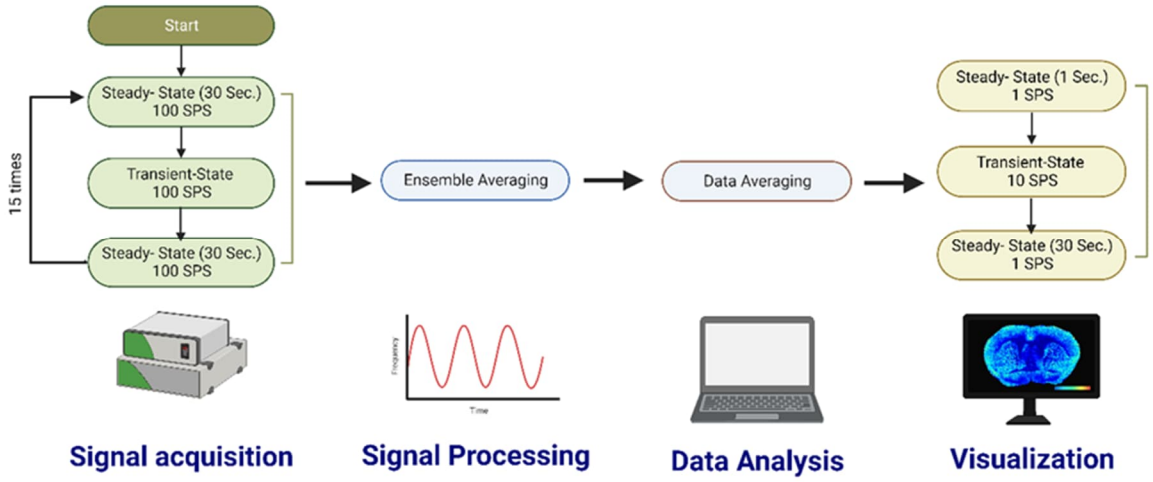

Figure 4-5: the procedure for data acquisition and data analysis.

4.6 Summary

This chapter presented the details of an experimental setup designed and developed for this study. Furthermore, specific attention was given to the techniques utilized for the signal processing and the method employed for conducting a comprehensive analysis of uncertainties. Next, the procedure for carrying out the tests was explained in detail. Finally, the data analysis method utilized to process the datasets was presented.

Chapter 5 Results and discussion

5.1 Introduction

This chapter is dedicated to the experimental study of the agitator performance. In this regard, a series of tests were performed on the developed agitator to examine the flow characteristic inside the tank under different operating conditions, including steady-state and transient. The torque exerted on the shaft and the rise in temperature of the fluid were measured, and the results were assessed to understand the agitator's behavior during its operation.

5.2 Effect of friction and inertia torque on measurements

The measured torque by the torque sensor is the total torque exerted on the shaft, which, based on equation 3.28, consists of hydrodynamic torque, friction torque, and inertia torque. Since the main objective of this study is to get insight into the characteristics of the flow field during transient conditions by measuring the hydrodynamic torque, it is essential to assess the effect of the inertia and friction torque on the collected data. For this purpose, two different experiments were performed using $FBT-07$ impeller, one in the empty tank and the other in the tank filled with water. The test conditions for these experiments are presented in Table 5-1. In the case of the empty tank, the friction torque resulting from the air inside the tank is assumed to be negligible.

Table 5-1: test conditions for assessing friction and inertia torque on the total torque.

Impeller	$\boldsymbol{\omega_1}\ (\frac{\boldsymbol{rad}}{\boldsymbol{s}})$	$\boldsymbol{\omega_2}\ (\frac{\boldsymbol{rad}}{\boldsymbol{s}})$	$\frac{\boldsymbol{d\omega}}{\boldsymbol{dt}}\ (\frac{\boldsymbol{rad}}{\boldsymbol{s^2}})$
FBT-07	25.13	37.7	62.83

The results for both experiments are presented in Figure 5-1. As can be seen, the sum of friction and inertia torque within the empty tank was almost constant, having a value of $0.002\ N.m$. This result indicates that the high acceleration rate of $62.83\ \frac{rad}{s^2}$ did not considerably affect the total torque. This proves that the effect of system inertia (J_{System}) on the total measured torque was small. On the other hand, the total torque when the tank is filled with water increased from $0.037\ N.m$ to around $0.082\ N.m$ when the ω increased from $25.13\ \frac{rad}{s}$ to $37.7\ \frac{rad}{s}$ with the acceleration rate of $62.83\ \frac{rad}{s^2}$. This, in turn, shows that the most dominating torque was from the fluid (water) resistance inside the tank, while the sum of friction and inertia torque had less than 6% effect on the total torque. Thus, in this study, we assumed that the total torque equals the hydrodynamic torque for simplicity.

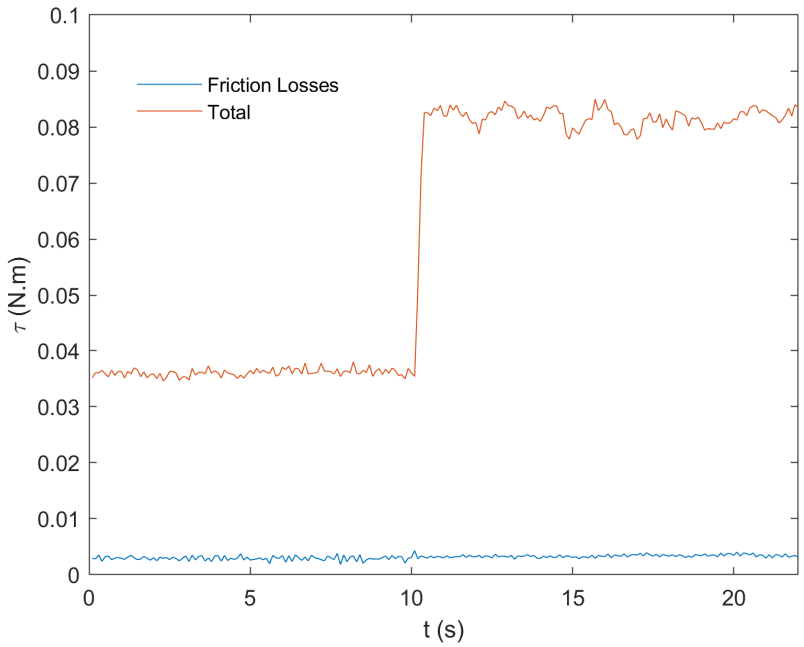

Figure 5-1: results of the total torque and the sum of inertia and friction torque for the experimental test condition presented in Table 4-2.

5.3 Steady-state analysis

To validate the measurements, and to establish a baseline for comparison with transient operations, a series of steady-state tests were conducted to obtain the power number N_P for each impeller across the defined Reynolds range. Each test was performed at constant rotational velocity for 60 seconds.

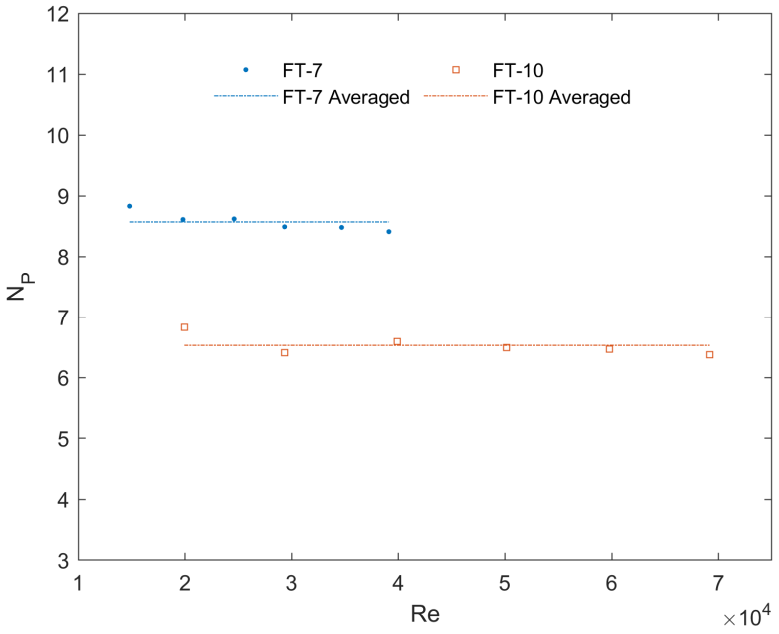

Figure 5-2: results of N_P across the Reynolds range for $FBT-10$ and $FBT-07$.

Figure 5-2 presents the results of N_P over different Reynolds for the two impellers. The $FBT-10$ has a steady state N_P of 6.6, while the N_P for $FBT-07$ is 8.5. The power number is almost constant for each impeller in the studied Reynolds range. This trend agrees with those reported in the literature [87]. In addition, Table 4 presents the results of steady-state N_P for $FBT-10$ as compared to the data reported in Ref. [87]. As it can be seen, the steady-state N_P for $FBT-10$ in this research is close but slightly higher (by 0.6) than the reported value in Ref. [87]. The difference is mainly because of the higher width of baffles (w_b) in this research compared to Ref. [87], which generated more resistance to flow circulation inside the tank.

Figure 5-2 presents the results of N_P over different Reynolds for the two impellers. Based on the results, the $FBT-10$ has a steady state N_P of 6.6, while the N_P for $FBT-07$ is 8.5. As it is clear, N_P is almost constant for both impellers in the studied Reynolds range, which is in complete agreement with the available data in the literature [87]. In addition, Table 5-2 presents the results of steady-state N_P for the $FBT-10$ compared to the data reported in Ref. [87]. As it can be seen, the steady-state N_P for $FBT-10$ in this research is close but slightly higher than the reported value in Ref. [87]. The difference is mainly because of the higher width of baffles (w_b) in this research compared to Ref. [87], which generated more resistance to flow circulation inside the tank.

Table 5-2: the results of steady-state N_P in this study and Ref. [87].

	Impeller Type	**No. of Blades**	***w/D***	***D/D$_T$***	$\frac{C}{H}$	n_b	w_b	N_P
This study	**FBT**	4	0.3	0.5	1/3	4	$D_T/10$	6.6
Ref. [87]	**FBT**	4	0.3	0.5	1/3	4	$D_T/12$	6

5.4 Transient analysis

Understanding the fluid agitator's hydrodynamic torque and power number characteristics during transient operation will help better assess the WTES performance during intermittent wind. In this regard, different tests were designed to investigate the effect of variable shaft motion on fluid agitators, including 1) acceleration, 2) deceleration, and 3) sinusoidal velocity profiles.

5.4.1 Acceleration

This section investigates the effect of impeller acceleration on the fluid agitator's transient hydrodynamic torque and power number.

5.4.1.1 Effect of different acceleration rates on torque (τ) and power number (N_P)

The hydrodynamic torques exerted on the $FBT-07$ and $FBT-10$ impellers when the acceleration rate changed from 1 to $62.83\ \frac{rad}{s^2}$ are shown in Figure 5-3 and Figure 5-4. The test conditions of these experiments are tabulated in Table 5-3.

While increasing the rotational speed increased the torque for both impellers, the results suggest that the (final) steady-state torques were constant and the same for each impeller despite the acceleration rates. With higher acceleration rates, the time to reach the final rotational speed (ω_2) declines, resulting in a steeper torque increase. For example, when the rate of acceleration was $1\frac{rad}{s^2}$, both impellers reached ω_2 in 12 seconds accompanied by a gradual rise in torque. When the acceleration rate was $62.83\ \frac{rad}{s^2}$, it took less than 3 seconds for both impellers to pass the transient phase, thus resulting in an abrupt increase in the torque.

Table 5-3: test conditions for transient operation with different acceleration rates.

Impeller	$\omega_1\ (\frac{rad}{s})$	Re_1	$\omega_2\ (\frac{rad}{s})$	Re_2	$\frac{d\omega}{dt}\ (\frac{rad}{s^2})$
FBT-07	25.13	19561	37.7	29341	1 – 62.83
FBT-10	12.57	19960	25.13	39920	1 – 62.83

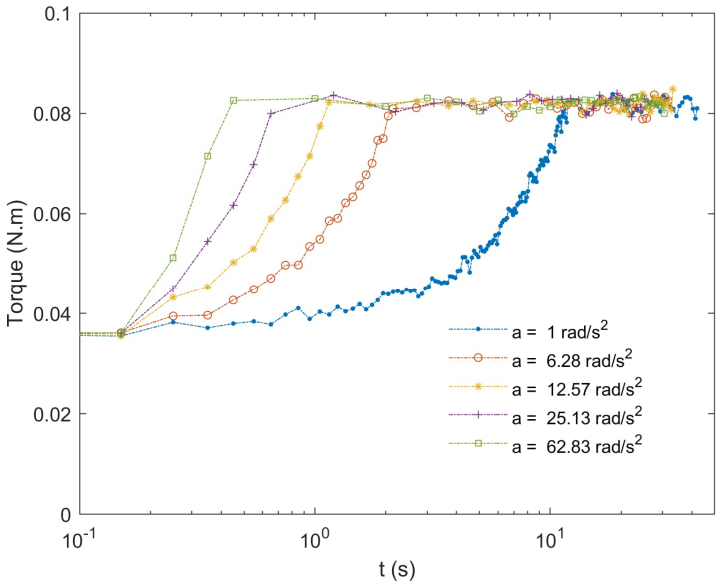

Figure 5-3: results of changing acceleration rate on torque for $FBT-07$ ($\omega_1 = 25.13\frac{rad}{s}, \omega_2 = 37.7\ \frac{rad}{s}$).

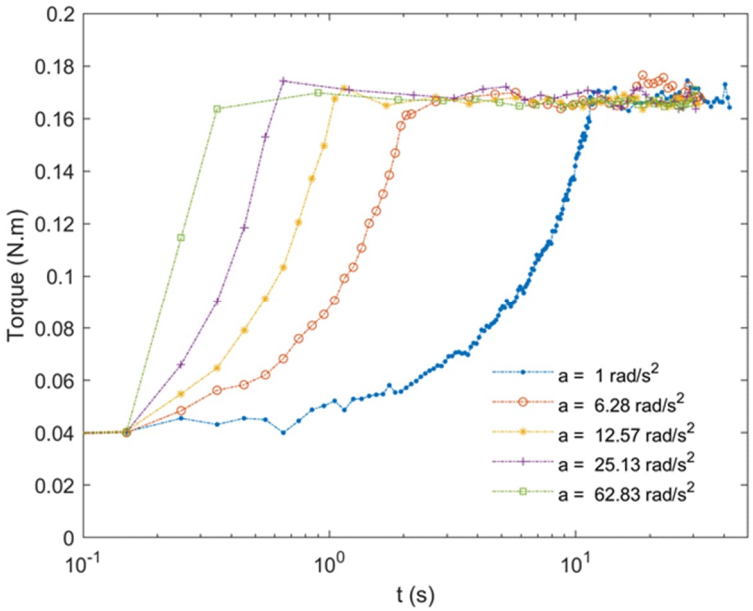

Figure 5-4: results of changing acceleration rate on torque for $FBT-10$ ($\omega_1 = 12.57\frac{rad}{s}, \omega_2 = 25.13\ \frac{rad}{s}$).

The measured power numbers (N_P) with different acceleration rates are presented in Figures 5-5 and 5-6 for $FBT-07$ and $FBT-10$ respectively. A logarithmic time scale is used to present N_P to closely examine how N_P behaves in the transient stage. As it can be seen, when the acceleration rate is $1\ \frac{rad}{s^2}$, the transient N_P is almost the same as the steady-state N_P, having a value of 8.6 and 6.6 for $FBT-07$ and $FBT-10$ respectively. However, with the rise of the acceleration rate, an initial spike happens in N_P for both impellers, followed by a decline in the state-state N_P as the transient phase ends. For example, when the acceleration rate is $12.57\ \frac{rad}{s^2}$, the transient N_P for the $FBT-07$ reaches 9.5 and then decreases to 8.6 as the transient stage fades. On the other hand, when the acceleration rate is $62.83\ \frac{rad}{s^2}$, the transient N_P spikes over 12 shortly before the shaft rotational velocity reaches ω_2. The same trend can also be seen for $FBT-10$. There are several reasons why the transient hydrodynamic N_P is higher than the steady-state condition. One key factor is the higher turbulence of the fluid near the impeller due to acceleration (deceleration would have a similar effect).

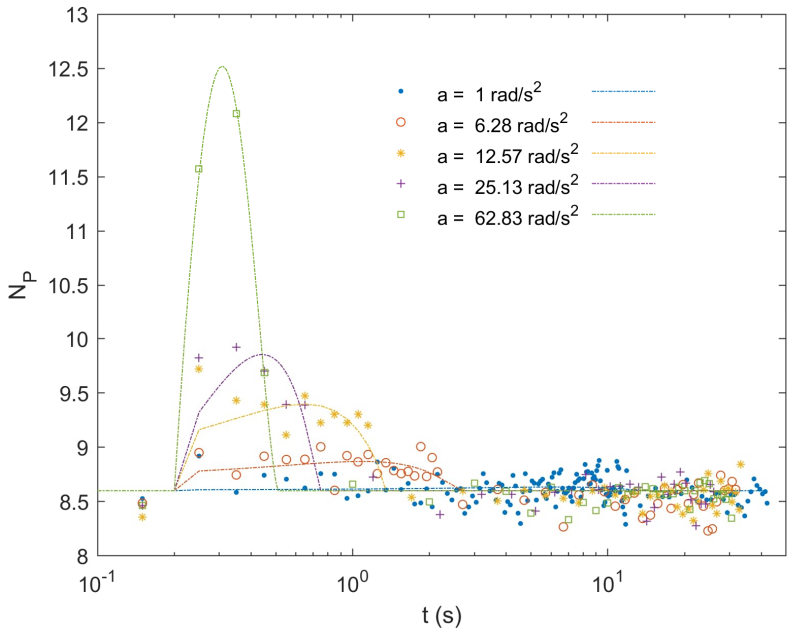

Figure 5-5: results of changing acceleration rate on N_P for $FBT-07$ ($\omega_1 = 25.13\frac{rad}{s}, \omega_2 = 37.7\frac{rad}{s}$).

It is also interesting to note that the magnitude of increase in N_P during the transient stage was higher for the $FBT-10$ impeller than FBT- 07 for all the acceleration rates. For example, when the acceleration rate was $62.83\ \frac{rad}{s^2}$, the transient N_P for $FBT-07$ increased around 45% (from 8.6 to 12.5). On the other hand, the transient N_P for $FBT-10$ increased over 85% (from 6.6 to 12.3) compared to the steady-state N_P. With almost the same Re at ω_1, these results indicate that the impeller with higher impeller diameter ($FBT-10$) operating at lower initial speed ω_1 experiences a higher level of drag forces during acceleration compared to the impeller with smaller impeller diameter ($FBT-07$) which rotates at higher ω_1.

Considering the heat generator operation in intermittent wind conditions, one can find that the abrupt increment of N_P as the shaft tends to accelerate with high acceleration rates generates high resistive hydrodynamic forces, which might prevent the system from matching itself to the

increasing wind input power. As a result, the system might not reach the optimum rotational velocity corresponding to the $C_{P,max}$, leading to a lower system efficiency.

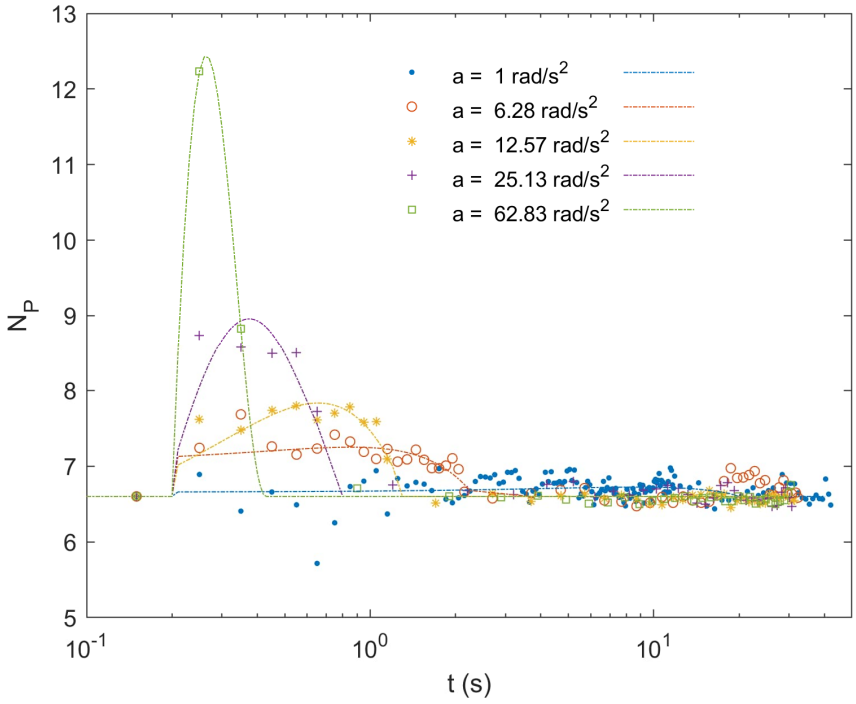

Figure 5-6: results of changing acceleration rate on N_P for $FBT-10$ ($\omega_1 = 12.57\ \frac{rad}{s}, \omega_2 = 25.13\ \frac{rad}{s}$).

5.4.1.2 Effect of different ω_1 on torque (τ) and power number (N_P) under constant acceleration rate

Figures 5-7 to 5-10 show the results of torque (τ) and power number (N_P) with different initial rotational speeds (ω_1) while keeping the acceleration rate (a) constant at $12.57\ \frac{rad}{s^2}$ to reach a target final speed (ω_2). The test conditions are provided in Table 5-4.

Figures 5-7 and 5-8 show that increasing ω_1 resulted in higher initial steady-state torque in all cases, as expected. In addition, the final torque is the same for all cases for each impeller since the

ω_2 was fixed. Higher ω_1 resulted in steeper increments of torque or, in other words, shorter duration of the transient stage in all the cases for both impellers.

Table 5-4: test conditions for transient operation with different ω_1.

Impeller	$\boldsymbol{\omega_1}$ $(\frac{\boldsymbol{rad}}{\boldsymbol{s}})$	$\boldsymbol{Re_1}$	$\boldsymbol{\omega_2}$ $(\frac{\boldsymbol{rad}}{\boldsymbol{s}})$	$\boldsymbol{Re_2}$	$\frac{\boldsymbol{d\omega}}{\boldsymbol{dt}}$ $(\frac{\boldsymbol{rad}}{\boldsymbol{s^2}})$
FBT-07	$18.85 - 43.98$	$14671 - 34231$	50.27	39521	12.57
FBT-10	$12.57 - 37.77$	$19960 - 59880$	43.98	69860	12.57

Reviewing the results of N_P presented in Figures 5-9 and 5-10, the spike in N_P at the start of the acceleration decreases as ω_1 increases for all the cases (both impellers). For $FBT-07$, when the ω_1 was $18.85\ \frac{rad}{s}$, the N_P increased to around 9.5 then started to decline to the steady-state N_P of 8.6 as the impeller rotational velocity reached to the ω_2 of $50.27\ \frac{rad}{s}$. On the other hand, the N_P spiked to around 9 at the start of the acceleration process when the ω_1 was set to $43.98\ \frac{rad}{s}$. The same trend can also be seen for the $FBT-10$. For example, the N_P went up to around 7.9 when the ω_1 was $12.57\ \frac{rad}{s}$, while as the ω_1 increased to $37.77\ \frac{rad}{s}$, the N_P slightly increased to 6.8 at the start of the transient process. These results show the dominant impact of ω_1 on changes in N_P when the acceleration rate is constant.

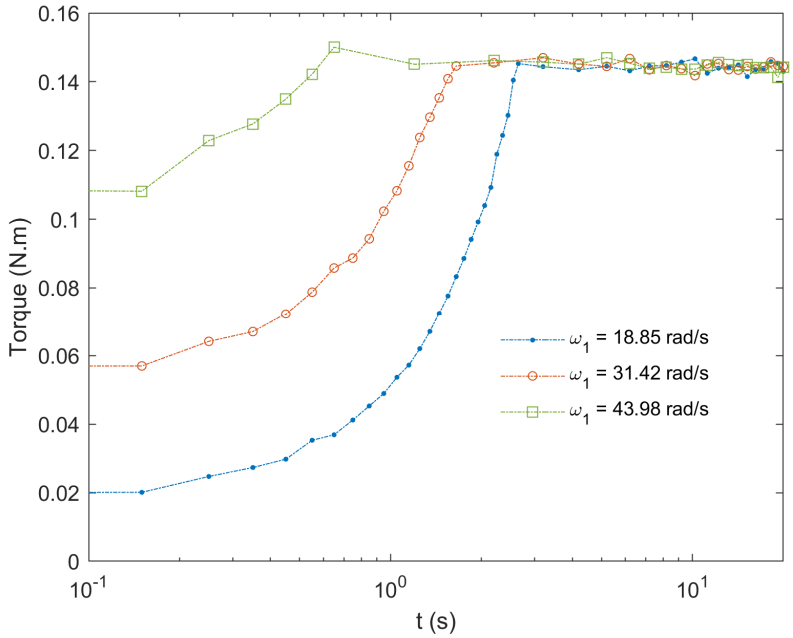

Figure 5-7: results of changing ω_1 on torque for $FBT-07$ in constant acceleration ($\omega_2 = 50.27\ \frac{rad}{s}, \frac{d\omega}{dt} = 12.57\ \frac{rad}{s^2}$).

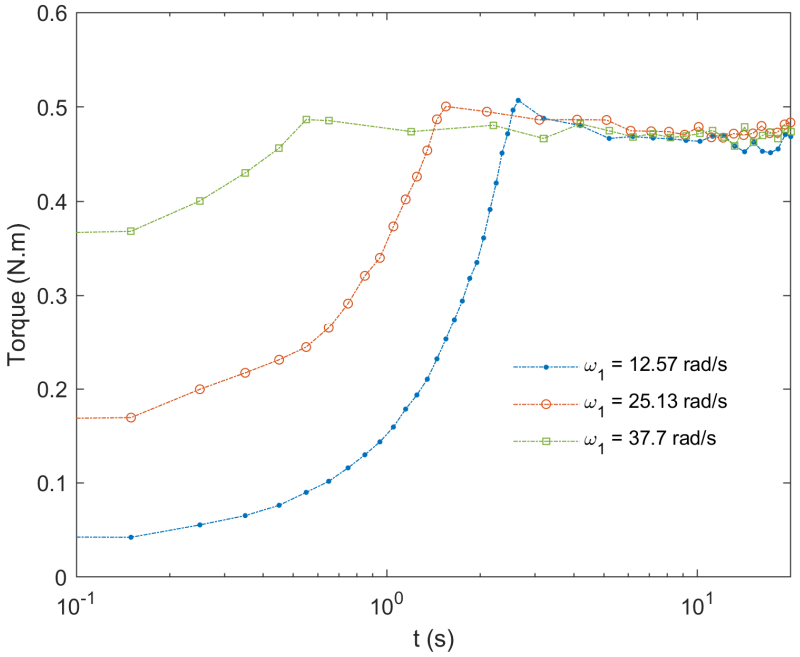

Figure 5-8: results of changing ω_1 on torque for $FBT-10$ in constant acceleration ($\omega_2 = 43.98\ \frac{rad}{s}, \frac{d\omega}{dt} = 12.57\ \frac{rad}{s^2}$).

Concerning heat generator design for WTES, these results suggest that a wind turbine-fluid agitator system that operates at lower ω_1 before the start of the acceleration process needs to overcome a higher level of hydrodynamic resistive forces to reach a potential ω_2 at constant acceleration rate compared to a system that rotates at higher initial ω_1. Therefore, it can be concluded that a system with higher ω_1 will more easily go through the acceleration process and adapt itself to the increasing wind velocity. This outcome is in line with the results of section 5.4.1.1, which demonstrated better adaptability of the system that operates at higher ω_1 to the higher acceleration rates.

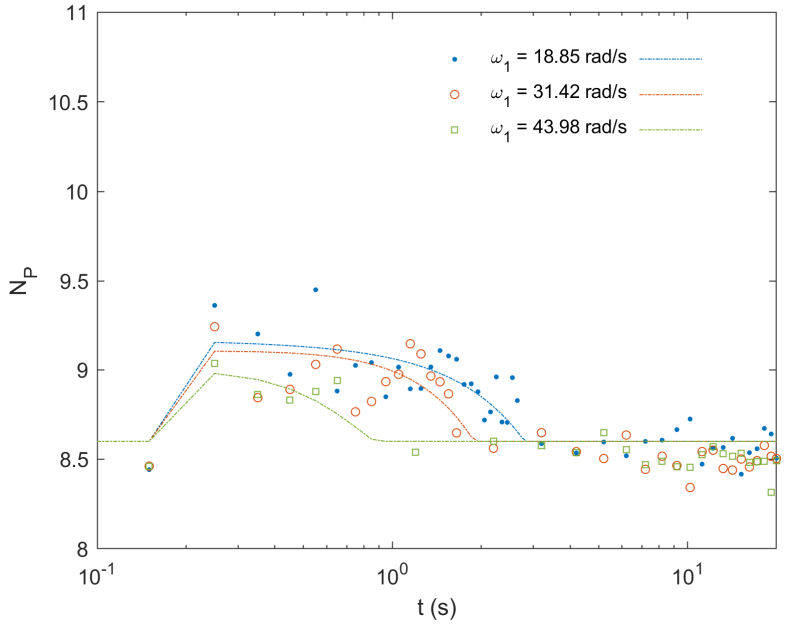

Figure 5-9: results of changing ω_1 on N_P for $FBT-07$ in constant acceleration ($\omega_2 = 50.27\ \frac{rad}{s}, \frac{d\omega}{dt} = 12.57\ \frac{rad}{s^2}$).

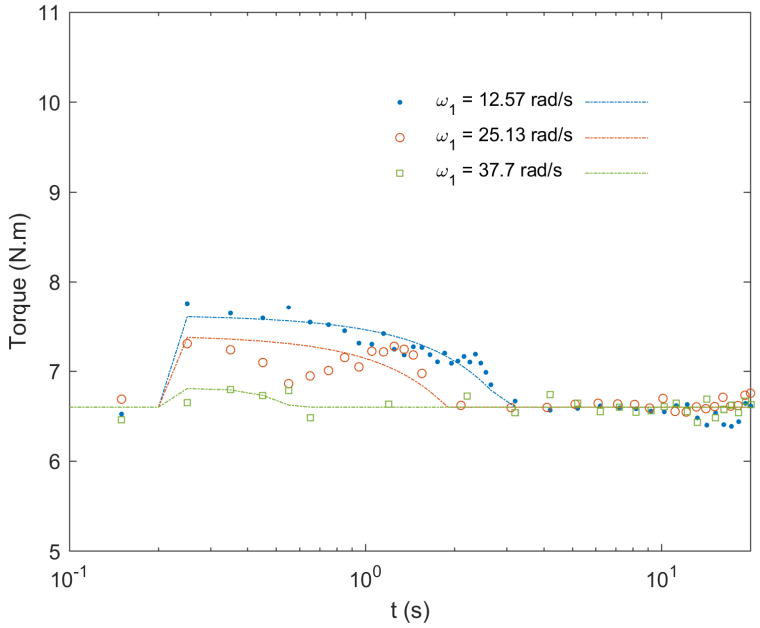

Figure 5-10: results of changing ω_1 on N_P for $FBT-10$ in constant acceleration ($\omega_2 = 43.98\ \frac{rad}{s}, \frac{d\omega}{dt} = 12.57\ \frac{rad}{s^2}$).

5.4.1.3 Effect of different ω_2 on torque (τ) and power number (N_P) under constant acceleration rate

Figures 5-11 and 5-12 depict the effect of different ω_2 on the hydrodynamic torque of the $FBT-07$ and $FBT-10$ with a constant acceleration rate of $12.57\ \frac{rad}{s^2}$ respectively. Table 5-5 also presents the range of different parameters for the experiment.

As ω_2 increases, the generated torque increases with a second order of ω for both impellers, which agrees well with the literature (equation 3). The duration of the transient operation also increases as ω_2 increases if the ω_1 is kept constant.

Table 5-5: test conditions for transient operation with different ω_2.

Impeller	ω_1 $(\frac{rad}{s})$	Re_1	ω_2 $(\frac{rad}{s})$	Re_2	$\frac{d\omega}{dt}$ $(\frac{rad}{s^2})$
FBT-07	18.85	14671	25.13 – 50.27	19560 – 39521	12.57
FBT-10	12.57	19960	18.85 – 43.98	29940 – 69860	12.57

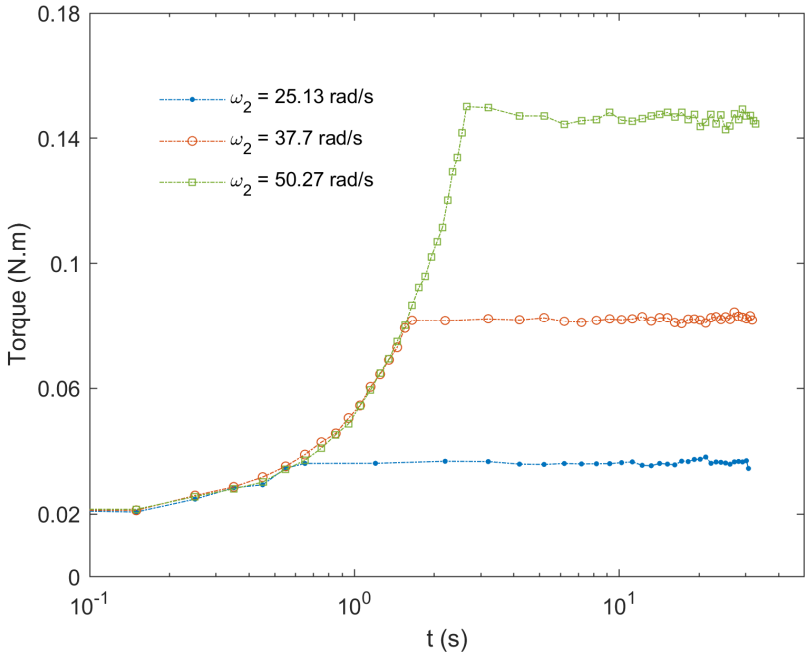

Figure 5-11: results of changing ω_2 on torque for $FBT-07$ in constant acceleration ($\omega_1 = 18.85\ \frac{rad}{s}, \frac{d\omega}{dt} = 12.57\ \frac{rad}{s^2}$).

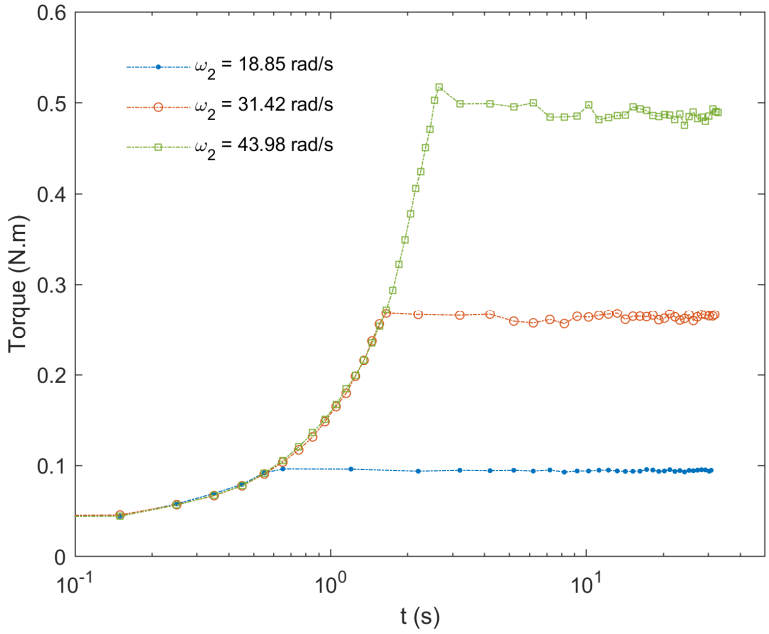

Figure 5-12: results of changing ω_2 on torque for $FBT-10$ in constant acceleration ($\omega_1 = 12.57\ \frac{rad}{s}, \frac{d\omega}{dt} = 12.57\ \frac{rad}{s^2}$).

Figures 5-13 and 5-14 depict the results of changing ω_2 on N_P while the acceleration rate is kept constant at $12.57\frac{rad}{s^2}$ for $FBT-07$ and $FBT-10$ respectively. The transient N_P for all the tests (both impellers) follows the same trend, with immediate spikes as the transient operation starts, then reducing back to its steady-state values as the transient state ends. It is also interesting to note that the maximum value of N_P was nearly the same for all tests (each impeller) regardless of ω_2. This is a remarkable finding since it shows that the transient N_P for the impeller is directly linked to the acceleration rate and independent of ω_2 or, in other words, the duration of the transient operation. Moreover, it was seen in section **b** that the change in N_P is smaller for higher ω_1 when the acceleration rate is constant. By combining these results, and also based on the steady-state design criteria for wind turbine-heat generator matching, $N_P D^5$, it can be concluded that a heat generator higher steady-state N_P operating at reasonably high initial speed ω_1 might respond better

to the acceleration due to the lower impact of transient hydrodynamic resistive forces. This will lead to a better matching of the system rotation velocity (ω that corresponds to the $C_{P,max}$) to the increasing wind speeds, resulting in higher system efficiency.

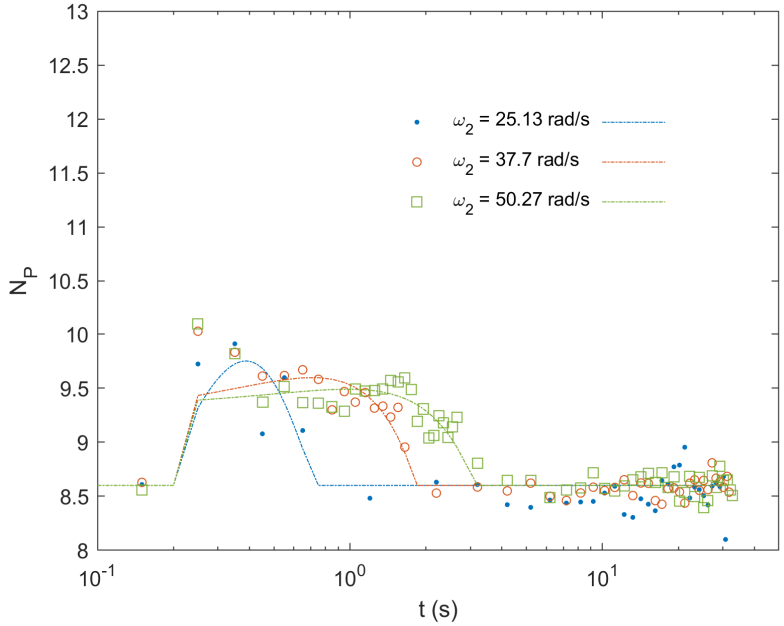

Figure 5-13: results of changing ω_2 on N_P for $FBT-07$ in constant acceleration ($\omega_1 = 18.85\frac{rad}{s}, \frac{d\omega}{dt} = 12.57\frac{rad}{s^2}$).

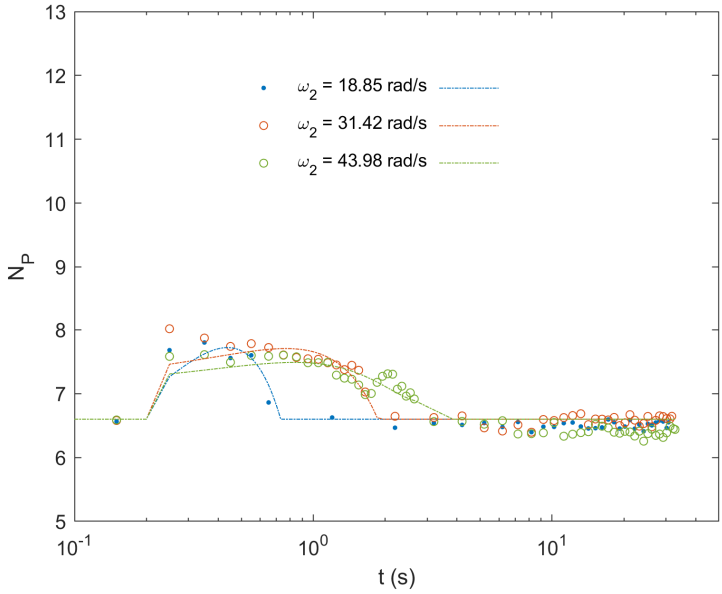

Figure 5-14: results of changing ω_2 on N_P for $FBT-10$ in constant acceleration ($\omega_1 = 12.57\frac{rad}{s}, \frac{d\omega}{dt} = 12.57\frac{rad}{s^2}$).

5.4.2 Deceleration

This section investigates the effect of impeller deceleration rate (linear decrease of angular speed) on transient torque and N_P. The experiments were designed in the same manner as the acceleration experiments, thereby allowing for a comparison of the outcomes.

5.4.2.1 Effect of different deceleration rate on transient torque (τ) and N_P

Figures 5-15 and 5-16 show the result of different deceleration rates of -1, -6.28, -12.57, -25.13, and $-62.83\ \frac{rad}{s^2}$ on the impeller's torque for $FBT-07$ and $FBT-10$. The other parameters for the experiments are shown in Table 5-6.

Table 5-6: test conditions for transient operation with different deceleration rates.

Impeller	$\omega_1\ (\frac{rad}{s})$	$\omega_2\ (\frac{rad}{s})$	$-\frac{d\omega}{dt}\ (\frac{rad}{s^2})$
FBT-07	37.7	25.13	1 – 62.83
FBT-10	37.7	25.13	1 – 62.83

When ω_1 was constant at $37.7\ \frac{rad}{s}$, the steady-state torque was 0.084 and $0.37\ N.m$ for $FBT-07$ and $FBT-10$ respectively. As the ω_1 decreased to $25.13\ \frac{rad}{s}$, the torque also reduced to 0.04 and $0.18\ N.m$ for $FBT-07$ and $FBT-10$ respectively. The higher deceleration rate led to a shorter transient period, resulting in a steeper slope of the torque decrement for both impellers.

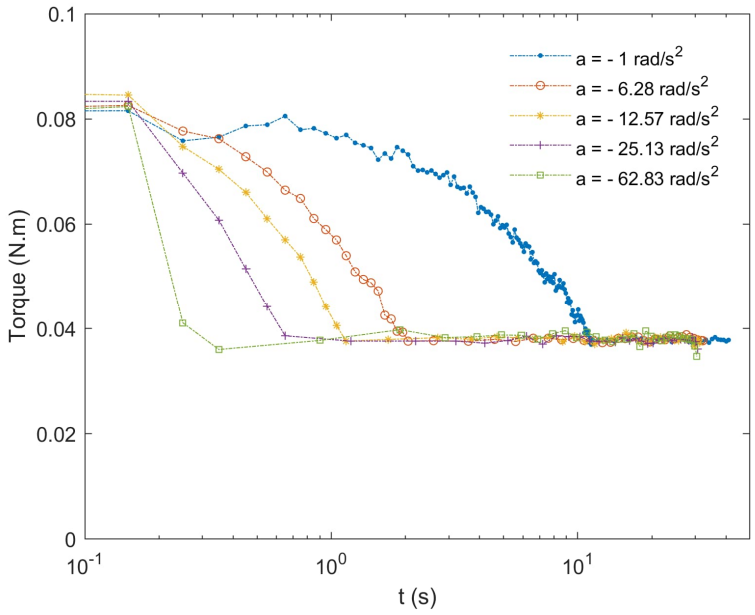

Figure 5-15: results of changing deceleration rate on torque for $FBT-07$ ($\omega_1 = 37.7\ \frac{rad}{s}$, $\omega_2 = 25.13\ \frac{rad}{s}$).

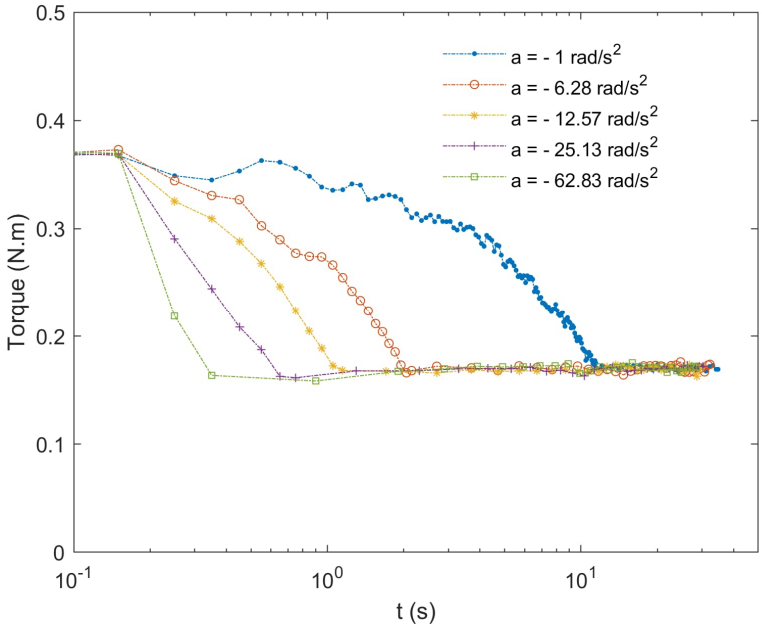

Figure 5-16: results of changing deceleration rate on torque for $FBT-10$ ($\omega_1 = 37.7\ \frac{rad}{s}$, $\omega_2 = 25.13\ \frac{rad}{s}$).

The variation of N_P for $FBT-07$ and $FBT-10$ over the experiment period is shown in Figures 5-17 and 5-18, respectively. The low deceleration rate of $-1\frac{rad}{s^2}$ had minimum impact on the N_P with an almost steady flow field for both impellers. Higher deceleration rates resulted in a more significant decrease of N_P. From all the tests, the N_P tends to decrease as the deceleration process starts, then returns to the steady-state condition after reaching a minimum value.

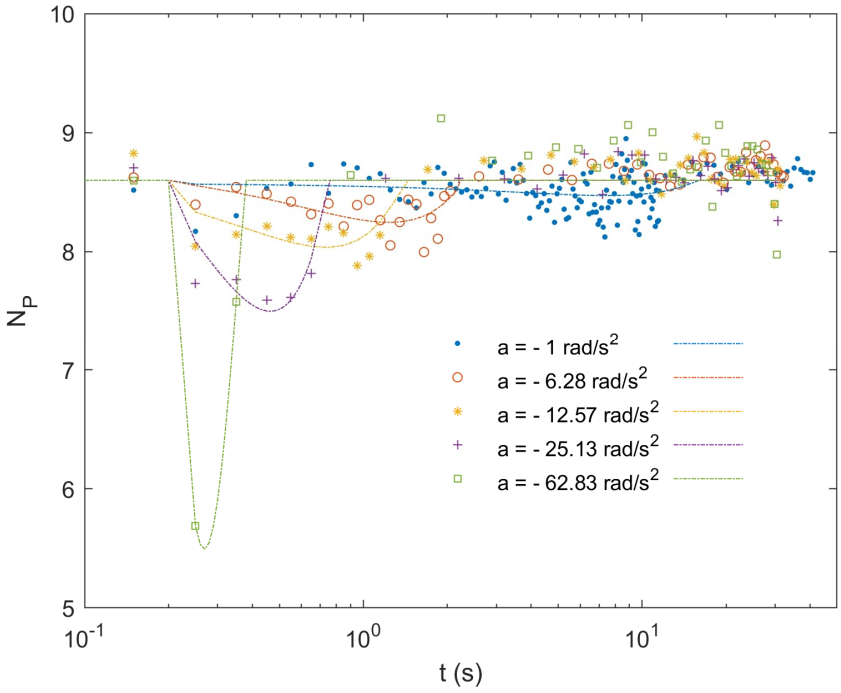

Figure 5-17: results of changing deceleration rate on N_P for $FBT-07$ ($\omega_1 = 37.7\ \frac{rad}{s}$, $\omega_2 = 25.13\,r\frac{rad}{s}$).

By comparing the results of acceleration tests (section 5.4.1.1) to the results obtained from the deceleration experiments, it can be understood that the magnitude of the N_P variation during deceleration is lower than acceleration for both impellers. For example, the minimum N_P of 5.5 for the $FBT-07$ resulted from a deceleration rate of $-62.83\ \frac{rad}{s^2}$, which is a reduction of about 36% compared to the steady state N_P of 8.6. On the other hand, the maximum N_P for $FBT-07$ was 12.5 ($\frac{d\omega}{dt} = 62.83\ \frac{rad}{s^2}$), which is 45% higher than the steady state N_P of 8.6. This difference could result from the acceleration process's higher impact on the flow field. It is evident that the acceleration process produces turbulence in the flow field (due to the increasing shaft speed), resulting in a spike in N_P. However, the higher initial level of turbulence of the flow field (higher

initial ω_1) in the deceleration process dominates the impact of lowering angular speed, leading to the lower reduction in N_P in the deceleration phase.

Another exciting finding comparing the deceleration results to the acceleration experiments is that the minimum N_P resulted from changing the deceleration rate almost occurred near the end of the transient period. In contrast, the N_P peaked to its maximum value right at the start of the transient process for different acceleration rates. This could also be explained by the fact that the flow field immediately responds to the increase in turbulence level because of acceleration, while it catches up more slowly to the decreasing turbulence resulting from the deceleration process, which in turn shifts the minimum of N_P toward the ends of the process.

In the case of heat generator design for WTES, the experimental results suggest that the reduction of N_P during the deceleration process will not negatively impact the system's ability to respond to

a declining wind velocity. The system's lower N_P compared to the steady-state condition could facilitate a faster response to declining wind speeds.

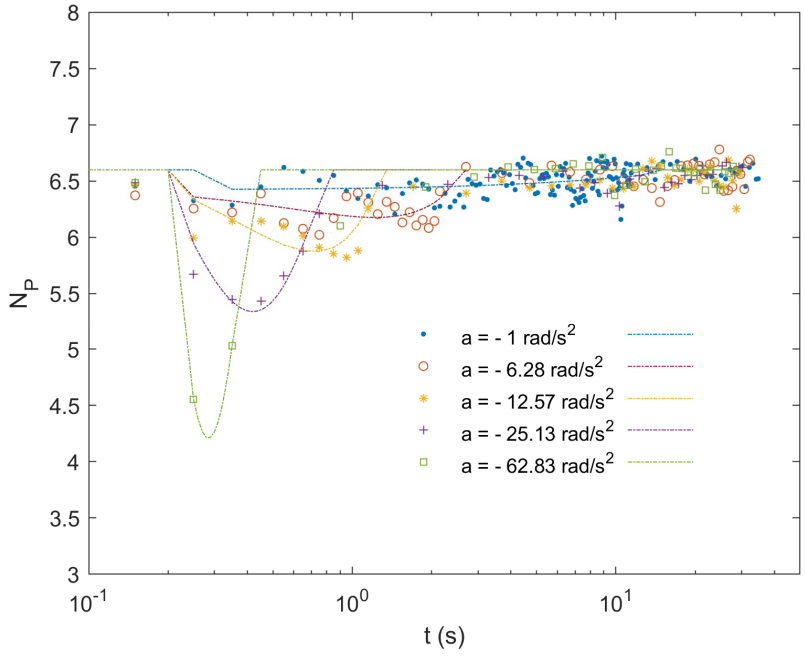

.

Figure 5-18: results of changing deceleration rate on N_P for $FBT-10$ ($\omega_1 = 37.7\ \frac{rad}{s}$, $\omega_2 = 25.13\ \frac{rad}{s}$).

5.4.2.2 Effect of different ω_1 on torque (τ) and power number (N_P) with constant deceleration rate

The effects of different ω_1 on torque are shown in Figures 5-19 to 5-20, and the effects on N_P are shown in Figures 5-21 and 5-22, for impellers $FBT-07$ and $FBT-10$ respectively. In these tests, the deceleration rate is kept constant at $-12.57\ \frac{rad}{s^2}$, and the same target ω_2 is used for each impeller. The other test conditions are provided in Table 9.

Table 5-7: test conditions for transient operation with different ω_1.

Impeller	ω_1 $(\frac{rad}{s})$	Re_1	ω_2 $(\frac{rad}{s})$	Re_2	$\frac{d\omega}{dt}$ $(\frac{rad}{s^2})$
FBT-07	25.13 – 50.27	19560 – 39122	18.85	39521	−12.57
FBT-10	18.85 – 43.98	29940 – 69860	12.57	69860	−12.57

At the same deceleration rate, lower ω_1 means a shorter transition period to reach the same target ω_2. The final torque was also the same for different tests on each impeller. Lower ω_1 also leads to lower torque throughout the deceleration period. The one with a larger diameter (FBT-10) induces more significant torque during the deceleration between the two impellers.

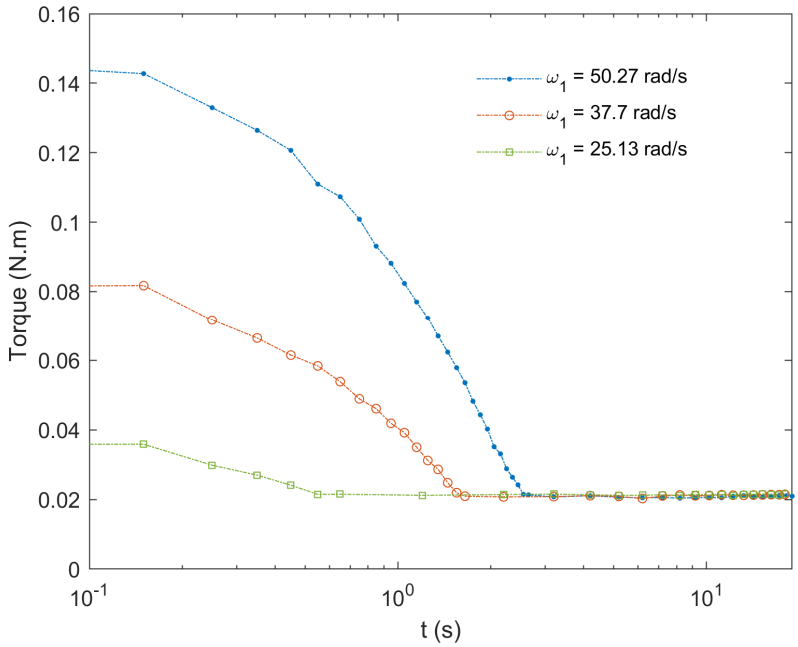

Figure 5-19: results of changing ω_1 on torque for $FBT-07$ in constant deceleration ($\omega_2 = 18.85\ \frac{rad}{s}, \frac{d\omega}{dt} = -12.57\ \frac{rad}{s^2}$).

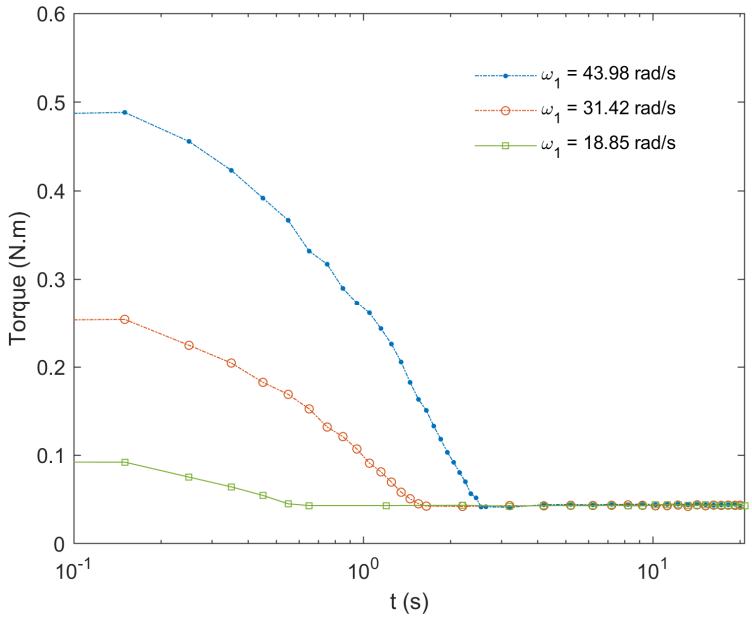

Figure 5-20: results of changing ω_1 on torque for $FBT-10$ in constant deceleration ($\omega_2 = 12.57\ \frac{rad}{s}, \frac{d\omega}{dt} = -12.57\ \frac{rad}{s^2}$).

Figures 5-21 and 5-22 show the power numbers N_P in these tests. As the deceleration starts, N_P first decreases and reaches a minimum, then increases back to its steady-state level when the target ω_2 is reached for each impeller. Higher ω_1 at the initial steady-state stage resulted in lower minimum N_P during deceleration. In addition, with higher ω_1, the minimum N_P happened closer to the end of the transient stage. This can be explained in a similar way as for the acceleration tests. The higher turbulence level of the flow field dominates the effects of shaft angular velocity reduction, resulting in slower responses of the flow field to the deceleration process. As discussed earlier, this slower response of the system to the deceleration process in higher ω_1 could facilitate the heat generator to adapt its angular velocity smoothly to a declining wind speed in real-world conditions.

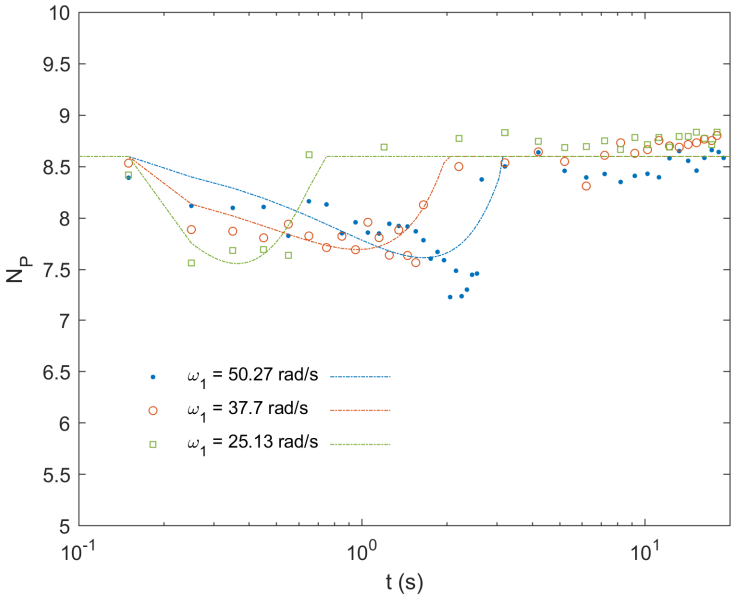

Figure 5-21: results of changing ω_1 on N_P for $FBT-07$ in constant deceleration ($\omega_2 = 18.85\ \frac{rad}{s}, \frac{d\omega}{dt} = -12.57\ \frac{rad}{s^2}$).

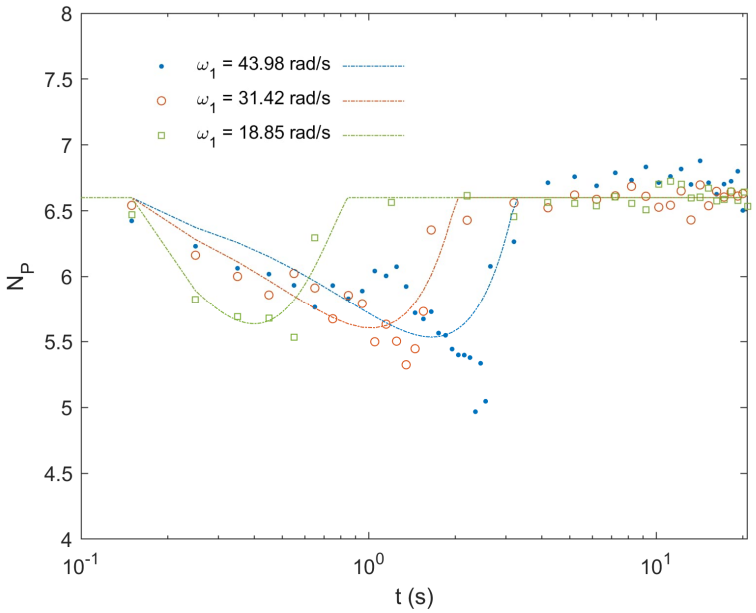

Figure 5-22: results of changing ω_1 on N_P for $FBT-10$ in constant deceleration ($\omega_2 = 12.57\ \frac{rad}{s}, \frac{d\omega}{dt} = -12.57\ \frac{rad}{s^2}$).

5.4.2.3 Effect of different final speed ω_2 on torque (τ) and power number (N_P) with constant deceleration rate

The effects of changing ω_2 on torque (τ) and power number (N_P) are shown in Figures 5-23 to 5-26 for $FBT-07$ and $FBT-10$, respectively. Table 5-8 also presents the range of parameters for the tests. As expected, decreasing ω_2 led to a reduction of the torque with the second order of ω for all the tests (both impellers). Moreover, the power number N_P follows the trend seen in the previous section, starting to decrease as the transient process begins and then increasing to its steady-state value after passing a minimum near the end of the transient stage.

Table 5-8: test conditions for deceleration with different ω_2.

Impeller	$\omega_1\ (\frac{rad}{s})$	Re_1	$\omega_2\ (\frac{rad}{s})$	Re_2	$\frac{d\omega}{dt}\ (\frac{rad}{s^2})$
FBT-07	50.27	39121	18.85 – 43.98	14670 – 34231	−12.57
FBT-10	43.98	69680	12.57 – 37.7	19960 – 59880	−12.57

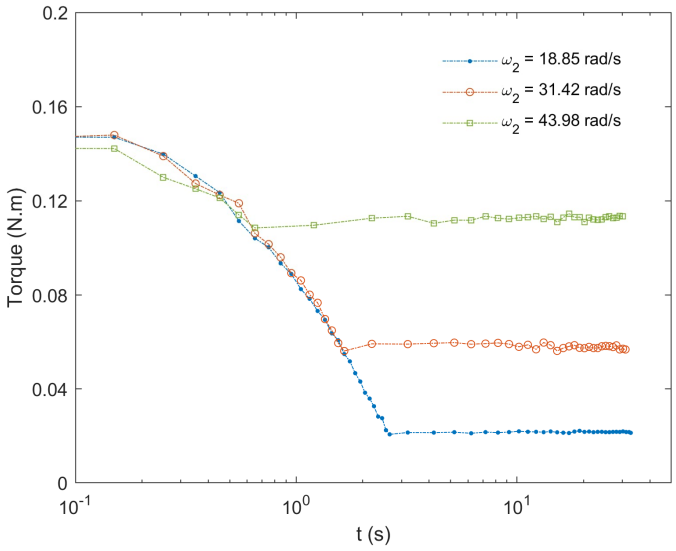

Figure 5-23: results of changing ω_2 on torque for $FBT-07$ in constant deceleration ($\omega_1 = 50.27\ \frac{rad}{s}, \frac{d\omega}{dt} = -12.57\ \frac{rad}{s^2}$).

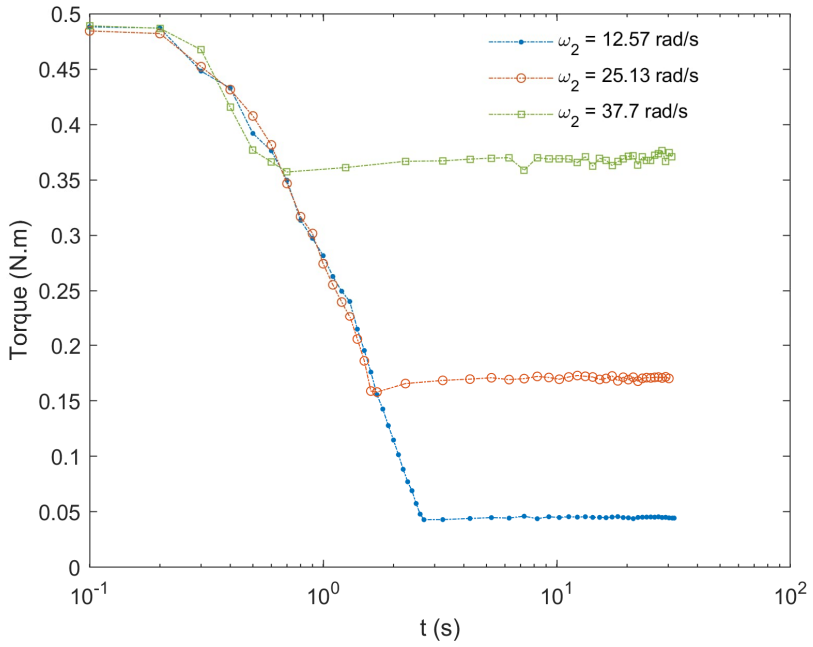

Figure 5-24: results of changing ω_2 on torque for $FBT-10$ in constant deceleration ($\omega_1 = 43.98\ \frac{rad}{s}, \frac{d\omega}{dt} = -12.57\ \frac{rad}{s^2}$).

With the same deceleration rate, different ω_2 resulted in approximately the same minimum N_P for each impeller. In Figure 30, a constant deceleration rate of $-12.57\frac{rad}{s^2}$ resulted in nearly identical minimum N_P of 8 for $FBT-07$ when ω_2 changed from 18.85 to $43.98\ \frac{rad}{s}$. Similarly, approximately the same minimum N_P of 5.7 was achieved for $FBT-10$ as ω_2 varied from 12.57 to $37.7\ \frac{rad}{s}$. This is similar to what was seen in the acceleration process, meaning that the effect of the deceleration rate on the N_P is dominant. For both impellers, the minimum N_P is achieved almost near the end of the transient stage. As discussed in the previous sections, this denotes the dominant effect of the flow field's initial turbulence level.

The results of hydrodynamic torque and power number presented for the deceleration tests suggest that the deceleration process does not prevent the system from matching its rotational velocity with the declining wind speeds since the power number during the deceleration process is lower than the power number during the steady-state condition. However, as the power number decreases, the system's performance in terms of heat generation will also decrease due to less resistive torque of the agitator. Therefore, limiting the reduction in power number seems to be beneficial for the system's performance during the deceleration process.

Combining the results obtained from the acceleration tests and deceleration experiments, it can be concluded that although addressing the spike of N_P because of acceleration is critical for the successful operation of the wind-agitator system, finding an operating range of ω for the wind turbine-agitator system based on the actual wind profile could be beneficial for optimizing system operation, especially under gusty wind conditions.

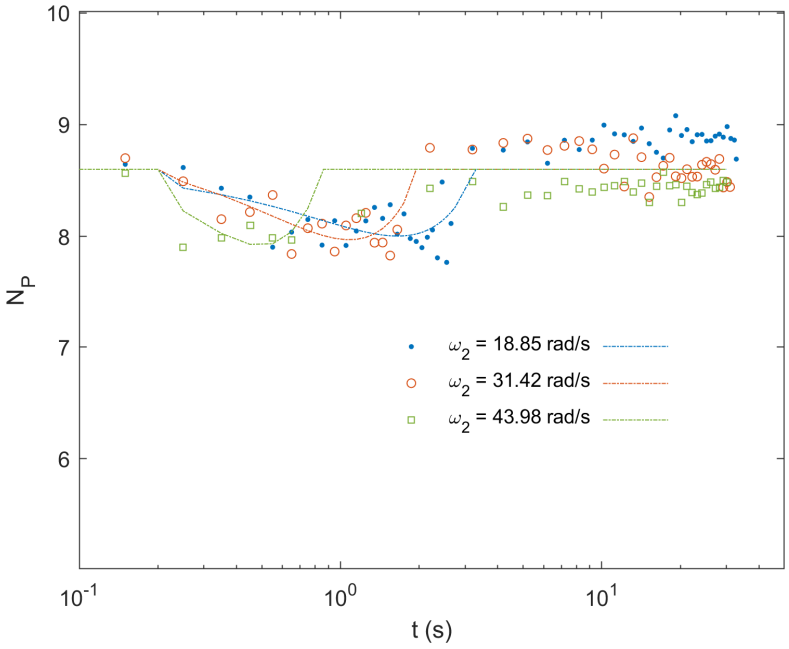

Figure 5-25: results of changing ω_2 on N_P for $FBT-07$ in constant deceleration ($\omega_1 = 50.27\ \frac{rad}{s}, \frac{d\omega}{dt} = -12.57\ \frac{rad}{s^2}$).

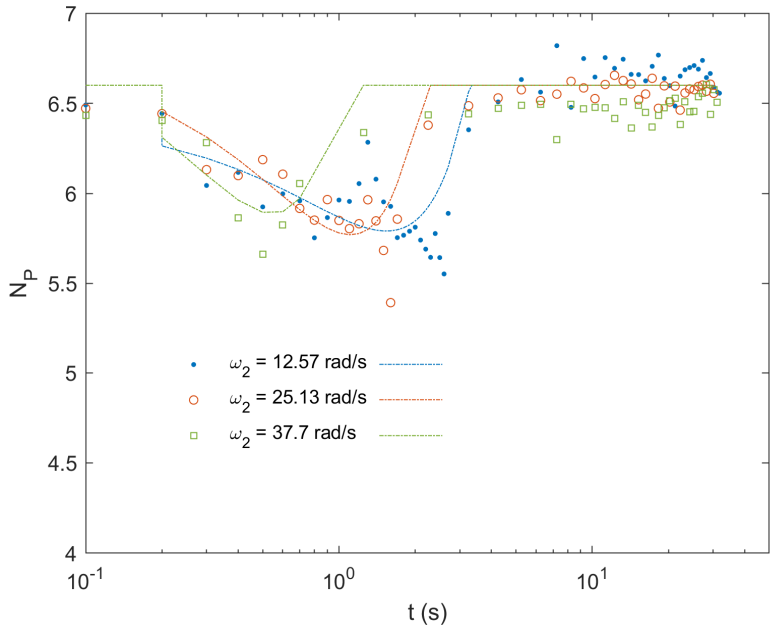

Figure 5-26: results of changing ω_2 on N_P for $FBT-10$ in constant deceleration ($\omega_1 = 43.98\ \frac{rad}{s}, \frac{d\omega}{dt} = -12.57\frac{rad}{s^2}$).

5.4.3 Sinusoidal velocity profile

This section aims to evaluate the effect of changing shaft angular velocity under a sinusoidal profile on torque, and N_P for $FBT-10$. As it is reported, wind speed can be modeled as the sum of several given sinusoidal components [108]. Therefore, a sinusoidal function is considered to roughly simulate a transient wind profile to gain a better insight into the agitator's operation under transient conditions.

The hypothetical velocity profile based on a sinusoidal wave is as follows:

$$\omega_{\infty} = \omega_0 + \omega_A Sin(2\pi f t) \quad (5.1)$$

Where ω_0 is the offset angular velocity and ω_A is the velocity amplitude. In addition, f is the angular frequency of the shaft velocity, defined as $\frac{1}{T}$ (T is the period to complete one cycle in seconds).

5.4.3.1 Effect of different shaft angular frequency (f) on torque (τ) and power number (N_P)

Figures 5-27 and 5-28 show the effect of different shaft angular frequencies ($T = 1, 5, 10\ s$) on the torque (τ) and power number (N_P) for impeller $FBT-10$. The range of test's parameters are also tabulated in Table 5-9.

Table 5-9: range of parameters for sine velocity profile experiments with different frequencies.

Impeller	$\boldsymbol{\omega_0\ (\frac{rad}{s})}$	$\boldsymbol{\omega_A\ (\frac{rad}{s})}$	$\boldsymbol{f\ (Hz)}$
FBT-10	31.42	12.57	0.1, 0.2, 1

Figure 5-27 shows that the steady-state torque for the offset velocity (ω_0) of $31.42\ \frac{rad}{s}$ is $0.28\ N.m$ which is similar for all the tests. Moreover, the maximum and minimum torque (0.53 and $0.9\ N.m$) are the same regardless of angular frequency variation. Increasing the shaft angular frequency (lower T in the figures) resulted in a higher number of cycles that the impeller underwent. A higher frequency is associated with a higher variation of the shaft angular velocity (higher acceleration/ deceleration rates). Since the torque and velocity are in the same phase, increasing the frequency led to sharper changes in torque values. Finally, it is evident that a higher frequency of angular velocity will result in higher power conversion and, therefore, higher heat generation.

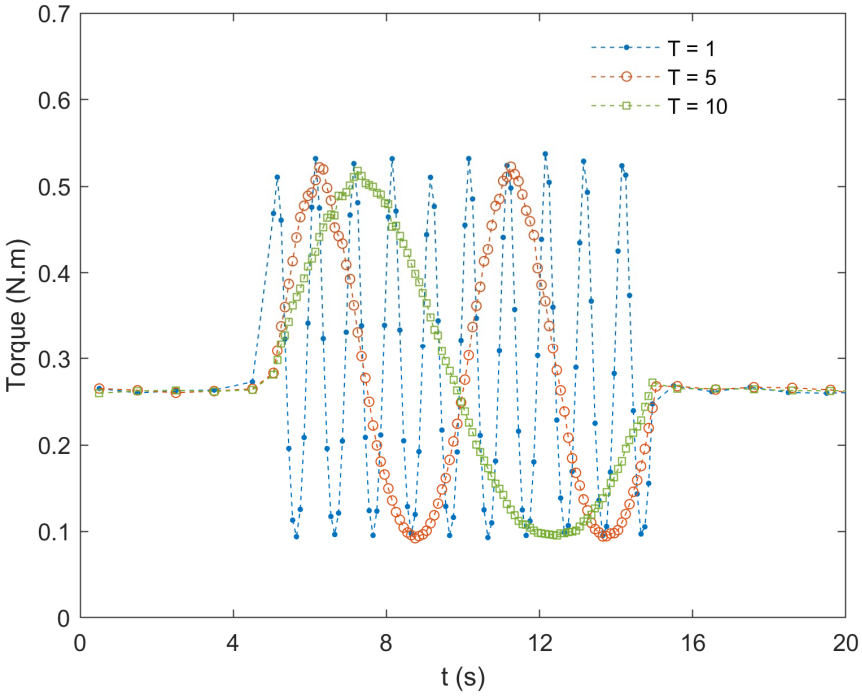

Figure 5-27: results of changing shaft angular frequency on torque for $FBT-10$ ($\omega_0 = 31.42\ \frac{rad}{s}, \omega_A = 12.57\ \frac{rad}{s}$).

The effects of shaft angular frequency variation on power number are presented in Figure 5-28. Note that the shaft angular frequencies of 0.1, 0.2, and $1\ Hz$ corresponds to the maximum or

minimum acceleration or deceleration rate of ± 7.89, ± 15.79, and $\pm 78.94 \frac{rad}{s^2}$, respectively. As the shaft angular frequency increases, the change in N_P also increases. For example, when the shaft angular frequency was set to $0.1\,Hz$, the maximum and minimum N_P were 7.1 and 6, respectively, which are slightly different from the steady state N_P of 6.6. On the other hand, the maximum and minimum N_P for the shaft angular frequency of $1\,Hz$ were 10.3 and 3.9, respectively, which shows a considerable deviation from the steady state N_P. These results are in line with the results obtained from the acceleration and deceleration experiments in which higher acceleration/deceleration rates resulted in abrupt changes in N_P.

An interesting observation from Figure 5-28 is that the maximum N_P at the impeller rotation's first cycle was lower than the overall maximum N_P for all three shaft angular frequencies. For example, at shaft angular frequency of $1\,Hz$, the N_P surged to a value of 8.4 at the first cycle while it rose to a value of around 10.4 at the subsequent cycles. The reason for this difference could result from the continuous oscillation of the impeller's angular speed, which produced a higher level of turbulence after the first cycle.

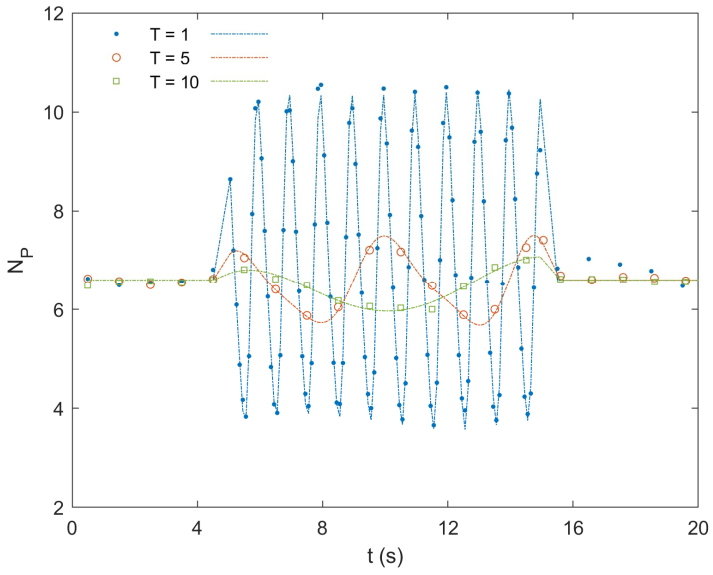

Figure 5-28: results of changing shaft angular frequency on N_P for $FBT-10$ ($\omega_0 = 31.42\ \frac{rad}{s}, \omega_A = 12.57\ \frac{rad}{s}$).

5.4.3.2 Effect of different shaft angular amplitude on torque (τ) and power number (N_P)

The effect of varying the amplitude of the sinusoidal velocity profile on the torque (τ) and power number (N_P) is shown in Figures 5-29 and 5-30. Moreover, Table 5-10 presents the range of parameters of the test. Changing the velocity amplitude leads to a variation of the acceleration/deceleration rates of the cycle. The acceleration/ deceleration rates corresponding to the velocity amplitudes of 3.14, 6.28, and $12.57\ \frac{rad}{s}$ are 19.72, 39.44, and $78.94\ \frac{rad}{s^2}$ respectively.

Table 5-10: range of parameters for sine velocity profile experiments with different amplitudes.

Impeller	$\boldsymbol{\omega_0\ (\frac{rad}{s})}$	$\boldsymbol{\omega_A\ (\frac{rad}{s})}$	$\boldsymbol{f\ (Hz)}$
FBT-10	31.42	3.14, 6.28, 12.57	1

As can be seen in Figure 5-29, increasing the amplitude of the sine velocity profile resulted in increasing the peak torque of the cycle in the transient process. When the amplitude was set to $3.14\ \frac{rad}{s}$, the torque oscillated between 2.3 to $3.2\ N.m$. However, increasing the amplitude to $12.57\ \frac{rad}{s}$ resulted in a variation of torque between 0.09 to $0.54\ N.m$. The effect of different amplitude on the N_P, Figure 5-30, also shows that increasing the amplitude of the sine velocity profile led to higher changes in N_P due to the velocity profile's higher acceleration/deceleration rates. This is also in line with the results obtained in 5.4.1 and 5.4.2, in which the higher acceleration/ deceleration rates resulted in a higher change in N_P. A similar observation to what was seen in the previous section can also be understood here, which is the smaller peak of the N_P at the first cycle of the rotation. This can also be regarded as the effect of high shaft angular frequency, which resulted in a more chaotic flow field and, therefore, higher N_P after the first cycle.

The sinusoidal velocity profile test results help understand the operation of wind-powered heat generators under rapid wind fluctuation (high acceleration/deceleration rate and high frequency). Although the system achieves a higher heat generation level due to higher input power, it needs to overcome higher hydrodynamic resistive forces, which can lead to operation difficulties. On the other hand, the system operation will be smoother when the wind speed changes smoothly as less resistive hydrodynamic forces will be generated in the agitator. It is worth mentioning that it is also critical to study the performance of the wind turbine under intermittent wind as a next step.

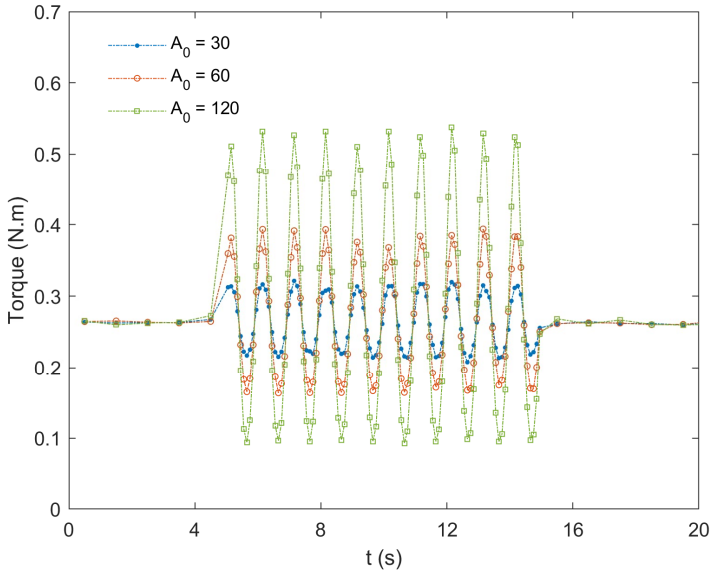

Figure 5-29: results of changing velocity amplitude on torque for $FBT-10$ (

$\omega_0 = 31.42\,\frac{rad}{s}, f = 1\,Hz$).

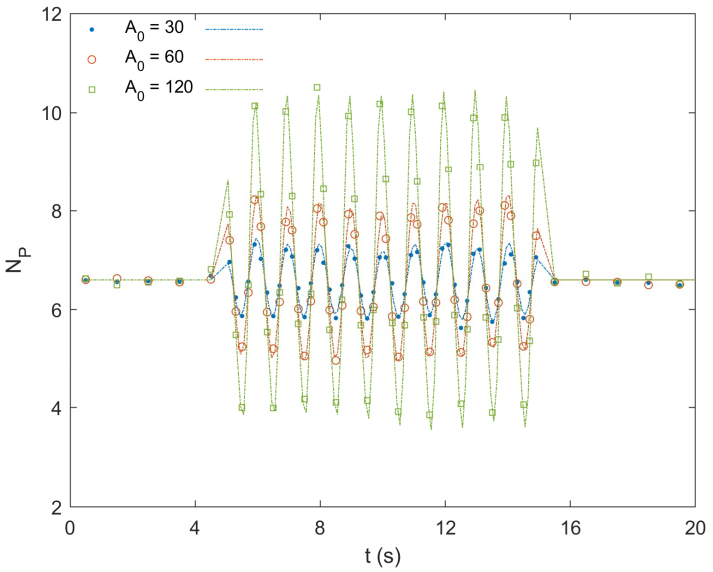

Figure 5-30: results of changing velocity amplitude on N_P for $FBT-10$ (

$\omega_0 = 31.42\,\frac{rad}{s}, f = 1\,Hz$).

5.5 Effect of different velocity profiles on temperature rise of the working fluid

A 60-minute test was conducted to quantify the effect of different velocity profiles on the rise in temperature of the working fluid (distilled water at room temperature), and the results are shown in Figure 5.23. The velocity profiles were constant angular velocity ($\omega = 31.42\ \frac{rad}{s}$) and sinusoidal velocity ($\omega_0 = 31.42\ \frac{rad}{s}$, $\omega_0 = 31.42\ \frac{rad}{s}$, $f = 1\ Hz$). In addition to ΔT, the net input power of the agitator, P_{HG}, was also calculated using the torque measurement data. It is worth noting that the vessel was carefully insulated using double reflective insulation (Reflectix ®) to ensure minimum heat loss to the surroundings.

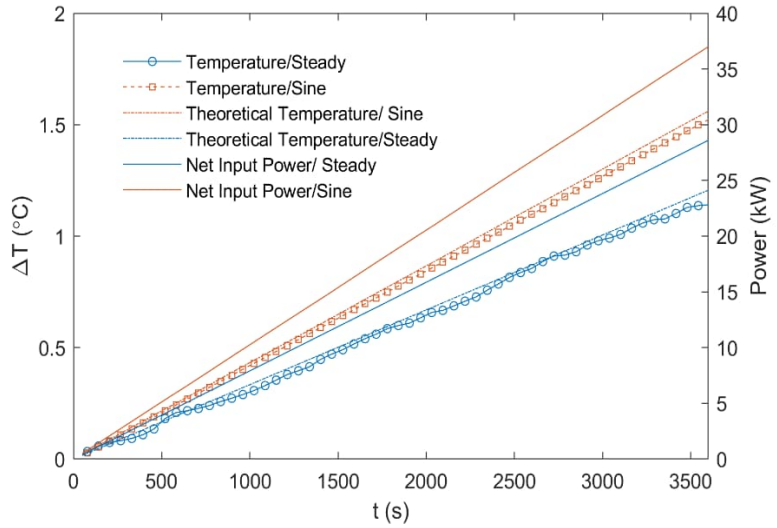

Figure 5-31: effect of different angular velocity profiles on the working fluid temperature rise for $FBT - 10$.

The rise in the temperature of the water is linear over time for both velocity profiles, which agrees with the literature [42, 52, 54, 57]. The steady motion of the shaft at $31.42\ \frac{rad}{s}$ resulted in total power absorption of 29 kW, and the fluid temperature increased around 1.1 ℃. The measured temperature rise was almost the same as the theoretical one. Here, the theoretical temperature rise

was calculated based on the agitator total power absorption, $W = P_{HG} \times t$, through torque measurement for the test duration (equation 10). On the other hand, applying a sinusoidal velocity profile based on equation 5.1 resulted in a total power absorption of 37 kW and a temperature rise of 1.6 ℃. The higher temperature rise of the fluid with the sine velocity profile was due to the shaft's higher input power absorption than the steady velocity profile since the impeller's power number (N_P) was higher under transient operation.

5.6 Summary

This chapter presents the results of the experimental analysis regarding the agitator's operation under different operating scenarios. First, the steady state results for N_P across the selected Reynolds ranges are presented. Next, the torque and N_P under different transient modes, including acceleration, deceleration, and sine velocity profile, are provided and discussed in detail. Finally, the effects of different velocity profiles, including constant angular velocity, and sinusoidal angular velocity, on the temperature rise of the working fluid are presented and analyzed.

Traditionally, the steady state N_P is used to match a heat generator to a wind turbine. However, the results obtained in this chapter show the critical impact of the transient operation on the N_P, which needs to be considered when designing a heat generator based on agitation technology for a WTEC.

It was shown that a wind turbine-agitator system can generate higher thermal energy during the gusty wind. However, the complexity associated with the changing flow field under gusty wind conditions suggests that the system operation is more guaranteed under lightly changing wind profiles. Moreover, it is seen that the effect of acceleration is more critical compared to the deceleration phenomena to be considered in the heat generator design. This is because the acceleration process can abruptly increase the resistive force in the flow field, preventing the

system from matching its angular velocity to the changing wind speeds. In this regard, designing a heat generator that operates at high angular velocities at all wind speeds could be beneficial to reduce the impact of the acceleration process on the abrupt change of the N_P. Another important finding that should be applied in designing a wind-agitator system is considering transient N_P instead of steady-state N_P in the theoretical matching process to obtain the highest efficiency, as the results showed a considerable difference between these two numbers especially under high acceleration/deceleration rates. However, unlike the readily available steady-state $N_P$values for various impeller designs, there is a notable absence of transient N_P values in the literature. This absence makes the transient analysis of the wind turbine-fluid agitator impossible. The results of the experimental analysis in this study reveal that the transient N_P for any specific impeller design can be obtained. Therefore, the wind turbine-fluid agitator system can be designed to achieve higher efficiency.

Conclusion and recommendation

6.1 Conclusion

The traditional approach to designing a heat generator for WTEC, based on fluid agitation, involves matching wind turbine torque to heat generator torque in steady-state operation (steady-state N_P). Unfortunately, this method yields poor system performance, hindering further WTEC technology development. In this study, we evaluated the transient operation of a fluid agitator for WTEC through experimental analysis. A proof-of-concept agitator heater was designed, powered by an electric motor for testing various design parameters. Transient operating modes were implemented to simulate wind speed intermittency, including acceleration, deceleration, and variable angular speed based on a sinusoidal function. A comprehensive parametric study of key design parameters, including acceleration/deceleration rate, initial velocity, and final velocity, was conducted to understand heat generator behavior under transient conditions better.

Results show that transient N_P differs from steady state N_P for each impeller design, emphasizing the importance of considering transient N_P in the heat generator design process. Examining acceleration/deceleration rates revealed their direct impact on transient N_P, with higher sensitivity to acceleration. This highlights the dominant effect of increasing turbulence and resistive forces during acceleration in the flow field. In addition, the study of initial steady-state velocity showed an inverse impact on N_P variation. In contrast, the final angular velocity had minimal effect on N_P variation when acceleration/deceleration rates were constant. This suggests the benefits of designing the rotor shaft to operate at higher angular velocities with appropriate transmission gear ratios. Furthermore, variable shaft angular motion based on a sine velocity profile demonstrated that transient N_P is influenced by frequency and amplitude, experiencing a higher variation as the frequency and/or amplitude increase. This result explains the reason why the wind-powered heat

generator has poor thermodynamic performance under gusty wind conditions when the design was based on steady-state N_P. Finally, the effects of different velocity profiles on the working fluid temperature rise revealed that sine velocity motion requires more energy input than constant angular speed, emphasizing again the need to account for resistive forces when designing a heat generator for a specific wind turbine operating under transient conditions.

6.2 Recommendations

Many gaps must be addressed to commercialize the WTEC based on the agitation technology. A few of the recommendations are noted below:

- Due to the physical complexity of the system, the integrated proto-type experimentation of the wind turbine and liquid stirrer under both lab and actual working conditions is an essential direction for future research.
- Examining the system efficiency under various operating modes based on actual wind profiles is an essential step to support the development of this technology.
- Understanding the wind turbine's transient torque behavior is essential for improving the system's efficiency.
- The start-up characteristics of the fluid agitator should also be assessed since it is an integral part of the system operation.
- CFD tools as a numerical simulation method have a great potential to help researchers better understand the underlying physics of the start-up behavior and various operating conditions.

References

[1] Countdown to Net Zero, Energy & Climate Intelligence Unit, 2019.

[2] Net Zero Tracker, Energy & Climate Intelligence Unit, 2020.

[3] Residential sector, Canada, Table 2: Secondary energy use and GHG emissions by end-use, Natural Resources Canada, 2018.

[4] Diesel reduction progress in remote communities, Pembina Institute, 2020.

[5] Energy consumption by end-use, European Commission, 2013.

[6] T. Lychuk, M. Evans, M. Halverson, V. Roshchanka, Analysis of the Russian market for building energy efficiency, Pacific Northwest National Lab (PNNL), Richland, WA (United States) , 2012.

[7] Z. Alnasir, M. Kazerani, An analytical literature review of stand-alone wind energy conversion systems from generator viewpoint, Renewable and Sustainable Energy Reviews. 28 (2013) 597–615. https://doi.org/10.1016/j.rser.2013.08.027.

[8] E. Williams, E. Hittinger, R. Carvalho, R. Williams, Wind power costs expected to decrease due to technological progress, Energy Policy. 106 (2017) 427–435. https://doi.org/10.1016/j.enpol.2017.03.032.

[9] Wind Power Capacity Worldwide Reaches 597 GW, 50,1 GW added in 2018, W. W. E. Association, 2019.

[10] M.Z. Jacobson, C.L. Archer, Saturation wind power potential and its implications for wind energy, Proceedings of the National Academy of Sciences. 109 (2012) 15679–15684.

https://doi.org/10.1073/pnas.1208993109.

[11] L.D. Hansen, P.O. Madsen, Frede Blaabjerg, H.I. Christensen, U. Lindhard, K. Eskildsen, Generators and power electronics technology for wind turbines, Proceedings of the 27th Annual Conference of the IEEE Industrial Electronics Society. (2002). https://doi.org/10.1109/iecon.2001.975598.

[12] H. Polinder, F.F.A. van der Pijl, G.-J.. de Vilder, P.J. Tavner, Comparison of direct-drive and geared generator concepts for wind turbines, IEEE Transactions on Energy Conversion. 21 (2006) 725–733. https://doi.org/10.1109/TEC.2006.875476.

[13] A.N. NITTO, Wind Powered Thermal Energy Systems (WTES) A Techno-economic Assessment of Different Configurations, Master Thesis, 2016.

[14] K.D. Decker, Heat your House with a Mechanical Windmill, LOW←TECH MAGAZINE. (2019). https://solar.lowtechmagazine.com/2019/02/heat-your-house-with-a-mechanical-windmill/#fn:14 (accessed September 1, 2023).

[15] K. De Decker, Real-world tests of small wind turbines in Netherlands and the UK, Resilience. (2010). https://www.resilience.org/stories/2010-09-16/real-world-tests-small-wind-turbines-netherlands-and-uk/#:~:text=The%20average%20electricity%20production%20of (accessed September 1, 2023).

[16] M. Neumeier, M. Cöster, R.A. Marques Pais, S. Levedag, State of the art of windthermal turbines: A systematic scoping review of direct wind-to-heat conversion technologies, Journal of Energy Resources Technology. (2021) 1–46. https://doi.org/10.1115/1.4052616.

[17] R. WAILES, Horizontal Windmills, Transactions of the Newcomen Society. 40 (1967) 125–145. https://doi.org/10.1179/tns.1967.007.

[18] Y. Li, Straight-Bladed Vertical Axis Wind Turbines: History, Performance, and Applications, Rotating Machinery. (2019). https://doi.org/10.5772/intechopen.84761.

[19] P.J. Schubel, R.J. Crossley, Wind Turbine Blade Design, Energies. 5 (2012) 3425–3449. https://doi.org/10.3390/en5093425.

[20] J.F. Manwell, J.G. McGowan, A.L. Rogers, Wind Energy Explained, John Wiley & Sons, Ltd, Chichester, UK, 2009. https://doi.org/10.1002/9781119994367.

[21] E. Hau, H. von Renouard, Wind Turbines, Springer Berlin Heidelberg, Berlin, Heidelberg, 2006. https://doi.org/10.1007/3-540-29284-5.

[22] J. Ribrant, L.M. Bertling, Survey of Failures in Wind Power Systems with Focus on Swedish Wind Power Plants During 1997–2005, IEEE Transactions on Energy Conversion. 22 (2007) 167–173. https://doi.org/10.1109/tec.2006.889614.

[23] H. Li, Z. Chen, Overview of different wind generator systems and their comparisons, IET Renewable Power Generation. 2 (2008) 123–138. https://doi.org/10.1049/iet-rpg:20070044.

[24] S. Apelfröjd, S. Eriksson, H. Bernhoff, A Review of Research on Large Scale Modern Vertical Axis Wind Turbines at Uppsala University, Energies. 9 (2016) 570. https://doi.org/10.3390/en9070570.

[25] IEA - Data and statistics, International Energy Agency, n.d.

[26] P. Cooper, Development and analysis of vertical-axis wind turbines, WIT Transactions on State-of-The-Art in Science and Engineering. (2010) 277–302. https://doi.org/10.2495/978-1-84564-205-1/08.

[27] J.F. Manwell, J.G. McGowan, A design procedure for wind powered heating systems, Solar

Energy. 26 (1981) 437–445. https://doi.org/10.1016/0038-092x(81)90223-1.

[28] J.T. Hamrick, L.C. Rose, Heat pump operated by wind or other power means, 1980.

[29] B. Ashikian, Wind motor operated heating system, 1971.

[30] S. Neyeloff, Analysis of a wind heat converter to heat water in closed tanks, Ph.D Thesis, 1979.

[31] U. Hansen, Wind powered heating circuit - has sails on wind tower driving eddy current brake for producing heat for heat exchange fluid, 1980.

[32] W.W. Gunkel, D.R. Lacey, S. Neyeloff, T.C. Porter, Wind energy for direct water heating. Final report, OSTI OAI (U.S. Department of Energy Office of Scientific and Technical Information). (1981). https://doi.org/10.2172/5348530.

[33] V.R. Nattuvetty, W.W. Gunkel, Theoretical performance of a straight-bladed cycloturbine under four different operating conditions, Wind Engineering. 6 (1982) 110–130.

[34] B. Kirke, Evaluation of Self-Starting Vertical Axis Wind Turbines for Stand-Alone Applications, (1998). https://doi.org/10.25904/1912/1503.

[35] Y.J. Kim, Y.-S. Ryou, Yong Han Yoon, K.-H. Kang, Windheat Heating System Development for Greenhouse Plant Bed Heating, (2001). https://doi.org/10.13031/2013.4745.

[36] Y. Nakatake, H. Tanaka, A new maritime lifesaving distiller driven by wind, Desalination. 177 (2005) 31–42. https://doi.org/10.1016/j.desal.2004.10.031.

[37] Y.J. Kim, J.H. Yun, Y.S. Ryou, G.C. Kang, Y. Paek, Factors Affecting Performance of a Proto type Windheat Generation System, (2005).

[38] Y.-J. Kim, G.-C. Kang, J.-H. Yun, Y.-S. Ryou, Y. Paek, K. Youn-Ku, An Experimental Study on a Windheat Generation System with a Savonius Wind Turbine, Agricultural and Biosystems Engineering. (2005).

[39] M. Katawaluwa, H. Zhang, Yuriy Vagapov, J. Evans, Simulation of Wind Heat Generator, Glyndwr University Research Online (Glyndwr University). (2006). https://doi.org/10.1109/eit.2006.252138.

[40] I. Sateikis, S. Lynikiene, B. Kavolelis, Analysis of feasibility on heating single family houses in rural areas by using sun and wind energy, Energy and Buildings. 38 (2006) 695–700. https://doi.org/10.1016/j.enbuild.2005.11.003.

[41] R. Chakirov, Y. Vagapov, Direct conversion of wind energy into heat using Joule machine, 4th Int. Conference on Environmental and Computer Science (ICECS). (2011).

[42] M.A. Al-Nimr, W.A.M. Al-Shohani, Design of a Wind Water Heater, Applied Mechanics and Materials. 110-116 (2011) 4970–4976. https://doi.org/10.4028/www.scientific.net/amm.110-116.4970.

[43] J. Zhao, Qing Miao Liu, Feng Chen Wang, Y. Mei, Shao Jiong Huang, Experimental Study on Stirring Wind-Heating Devices, Advanced Materials Research. (2014). https://doi.org/10.4028/www.scientific.net/amr.953-954.419.

[44] J. Černeckienė, Usage of the Wind Energy for Heating of the Energy-Efficient Buildings: Analysis of Possibilities, Journal of Sustainable Architecture and Civil Engineering. 10 (2015). https://doi.org/10.5755/j01.sace.10.1.7479.

[45] T. Okazaki, Y. Shirai, T. Nakamura, Concept study of wind power utilizing direct thermal energy conversion and thermal energy storage, Renewable Energy. 83 (2015) 332–338.

https://doi.org/10.1016/j.renene.2015.04.027.

[46] Y. Hu, S. Xue, Y. Liu, Z. Han, Structure Design and Experimental Study on stirred-damped Wind-powered Heater, Journal of Shanghai University of Electric Power. (2017).

[47] Y. Hu, K. Li, H. Jin, Structure Design and Parameter Computation of a Seawater Desalination System with Vertical Axis Wind Turbine, Communications in Computer and Information Science. (2017). https://doi.org/10.1007/978-981-10-6364-0_5.

[48] S. Su, Analysis of Wind Heating System to Solve Winter Heating in Northeast China, (2017). https://doi.org/10.2991/msmee-17.2017.86.

[49] M. Zheng, Y. Tian, H. Teng, J. Hu, F. Wang, Y. Zhao, L. Yu, Prospect of wind energy application in China's oilfields for heating, International Review of Applied Sciences and Engineering. 8 (2017) 141–144. https://doi.org/10.1556/1848.2017.8.2.6.

[50] S. Mei, Z. Yaxu, H. Xuguang, Status and Development Suggestions of Wind Heating in Northern China, Energy Procedia. 142 (2017) 105–110. https://doi.org/10.1016/j.egypro.2017.12.017.

[51] W.-L. Cheng, B.-C. Han, Y.-L. Nian, B.-B. Han, Theoretical analysis of a wind heating conversion and long-distance transmission system, Energy Conversion and Management. 137 (2017) 21–33. https://doi.org/10.1016/j.enconman.2017.01.021.

[52] K. Yang, X. Sun, Y. Guo, S.-S. Bi, X. Qiu, Experimental Study on the Performance of Wind Stirring System with Different Working Fluids, (2018). https://doi.org/10.2991/edep-18.2018.17.

[53] K.-K. Cao, A.N. Nitto, E. Sperber, A. Thess, Expanding the horizons of power-to-heat: Cost assessment for new space heating concepts with Wind Powered Thermal Energy Systems, Energy.

164 (2018) 925–936. https://doi.org/10.1016/j.energy.2018.08.173.

[54] J. Ma, Direct wind heating greenhouse underground heating system, IOP Conference Series: Earth and Environmental Science. 300 (2019) 042056. https://doi.org/10.1088/1755-1315/300/4/042056.

[55] Y.-C. Chen, J. Radcliffe, Y. Ding, Concept of offshore direct wind-to-heat system integrated with thermal energy storage for decarbonizing heating, (2019). https://doi.org/10.1109/oses.2019.8867047.

[56] L. Zhang, Q. Yao, K. Li, Research and application of a domestic system of wind power directly stirring heating---Taking northeast China as an example, IOP Conference Series. 440 (2020) 032002–032002. https://doi.org/10.1088/1755-1315/440/3/032002.

[57] X. Liu, X. Sun, J. Li, X. Qiu, Y. Kang, Y. Cao, Experimental Study on the Heating Effect of a Wind-Energy Stirring Heater, Journal of Thermal Science. 30 (2021) 772–781. https://doi.org/10.1007/s11630-021-1344-4.

[58] L. Chen, X. Ma, H. Xie, Y. Li, J. Liu, D. Liu, Start-up performance and optimization of the stirring wind-heating system, IOP Conference Series: Earth and Environmental Science. 657 (2021) 012085. https://doi.org/10.1088/1755-1315/657/1/012085.

[59] D. McLean, K. Pope, X. Duan, Start-up considerations for a small vertical-axis wind turbine for direct wind-to-heat applications, Energy Conversion and Management. 261 (2022) 115595. https://doi.org/10.1016/j.enconman.2022.115595.

[60] X. Liu, X. Sun, J. He, D. Wang, X. Qiu, S. Bi, Y. Cao, Study on the Influence of Working-Fluid's Thermophysical Properties on the Stirring-Heating, Energies. 15 (2022) 4835. https://doi.org/10.3390/en15134835.

[61] L. Swinfen-Styles, S.D. Garvey, D. Giddings, Combining Wind-Driven Air Compression with Underwater Compressed Air Energy Storage, IEEE Xplore. (2019) 1–8. https://doi.org/10.1109/OSES.2019.8867344.

[62] S.D. Garvey, A.J. Pimm, J.A. Buck, S. Woolhead, K.W. Liew, B. Kantharaj, J.E. Garvey, B.D. Brewster, Analysis of a Wind Turbine Power Transmission System with Intrinsic Energy Storage Capability, Wind Engineering. 39 (2015) 149–173. https://doi.org/10.1260/0309-524x.39.2.149.

[63] C.-S. Jwo, Z.-J. Chien, Y.-L. Chen, C.-C. Chien, Development of a Wind Directly Forced Heat Pump and Its Efficiency Analysis, International Journal of Photoenergy. 2013 (2013) 1–7. https://doi.org/10.1155/2013/862547.

[64] J.I. Tapiador, A.Y. Chua, A Novel Automated Wind Chiller Hybrid Cooling System for a Cold Storage Room Application, International Journal of Mechanical Engineering and Robotics Research. (2018) 662–668. https://doi.org/10.18178/ijmerr.7.6.662-668.

[65] H.H. Klueter, L.A. Liljedahl, Feasibility of Wind-Powered Mechanically-Driven Heat Pump for a Dairy, Transactions of the ASAE. 25 (1982) 0745–0751. https://doi.org/10.13031/2013.33606.

[66] W.W. Gunkel, G.B. Kromann, V.R. Nattuvetty, Performance Analysis of a Wind-Assisted Heat Pump for a Dairy, Transactions of the ASAE. 28 (1985) 255–262. https://doi.org/10.13031/2013.32237.

[67] T. Zdankus, J. Cerneckiene, A. Jurelionis, J. Vaiciunas, Experimental Study of a Small-Scale Hydraulic System for Mechanical Wind Energy Conversion into Heat, Sustainability. 8 (2016) 637. https://doi.org/10.3390/su8070637.

[68] T. Ždankus, J. Černeckienė, L. Greičius, V. Stanevičius, N. Bunikis, Wind Energy Usage for Building Heating Applying Hydraulic System, Journal of Sustainable Architecture and Civil Engineering. 25 (2019) 63–70. https://doi.org/10.5755/j01.sace.25.2.21542.

[69] T. Zdankus, J. Cerneckiene, R. Jonynas, G. Stelmokaitis, P.A. Fokaides, Experimental investigation of a wind to thermal energy hydraulic system, Renewable Energy. 159 (2020) 140–150. https://doi.org/10.1016/j.renene.2020.05.175.

[70] P.C. Verma, R. Ciudin, A. Bonfanti, P. Aswath, G. Straffelini, S. Gialanella, Role of the friction layer in the high-temperature pin-on-disc study of a brake material, Wear. 346-347 (2016) 56–65. https://doi.org/10.1016/j.wear.2015.11.004.

[71] O. Grigorash, A. Kirichenko, K. Pigarev, Model of Induction Heater on Permanent Magnets Using Wind Energy, 2019 International Conference on Industrial Engineering, Applications and Manufacturing (ICIEAM). (2019). https://doi.org/10.1109/icieam.2019.8743026.

[72] X.H. Liu, C.C. Chen, H.D. Yu, G.D. Wei, Z.D. Tian, The Study of the Heat Device in Wind-Magnetic Water Heater, Advanced Materials Research. 201-203 (2011) 460–464. https://doi.org/10.4028/www.scientific.net/amr.201-203.460.

[73] T. Tudorache, M. Popescu, FEM Optimal Design of Wind Energy-based Heater, (2009).

[74] O. Nebi, Virgiliu Fireteanu, Finite element analysis of an eddy currents heater for wind or water kinetic energy conversion into heat, Renewable Energy & Power Quality Journal. (2010). https://doi.org/10.24084/repqj08.506.

[75] I. Dirba, J. Kleperis, Practical Application of Eddy Currents Generated by Wind, IOP Conference Series: Materials Science and Engineering. 23 (2011) 012011. https://doi.org/10.1088/1757-899x/23/1/012011.

[76] L. Chen, Y. Pei, F. Chai, S. Cheng, Investigation of a Novel Mechanical to Thermal Energy Converter Based on the Inverse Problem of Electric Machines, Energies. 9 (2016) 518–518. https://doi.org/10.3390/en9070518.

[77] M. Jaszczur, A. Młynarczykowska, L. Demurtas, Effect of Impeller Design on Power Characteristics and Newtonian Fluids Mixing Efficiency in a Mechanically Agitated Vessel at Low Reynolds Numbers, Energies. 13 (2020) 640. https://doi.org/10.3390/en13030640.

[78] M. Ragheb, Optimal Rotor Tip Speed Ratio, Work Notes. (2009).

[79] V.W. Uhl, Joseph Burham Gray, Mixing: theory and practice. Volume II, Academic Press, New York (N.Y.) ; London, 1967.

[80] J. Henry Rushton, Power Characteristics of Mixing Impellers part 1, 46 (1950) 395–404.

[81] M.J. Moran, H.N. Shapiro, D.D. Boettner, M.B. Bailey, Fundamentals of engineering thermodynamics., John Wiley & Sons, Inc, Hoboken, Nj, 2018.

[82] S. Kamei, S. Nagata, N. Yoshioka, Studies on the Power Requirement of Paddle Agitators in Cylindrical Vessels, Kagaku Kōgaku. 20 (1956) 582–592. https://doi.org/10.1252/kakoronbunshu1953.20.582.

[83] V.W. Uhl, J.B. Gray, Mixing Theory and Practice Volume 1, 1966.

[84] Konstantinos Steiros, Effect of Impeller Design and Rotation Protocol on the Power Consumption of Turbulent Stirred Tanks, Ph.D Thesis, 2017.

[85] T. Kumaresan, J.B. Joshi, Effect of impeller design on the flow pattern and mixing in stirred tanks, Chemical Engineering Journal. 115 (2006) 173–193. https://doi.org/10.1016/j.cej.2005.10.002.

[86] ÇengelY.A., J.M. Cimbala, Fluid mechanics: fundamentals and applications, Mcgraw-Hill Education, Singapore, 2020.

[87] R.L. Bates, P.L. Fondy, R.R. Corpstein, Examination of Some Geometric Parameters of Impeller Power, Industrial & Engineering Chemistry Process Design and Development. 2 (1963) 310–314. https://doi.org/10.1021/i260008a011.

[88] A.W. Nienow, D. Miles, Impeller Power Numbers in Closed Vessels, Industrial & Engineering Chemistry Process Design and Development. 10 (1971) 41–43. https://doi.org/10.1021/i260037a007.

[89] R.L. King, R.A. Hiller, G.B. Tatterson, Power consumption in a mixer, AIChE Journal. 34 (1988) 506–509. https://doi.org/10.1002/aic.690340320.

[90] S. Nagata, Mixing: Principles and Applications, A Halsled Press book, 1975.

[91] W. Bujalski, A.W. Nienow, S. Chatwin, M. Cooke, The dependency on scale of power numbers of Rushton disc turbines, Chemical Engineering Science. 42 (1987) 317–326. https://doi.org/10.1016/0009-2509(87)85061-3.

[92] C. Xanthopoulos, M. Stamatoudis, Turbulent range impeller power numbers in closed cylindrical and square vessels, Chemical Engineering Communications. 46 (1986) 123–128. https://doi.org/10.1080/00986448608911401.

[93] D. Chapple, S.M. Kresta, A. Wall, A. Afacan, The Effect of Impeller and Tank Geometry on Power Number for a Pitched Blade Turbine, Chemical Engineering Research and Design. 80 (2002) 364–372. https://doi.org/10.1205/026387602317446407.

[94] K. Rutherford, S.M.S. Mahmoudi, K.C. Lee, M. Yianneskis, The Influence of Rushton

Impeller Blade and Disk Thickness on the Mixing Characteristics of Stirred Vessels, Chemical Engineering Research & Design. 74 (1996) 369–378.

[95] Setsuya Aiba, Flow patterns of liquids in agitated vessels, Aiche Journal. 4 (1958) 485–489. https://doi.org/10.1002/aic.690040419.

[96] S. Nagata, K. Yamamoto, M. Ujihara, Flow Patterns of Liquid in a Cylindrical Mixing Vessel without Baffles, Chemical Engineering. 23 (1959) 130–137. https://doi.org/10.1252/kakoronbunshu1953.23.130.

[97] S. Woziwodzki, Unsteady Mixing Characteristics in a Vessel with Forward-Reverse Rotating Impeller, Chemical Engineering & Technology. 34 (2011) 767–774. https://doi.org/10.1002/ceat.201000455.

[98] D. Gao, S. Acharya, Y. Wang, J. Uhm, Flow field around Rushton turbine in stirred tank by particle image velocimetry measurement, Chinese Journal of Chemical Engineering. 12 (2004).

[99] S. Roy, S. Acharya, Effect of Impeller Speed Perturbation in a Rushton Impeller Stirred Tank, Journal of Fluids Engineering. 134 (2012). https://doi.org/10.1115/1.4006471.

[100] D. Maynes, M. Butcher, Steady-state and decay dynamics for impellers of varying aspect ratio in unbaffled tanks, Aiche Journal. 48 (2002) 38–49. https://doi.org/10.1002/aic.690480106.

[101] M. Yoshida, A. Ito, Kazuaki Yamagiwa, Akira Ohkawa, M. Abe, Shuichi Tezura, Masuo Shimazaki, Power characteristics of unsteadily forward-reverse rotating impellers in an unbaffled aerated agitated vessel, Journal of Chemical Technology & Biotechnology. 76 (2001) 383–392. https://doi.org/10.1002/jctb.394.

[102] L. Li, Xiang Ke-feng, B. Xiang, Numerical simulation of transient power consumption

characteristics in an unbaffled stirred tank, Chemical Papers. 74 (2020) 2849–2859. https://doi.org/10.1007/s11696-020-01115-3.

[103] L. Li, B. Xu, CFD simulation of hydrodynamics characteristics in a tank with forward-reverse rotating impeller, Journal of the Taiwan Institute of Chemical Engineers. 131 (2022) 104174. https://doi.org/10.1016/j.jtice.2021.104174.

[104] M.H. Javed, Experimental study on kinetic to thermal energy conversion with fluid agitation, Master Thesis, 2021.

[105] J.L. Semmlow, Circuits, signals and systems for bioengineers: a MATLAB-based introduction, Elsevier/Academic Press, London, United Kingdom, 2018.

[106] R.J. Moffat, Describing the uncertainties in experimental results, Experimental Thermal and Fluid Science. 1 (1988) 3–17. https://doi.org/10.1016/0894-1777(88)90043-x.

[107] The MathWorks, Inc. (2022). MATLAB version: 9.13.0 (R2022b).

[108] https://www.orcina.com/webhelp/OrcaFlex/Content/html/Environment,Winddata.htm

Appendix A: Equipment datasheet and drawings

A.1 Stepper motor

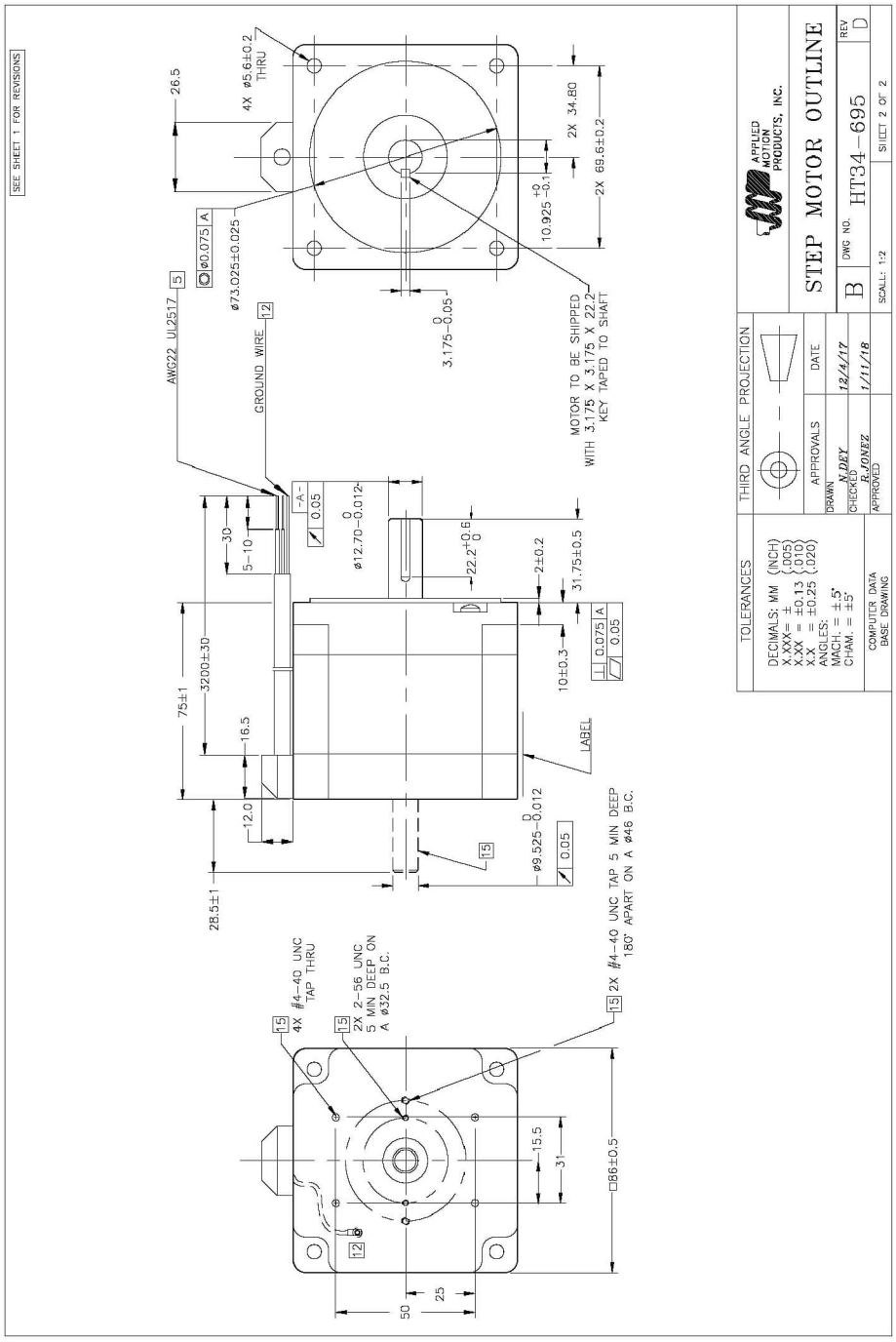

A.2 Torque sensor

FUTEK
ADVANCED SENSOR TECHNOLOGY, INC.

MODEL TRS605

Non-Contact Shaft-to-Shaft Rotary Torque Sensor with Encoder

FEATURES

- Utilizes strain gauge technology
- Angle speed feedback
- Compact size
- Can operate up to 7000 RPM

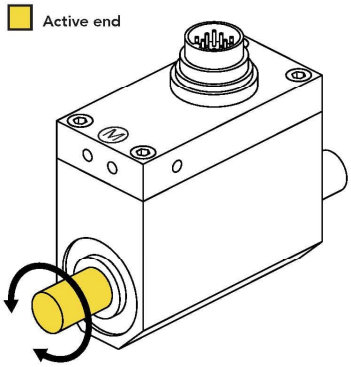

– Output (CCW)
+ Output (CW)

Ⓜ = Measuring Side

SPECIFICATIONS	
PERFORMANCE	
Nonlinearity	±0.2% of RO
Hysteresis	±0.1% of RO
Nonrepeatability	±0.2% of RO
Rotational Speed	7000 Max
ELECTRICAL	
Bandwidth	3 kHz
Typical Noise	<50 mV p-p
Rated Output (RO)	±5 VDC
Excitation	11–26 VDC, 1 Watt
Connector	12 pin Binder Series #581 (09-0331-90-12)
MECHANICAL	
Safe Overload	150% of RO
Zero Balance	±1% of RO
Material	Aluminum (Housing), Steel Alloy (Shaft)
IP Rating	IP40
TEMPERATURE	
Operating Temperature	–13 to 176°F (–25 to 80°C)
Compensated Temperature	41 to 122°F (5 to 50°C)
Temperature Shift Zero	±0.01% of RO/°F (±0.02% of RO/°C)
Temperature Shift Span	±0.01% of RO/°F (±0.02% of RO/°C)
CALIBRATION	
Calibration Test Excitation	12 VDC
Calibration (standard)	Certificate of Conformance
Calibration (available)	5-pt CW & CCW
Shunt Calibration Value	With sensor fully connected apply 11–26 VDC to Pins A & K to generate 5 VDC nom output
ENCODER	
Output	Impulse (TTL)
Pulses per Revolution	2 × 360
Excitation	5 VDC, 40 mA max
Angle 1	Leading Pulse
Angle 2	Trailing Pulse (90°)
CONFORMITY	
RoHS	2014/30/EU
CE	Declaration of Conformity

Sensor Solution Source
Load · Torque · Pressure · Multi-Axis · Calibration · Instruments · Software

www.futek.com

CE RoHS ANSI Z540-1 ISO 17025 ISO 9001 ISO 13485 U.S. Manufacturer

A.3 Heat generator

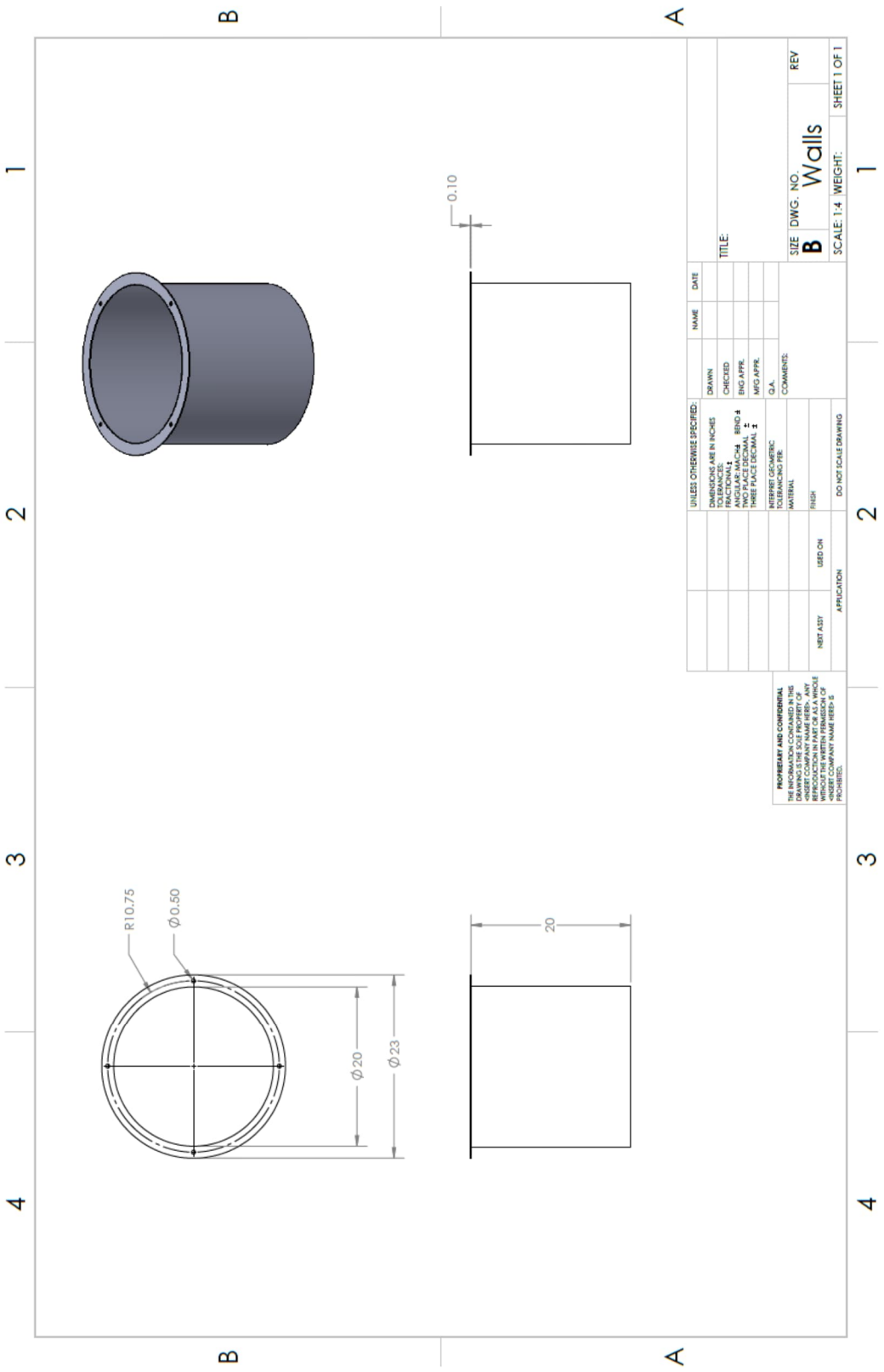

REVISION HISTORY

REV	DESCRIPTION	INCORP BY	DATE	CHECKED

NOTES:

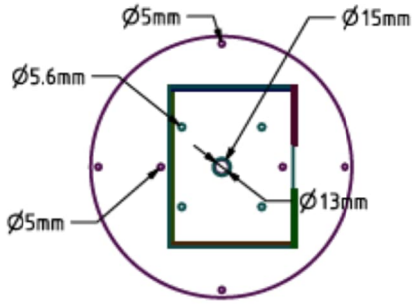

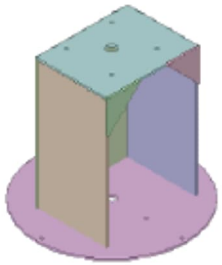

SCALE 1:5

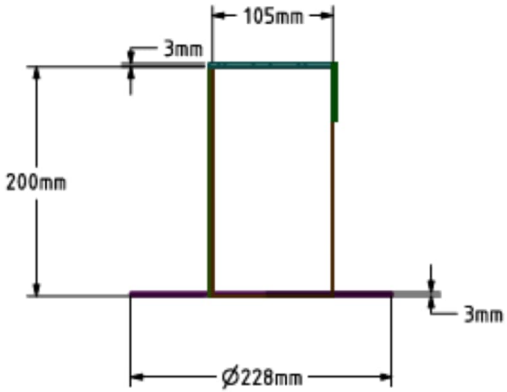

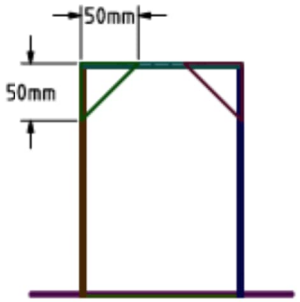

-2 QTY REQD	-1	ITEM NO.	PART OR IDENTIFYING NO.	NOMENCLATURE OR DESCRIPTION

PARTS LIST

INIT	APPROVALS	DATE	INIT	APPROVALS	DATE

	CONTRACT NO.	MATERIAL
		FINISH
THIRD ANGLE PROJECTION		TREATMENT
	NEXT ASSY / USED ON	SIMILAR TO
	APPLICATION	

TITLE

SIZE	CAGE CODE	DWG NO.	REV
B			
SCALE		SHEET	

A.4 Impeller

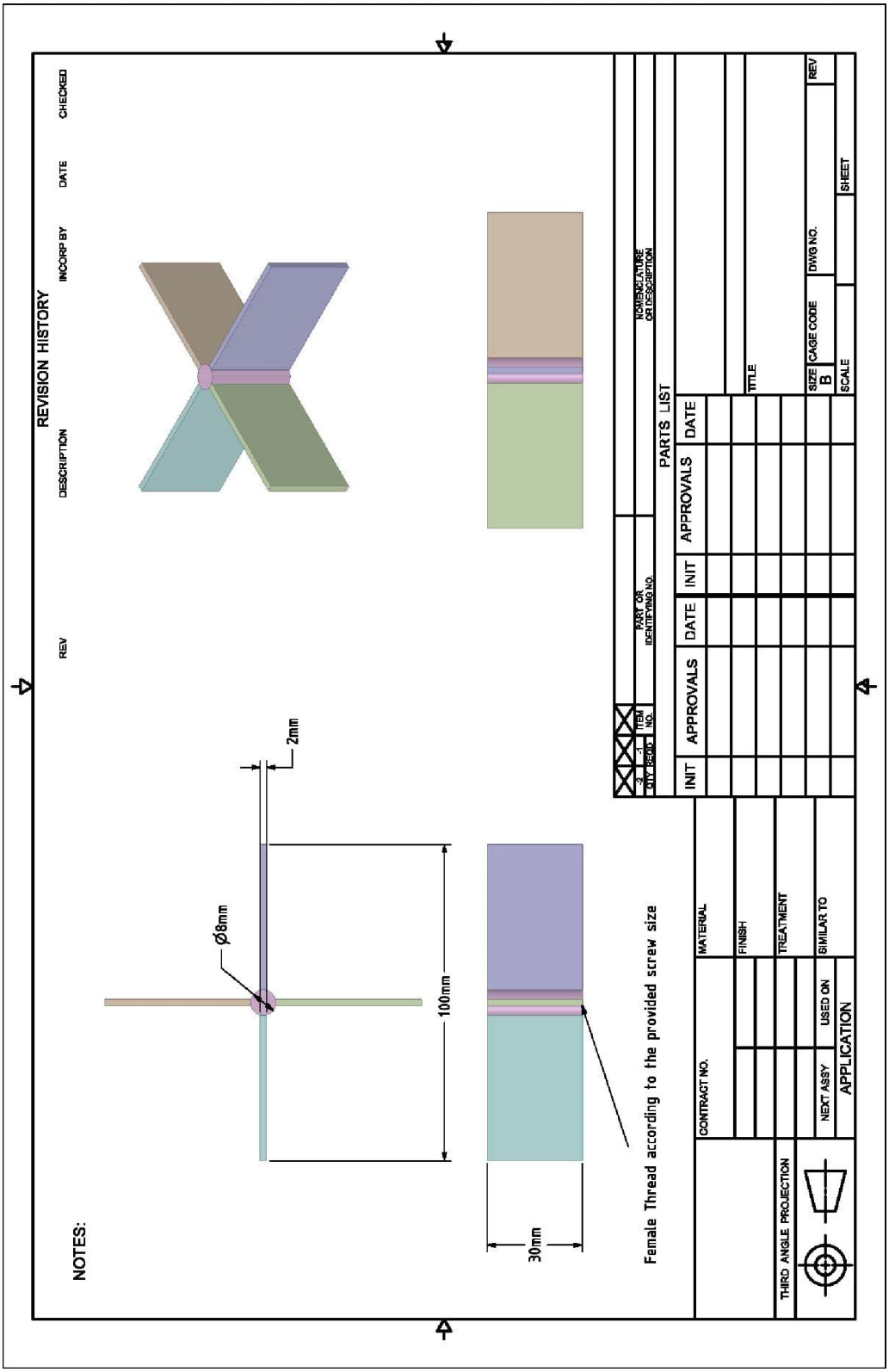
REVISION HISTORY
REV
DESCRIPTION
INCORP BY
DATE
CHECKED
NOTES:
Female Thread according to the provided screw size
Ø8mm
2mm
100mm
30mm
PARTS LIST
ITEM NO.
PART OR IDENTIFYING NO.
NOMENCLATURE OR DESCRIPTION
QTY REQD
APPROVALS
INIT
DATE
TITLE
SIZE
B
CAGE CODE
DWG NO.
REV
SCALE
SHEET
CONTRACT NO.
MATERIAL
FINISH
TREATMENT
NEXT ASSY
USED ON
SIMILAR TO
APPLICATION
THIRD ANGLE PROJECTION

Appendix B: Codes

B.1 Sample Arduino code

The following sample code was used to control the stepper motor rotational velocity by defining three different stages: 1) The motor starts accelerating from the quiescent with a predefined acceleration rate to ω_2, 2) rotating at ω_2 for a specified period, 3) then decelerating to zero speed with a specific deceleration rate.

```
#include <Stepper.h>

// Define the stepper motor connections and other variables
#define STEPS_PER_REV 800
#define DIR_PIN 8
#define STEP_PIN 9
#define EN_PIN 50
// #define MICROSTEPS 16
Stepper stepper(STEPS_PER_REV, DIR_PIN, STEP_PIN);

/*Parameters*/
//////////////
int speed_min = 1; // Min motor speed in RPM
int speed_max = 200; // Max motor speed in RPM
int speed_incr = 10; // Acceleration in RPM/s
int ss_time = 5; // Steady state time in seconds
bool CW = false; // Direction of rotation (true for CW , flase for CCW)

/*variables*/
float speed = 0; // Motor speed
int dir = 0;


void setup() {
  // Initialize
  Serial.begin(9600);

  pinMode(EN_PIN, OUTPUT);
  digitalWrite(EN_PIN, HIGH);

  pinMode(DIR_PIN, OUTPUT);
  digitalWrite(DIR_PIN, LOW);

  stepper.setSpeed(speed_min);

  // Set the initial position of the stepper motor
  //stepper.setCurrentPosition(0);

  if (CW==true){
    dir = 1;
  }else{
    dir = -1;
  }
}

void loop() {

// Accelaration
  /* For loop- Loop starts at an RPM of speed_min and accelerates at a rate of
  speed_incr RPM/s until speed is equal to speed_max*/
  for (speed = speed_min;speed < speed_max;speed=speed + speed_incr/10){
    // Set new speed after increasing speed
    stepper.setSpeed(speed);
    // Move the corresponding no. of steps to maintain steady accelaration
    stepper.step(dir * 80 * speed/60);
  }

// Steady state
for (int i=0 ; i < ss_time ;i++){
  stepper.step(dir * 800 * speed/60);
}

// Decelaration
  /* For loop- Loop starts at an RPM of speed_min and accelerates at a rate of
  speed_incr RPM/s until speed is equal to speed_max*/
  for (speed = speed_max;speed > speed_min;speed=speed - speed_incr/10){
    // Set new speed after increasing speed
    stepper.setSpeed(speed);
    // Move the corresponding no. of steps to maintain steady accelaration
    stepper.step(dir * 80 * speed/60);
  }
}
```

B.2 MATLAB code

The following MATLAB code presents signal processing calculations applied to the raw torque data to find ensemble-averaged torque.

```
clear all, clc;
directory_t = 'C:\Users\navidn\Documents\MATLAB\Measurements\Transient\FT-07\09\29-09-23\Deceleration\n2=3, alpha=2\n1=8\Results' %with the actual directory path
filename = 't.xlsx';            % Replace with your file name

% Combine the directory and filename
fullPath = fullfile(directory_t, filename);

% Load the Excel file as a table
t = readtable(fullPath);

% Specify the directory containing the Excel files
directory = 'C:\Users\navidn\Documents\MATLAB\Measurements\Transient\FT-07\09\29-09-23\Deceleration\n2=3, alpha=2\n1=8';

% directory = 'C:\Users\navidn\Documents\MATLAB\Measurements\Transient\FT-10\19-05-23\Acceleration\1-alpha=0.25, n=5\3-Empty Tank';

% Get a list of all Excel files in the directory
fileList = dir(fullfile(directory, '*.xlsx')); % Modify '*.xlsx' based on your file extension

% Initialize a cell array to store the values for each file
Y = cell(numel(fileList), 1);

% Specify the column names to copy
columnNames = {'TrackingValue', 'RPM'}; % Replace with your desired column names

% Loop through each Excel file

for i = 1:numel(fileList)
    % Get the file name
    filename = fileList(i).name;

    % Read the Excel file as a table
    tableData = readtable(fullfile(directory, filename));

    % Extract the desired columns from the table
    selectedColumns = tableData(:, columnNames);

    % Get the column data from the table
    columnName = 'RPM'; % Replace 'RPM' with the name of the desired column
    RPM = selectedColumns.(columnName);

    R{i} = RPM(:,1);

    columnName = 'TrackingValue'; % Replace 'TrackingValue' with the name of the desired column
    T = selectedColumns.(columnName);

    % Perform your desired operations with the values (e.g., find the row index)
    B = [RPM, T];
    columnIndex = 1;

% rowIndex = find(all(B(:, columnIndex:end) ~= 0, 2), 1);
rowIndex = find(B(:, columnIndex) < 477, 1);
% Get the value from another column, 40 rows before the found row
anotherColumnIndex = 2; % Replace 5 with the index of the desired column
targetRowIndex = rowIndex -1400; % Calculate the row index 30 rows before
C = B(targetRowIndex:end,:);
x = 3291;
 D = C(1:x, :);

    % Store the values in a cell array or structure for the current file
     Y{i} = D(:,2);
     R{i} = D(:,1);
end
```

```
% Create new variables
for i = 1:numel(Y)
    eval(['T', num2str(i), ' = Y{i};']);
end

% Create a new variable and concatenate T1 to Ti
T_t= [];
for j = 1:i
    variableName = ['T', num2str(j)];  % Create the variable name dynamically
    T_t = [T_t, eval(variableName)];  % Concatenate the variables
end

% Create new variables
for i = 1:numel(R)
    eval(['RPM', num2str(i), ' = R{i};']);
end


RPM_avg= [];
for j = 1:i
    variableName = ['RPM', num2str(j)];  % Create the variable name dynamically
    RPM_avg = [RPM_avg, eval(variableName)];  % Concatenate the variables
end

[nu,N] = size(RPM_avg);

if nu > N

    RPM_avg = RPM_avg';
end

R_avg = mean(RPM_avg);


%ensemble_Averaging

sample_rate = 25;

fs = 1/ (1/sample_rate);

% Specify the range of row numbers

startRow = 1;    % Starting row number
endRow = x;      % Ending row number


% Access the data from the table array
dt = t.dt(startRow:endRow, :);

[nu,N] = size (dt);

if nu > N
    dt = dt';
end

[nu,N] = size(T_t);

if nu > N

    T_t = T_t';
end

% plot one of the records
subplot (1,2,1)
plot (dt, T_t(2,:));

%calculate ensemble average

avg = mean(T_t);

% plot the average
subplot (1,2,2)
plot (dt, avg);
```

```
139
140 % Specify the directory and file name
141 %directory3 = directory;  % Replace with your desired directory path
142 %filename = 'avgll.mat';          % Replace with your desired file name
143
144 % Combine the directory and file path
145 %fullPath = fullfile(directory, filename);
146
147 % Save the variable to the specified directory and file
148 %save(fullPath, 'avg');
149
150 save('workspace.mat')
```